RSC Advances

REVIEW

View Article Online
View Journal | View Issue

Cite this: *RSC Adv.*, 2026, **16**, 11793

Multifunctional lanthanide-based iron oxide luminescent–magnetic nanoparticles: synthesis, properties and biomedical applications

Md. Shamiull Alim Munna,[a] Tanvir Hossain,[a] Md. Shahidul Islam,[a] O. Thompson Mefford,[b] Hasan Ahmad[a] and Md. Mahbubor Rahman *[a]

Multifunctional nanocomposites that integrate lanthanide photophysics with iron oxide magnetism represent a rapidly expanding class of materials for precision bioimaging and theranostics. Lanthanide-based iron oxide nanoparticles (Ln-IONPs) uniquely combine the narrow f–f emissions, long-lived excited states, and UC/DC luminescence of lanthanides with the superparamagnetism, high relaxivity, and magnetic field responsiveness of Fe_3O_4/γ-Fe_2O_3. However, their rational design remains challenging due to interfacial energy transfer, concentration-dependent cross-relaxation, and fluorescence quenching induced by iron oxide. This review provides the first systematic overview of Ln-IONPs, covering their fundamental luminescent and magnetic mechanisms, ligand and host engineering, and factors influencing their optical and magnetic performance, such as particle size, dopant distribution, surface chemistry, pH, temperature, and solvent effects. Synthetic strategies, including coprecipitation, thermal decomposition, hydro(solvo)thermal growth, sol–gel assembly, microwave-mediated crystallization, and polymer-integrated architectures, are critically evaluated with respect to phase control, heterointerface engineering, and quenching suppression *via* inert buffer layers. We further highlight recent advances in multimodal bio-applications, including high-resolution UC imaging, magnetically guided drug delivery, photothermal/photodynamic therapy, and integrated opto-magnetothermal theranostics. Persistent challenges, such as optimizing core–shell energy barriers, balancing luminescence efficiency with magnetic moment retention, and improving *in vivo* stability and clearance, are discussed alongside future opportunities for designing next-generation Ln-IONPs with enhanced optical–magnetic coupling and clinical translational potential.

Received 10th December 2025
Accepted 10th February 2026

DOI: 10.1039/d5ra09579d

rsc.li/rsc-advances

[a]*Polymer Colloids & Nanomaterials (PCN) Research Laboratory, Department of Chemistry, University of Rajshahi, Rajshahi-6205, Bangladesh. E-mail: mrchem@ru.ac.bd*

[b]*Department of Materials Science and Engineering, Clemson University, South Carolina, USA*

Md. Shamiull Alim Munna

Md. Shamiull Alim Munna completed his BSc (Honours) in Chemistry and MSc (by thesis) in Organic Chemistry in the Department of Chemistry, University of Rajshahi, Bangladesh. He is a researcher at the Polymer, Colloids & Nanomaterials (PCN) Laboratory, RU, with experience in the synthesis and characterization of functional nanomaterials. His research interests include lanthanide-based nanomaterials, iron oxide nanoparticles, and opto-magnetic nanohybrids for biomedical imaging and theranostic applications.

Tanvir Hossain

Tanvir Hossain completed his Bachelor of Science (BSc) in Chemistry and Master of Science (MSc, by thesis) in Organic Chemistry in the Department of Chemistry, University of Rajshahi, Bangladesh. His work focuses on luminescent and magnetic nanostructures for biomedical imaging and therapeutic applications. He is actively involved in reviewing recent advances in multifunctional magnetic nanomaterials.

1. Introduction

Lanthanides are the 15 elements of period six and group IIIB in the periodic table, ranging from lanthanum to lutetium, with the electronic configuration [Xe] $4f^{n-1}$ $5d^{0-1}$ $6s^2$ ($n = 15$). Lanthanides are distinguished by their 4f electrons, which give them special properties. Except for La^{3+} and Lu^{3+}, the number of unpaired electrons in 4f orbitals with large unquenched angular momentum can be as high as seven, resulting in effective spin–orbit coupling (SOC) and considerable paramagnetic characteristics. The magnetic moments, magnetic susceptibilities, and electronic relaxation times of lanthanide (Ln) ions are all dictated by their 4f electron configurations, which vary considerably along the series.[1–3] Furthermore, Ln ions can display strong fluorescence emissions *via* intra-4f or 4f–5d transitions due to their numerous f-orbital configurations, which produce characteristic line-like emission bands (Fig. 1), and are isolated from the external environment by outer s and p-orbitals.[4] Thus, Ln ions work as emitting species in phosphors. With the tremendous advances in nanoscience and nanotechnology during the last few decades, uniform Ln^{3+}-based nanoparticles have been outlined for potential bio applications. For example, the well-controlled size, crystallinity, and distinctive magnetic properties of Ln^{3+} nanoparticles make them a viable option for magnetic resonance imaging (MRI) contrast agents.[5] In particular, up-conversion nanoparticles (UCNPs) doped with Ln^{3+} ions have attracted significant interest in biological applications because they can sequentially absorb multiple lower-energy (longer-wavelength) photons and emit higher-energy anti-Stokes luminescence.[6] In comparison to traditional biomarkers, such as organic dyes, quantum dots (QDs), or fluorescent proteins, Ln^{3+}-doped UCNPs are unique in terms of photobleaching resistance, as well as reduced photo blinking, emission cross-talk, and autofluorescence from organisms.[7] Furthermore, these UCNPs use near infra-red (NIR) excitation, which can penetrate deeper into biological tissues, so they will have greater advantages as standard bioimaging probes than those that use visible/UV excitation.[8] Taking advantage of their distinct optical properties, the UCNPs of lanthanides have been developed and employed as a powerful

Md. Shahidul Islam

Dr Md. Shahidul Islam is a Professor in the Department of Chemistry at the University of Rajshahi, Bangladesh. He completed his BSc (Honours) in Chemistry and MSc in Organic Chemistry at the University of Rajshahi and earned his PhD in Drug Design and Synthesis from Kyushu Institute of Technology, Kitakyushu, Fukuoka, Japan. His academic and professional work focuses on organic chemistry, including peptide synthesis and drug design.

Hasan Ahmad

Dr Hasan Ahmad is a Professor of Chemistry specializing in polymer colloid chemistry. He earned his BSc (Honours) and MSc in Applied Chemistry from the University of Rajshahi, Bangladesh, and completed his Doctor of Engineering in Material Sciences at Kobe University, Japan. His research focuses on radical and controlled radical polymerization, functional polymer particles, conducting polymers, inorganic/organic composite microspheres, energy storage materials, and high-value products derived from natural fibers.

O. Thompson Mefford

Dr O. Thompson Mefford is an Associate Professor at Clemson University, specializing in polymers, nanomaterials, magnetism, and environmental applications. He earned his B.S. in Textile and Polymer Chemistry from Clemson University (2003) and his PhD in Macromolecular Science and Engineering from Virginia Tech (2007). His research focuses on polymer–metal oxide nanoparticle complexes and composites for biomedical, environmental, and energy applications, including hyperthermia and additive manufacturing in tissue engineering.

Md. Mahbubor Rahman

Dr Md. Mahbubor Rahman is a Professor of Chemistry. He completed his MSc at the University of Rajshahi, Bangladesh, followed by a PhD in France and postdoctoral research in Belgium. His research focuses on iron oxide magnetic nanoparticles for drug delivery, MRI, and hyperthermia, as well as polymer colloids, stimuli-responsive polymers, and luminescent nanoparticles for biomedical applications, aiming to develop advanced functional nanomaterials for healthcare and bioengineering.

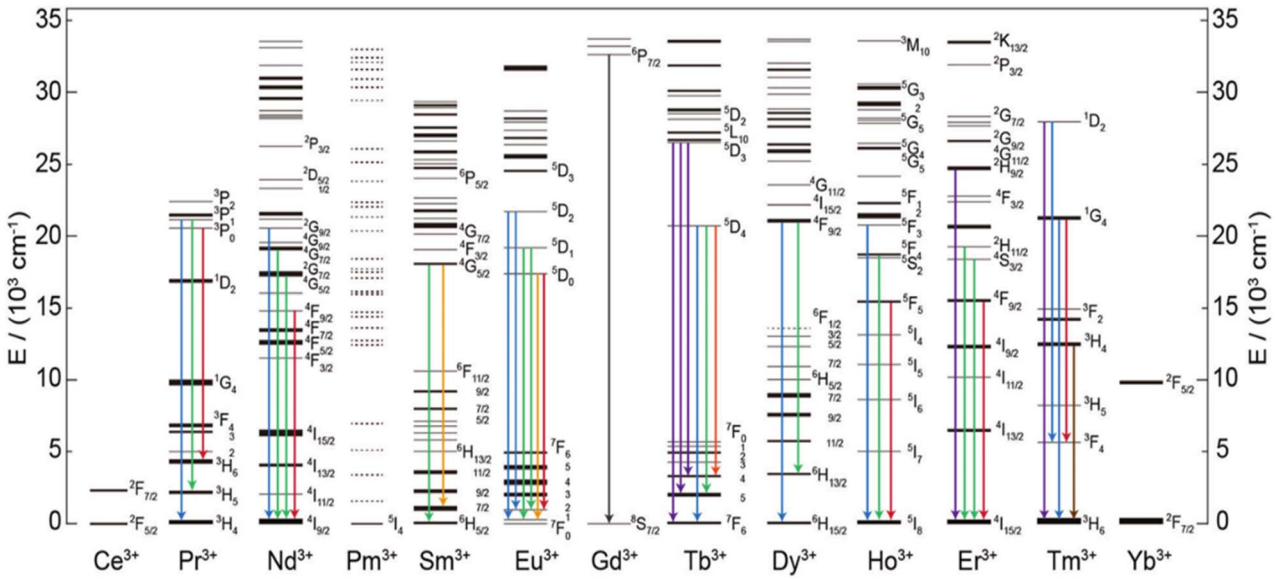

Fig. 1 A partial energy level diagram of lanthanide ions commonly used for achieving upconversion emission. The radiative transitions corresponding to typical emissions are highlighted.

tool in photodynamic[9] and photothermal[10] therapeutic treatments.

In addition to Ln nanoparticles, iron oxide nanoparticles (IONPs)have attracted a lot of attention in several sectors due to their unique nanoscale physicochemical features with magnetic properties. Although they lack the characteristic photoluminescent (PL) properties typically observed in lanthanide complexes and nanoparticles, their strong magnetic behavior and low toxicity provide the potential for a wide range of applications, including magnetic separation, magnetic hyperthermia, and contrast agents for magnetic resonance imaging. Since iron is an essential element in the human body, IONP-based contrast agents, which have already been approved by the United States Food and Drug Administration (FDA, US), offer improved biocompatibility and safety profiles when compared to other contrast agents like gadolinium-based complexes. As a result, IONP-based contrast agents have earned increasing interest for application in MR imaging. In addition, the heat generation capacity due to the magnetic oscillation of IONPs promises the destruction of lesion cells through thermal induction in cancer treatment.[11] In magnetic hyperthermia, the tumor cells can be successfully destroyed by the heat generated from IONPs.[12] Therefore, combining magnetic and luminescence characteristics in a single nanocomposite platform may pave the way for versatile nanomaterials with distinct multimodal features. These nanoparticles (NPs) also have promise for a variety of applications such as targeted drug delivery, theranostics, bioimaging, MRI, and fluorescence microscopy. Organic dyes and quantum dots (QDs) are frequently combined with magnetic IONPs to provide more versatility; however, both have some inherent drawbacks. Ln-based compounds, which feature distinctive emission bands, long luminescence lifetimes, and good photostability under photoexcitation, have recently been widely investigated as a new form of optical component.[13–18] To take advantage of their unique optical behaviors and magnetic properties, many efforts have been devoted to synthesizing nanocomposites that integrate both IONPs and Ln-NPs.

In this review, we discuss the overall advancement of lanthanide-based iron oxide nanoparticles (Ln-IONPs). The nanomaterials discussed herein include lanthanide-doped IONPs, polymer-based lanthanide-iron oxide nanocomposites, and inorganic matrix-based upconversion lanthanide-iron oxide nanomaterials. Owing to their optical and magnetic properties, Ln-IONPs have outstanding application potential as multimodal contrast agents,[19] dynamic opto-magnetic drug delivery vehicles,[20] and optical imaging-guided photothermal therapeutics.[21] A few studies are available on their cytotoxic profile, which are briefly discussed here. Particular emphasis has been placed on the changes in the magnetic and luminescence characteristics when iron oxide and lanthanide particles are combined, especially luminescence quenching, which is still seen as a major challenge in the combination of iron oxide and lanthanide nanoparticles. We also discuss various synthetic pathways that have been applied to resolve these issues. First, we briefly discuss the luminescence properties of Ln complexes and nanoparticles, along with some important factors that affect the luminescence and magnetic properties of Ln nanoparticles. Afterward, we briefly discuss the important properties of IONPs, which are necessary for specific applications in the biomedical field. Finally, we highlight Ln-IONPs, including their synthetic chemistry, optical and magnetic properties, *in vitro* and *in vivo* applications, limitations, and future scope.

2. Lanthanide complexes

In spite of the excellent luminescence properties of lanthanides, the light absorption ability of all Ln ions is very poor. Because

most of the transitions in the absorption spectra of trivalent Ln ions (Ln^{3+}) have molar absorption coefficients less than 10 L mol^{-1} cm^{-1}, only a modest quantity of light is absorbed by direct excitation in the 4f levels.[19] Weak light absorption results in weak luminescence because the luminescence intensity is proportional to both the luminescence quantum yield and the amount of light absorbed.[20] The antenna effect, on the other hand, can overcome the problem of low light absorption (or sensitization). The commonly used chromophore organic ligands that facilitate the sensitization of Ln light emission are known as "antennae" and are crucial in defining the emission intensity of the Ln^{3+}-ligand complexes. In general, any aromatic or hetero-aromatic highly conjugated systems with high light absorption (or extinction) efficiency can be used as antennae. Organic ligands can absorb more light than the Ln ion itself due to the intense absorption bands of organic chromophores. In coordination chemistry, the design of Ln organic ligand complexes as effective light conversion molecular devices (LCMD) has become a research field of interest. The widely recognized mechanism for transferring energy from organic ligands to the Ln ion has been suggested by Crosby and Whan.[21–23] As illustrated in Fig. 2(a), the ground state molecules of organic ligands are excited to the first excited singlet state ($S_0 \rightarrow S_1$) when the Ln-ligand complexes are exposed to ultraviolet radiation. Through interactions with solvent molecules, the ligands undergo rapid internal transitions to the lower vibrational levels of the S_1 state. The excited singlet state can be deactivated radiatively to the ground state (molecular fluorescence, $S_1 \rightarrow S_0$) or nonradiatively to the triplet state T_1 by intersystem crossing (ISC). The spin-prohibited transition $T_1 \rightarrow S_0$ can deactivate the triplet state T_1 radiatively to the ground state S_0, resulting in molecular phosphorescence. Alternatively, the complex could make a nonradiative transition through an energy transfer from the triplet state of the organic ligand to the excited state of the Ln ions. The Ln ions may then undergo a radiative transition to a lower 4f state *via* characteristic line-like photoluminescence after this indirect stimulation by energy transfer, or they may be deactivated by nonradiative processes. In order to populate a Ln ion's resonance level, the lowest triplet state of the complex must have an energy almost equal to or higher than the Ln ion's resonance level, but not lower. When the energy levels of organic ligands fall below the resonance level of the Ln ion, the ligand exhibits molecular fluorescence or phosphorescence, or no light emission at all. A close match between the triplet state energy level and the receiving 4f energy level of the Ln ion is also undesirable since energy back transfer from the Ln ion to the triplet state is possible. For example, Whan and coworkers observed energy back transfer from the excited Tb^{3+} ion to the ligand when the energy difference between the lowest triplet state of the ligand and the $^5D_4$ level of Tb^{3+} was smaller than 1850 cm^{-1}.[22]

A reference scheme for the back energy transfer is provided in Fig. 2b.[24–26] As the energy gap widens, the energy transmitted from the triplet travels through the metal's non-radiative excited states until it reaches the emissive levels where metal-centered emission occurs. On the other hand, because of thermal deactivation as a result of reverse energy transfer, a smaller energy gap severely reduces the emission quantum yield. Charge-transfer states are another way to sensitize Ln luminescence.[27–29] This is especially true for redox-sensitive Ln ions like Sm^{3+}, Eu^{3+}, and Yb^{3+}, where light can be absorbed through a ligand-to-metal charge transfer (LMCT) state, from which the energy of the photon can be transmitted to the 4f levels of Ln ions. This technique is only effective if the LMCT

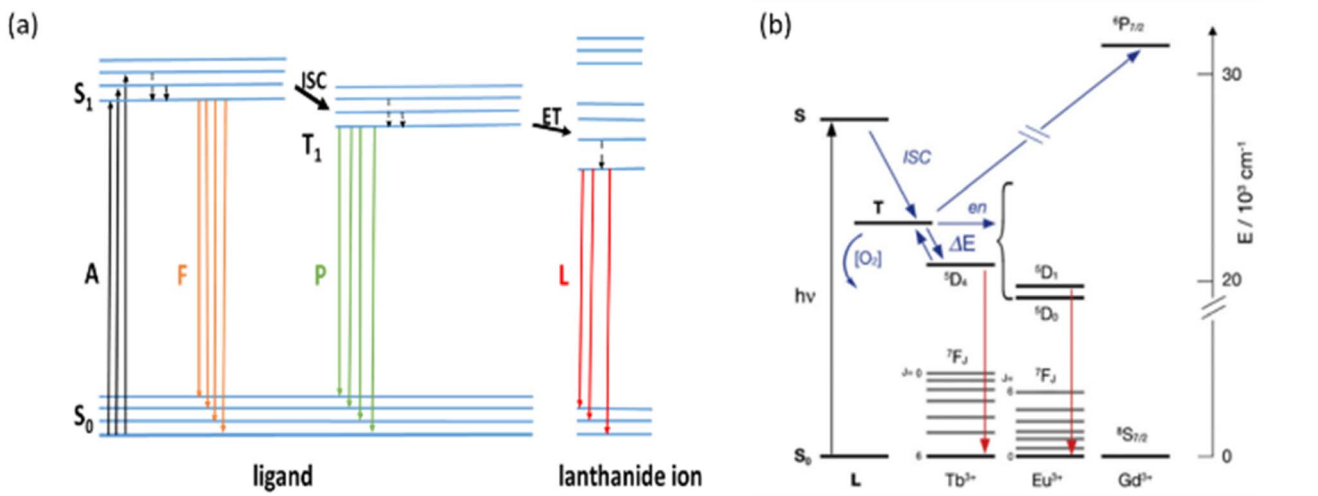

Fig. 2 (a) Schematic of photophysical processes in lanthanide(III) complexes (antenna effect). Abbreviations: A – absorption; F – fluorescence; P – phosphorescence; L – lanthanide-centered luminescence; ISC – intersystem crossing; ET – energy transfer; S – singlet state; and T – triplet state. Full vertical lines indicate radiative transitions and dotted vertical lines indicate nonradiative transitions. (b) Schematic of three cases with regard to energy transfer (en) as regulated by the energy gap (ΔE) between the triplet level (T) of the chromophore (L) and the emitting level of the cation: (i) when $\Delta E \leq 1500$ cm^{-1}, back energy transfer takes place and, consequently, O_2-effects (particularly intense in solution at room temperature given the long lifetime of the ligand triplet level) are observed; (ii) when $\Delta E \geq 1500$ cm^{-1}, energy transfer is complete; and (iii) energy transfer is exothermic and does not take place.

state is sufficiently energetic. Eu^{3+} sensitization *via* an LMCT state is effective if the energy difference is more than 40 000 cm^{-1}. Low-lying LMCT states will quench the luminescence partially or completely.[30] Metal-centered luminescence is completely quenched in Eu^{3+} if the LMCT energy is less than 25 000 cm^{-1} (Fig. 3).[19]

The position of the triplet level is dependent on the type of ligand; changing the ligand can vary the luminescence intensity seen for a particular Ln ion.[31] As a result, special attention should be devoted to the design of ligands to optimize the desired photoluminescence (PL) features. The Ln^{3+} ion and ligand interaction must be increased to boost the thermodynamic stability of the complex. Ln^{3+} cations prefer hard binding sites with significant electrostatic components because of their hard nature.[32]

2.1. Ln-complex of β-diketone

Anionic ligands such as carboxylates, phosphinates, phosphonates, and diketonates are widely used ligands for Ln ions. The β-diketones have strong absorptions for their π–π* transitions over a wide range of wavelengths, and have therefore been targeted for their capacity to sensitize the luminescence of the Ln(III) ions.[33] However, they are generally poor ligands for sensitizing the luminescence of terbium(III) ions, whereas most europium(III) β-diketone complexes display exceptionally bright luminosity. This is because many β-diketone ligands with aromatic substituents have a triplet level lower than that of the $^5D_4$ resonance level of terbium ions. However, the tris complexes of acetylacetone, di-*p*-fluorodibenzoylmethane, and trifluoroacetylacetone show significant luminescence with terbium(III) β-diketone complexes.[31] Among them, terbium(III) complexes of acetylacetone showed the maximum luminescence intensity.[34]

On the other hand, because of the large energy gap between the Eu^{3+} ion's resonance levels and the triplet state of the ligand, aliphatic β-diketone ligands (acetylacetone, trifluoroacetylacetone, or hexafluoroacetylacetone) give weakly luminescent europium(III) complexes.[31] When the β-diketone ligand combines with both aromatic and aliphatic substituents such as benzoylacetone, benzoyltrifluoroacetone, and 2-thenoyltrifluoroacetone (Fig. 4), they generate Eu(III) complexes with brighter luminescence. This is attributed to the more efficient energy transfer from the ligand to the Ln ion within the systems and also to the enhanced anisotropy around the europium(III) ion to increase luminescence intensity in such systems.[31]

Ancillary ligand-based β-diketone complexes, such as azobenzene-derived β-diketonate Ln(III) complexes[35] and unsubstituted monodentate pyrazole β-diketonate Ln(III) complexes,[36] have recently been attracting more attention for their multifunctionalities. The photoactivatable property was reported in a β-diketone complex with pyrrole rings.[37] In lanthanide hexafluoroacetyl acetonate, Eliseeva and coworkers[38] used 2,2'-bipyridine-*N*,*N*'-dioxide as an auxiliary ligand to avoid nonradiative deactivation pathways through harmonics of –OH vibrations. By controlling the orthogonal placement of the bis-β-diketone ligand, Li and colleagues[39] recently designed water-quenching resistant bis-β-diketonate europium(III) complexes. The photophysical properties of mono-diketonate and bis-diketonate Eu(III) complexes were compared, and it was found that the mono-diketone complex had a higher energy transfer efficiency from the ligand to the metal ion due to its lower site symmetry around the Eu(III) ion, and a lower non-radiative rate constant.[40]

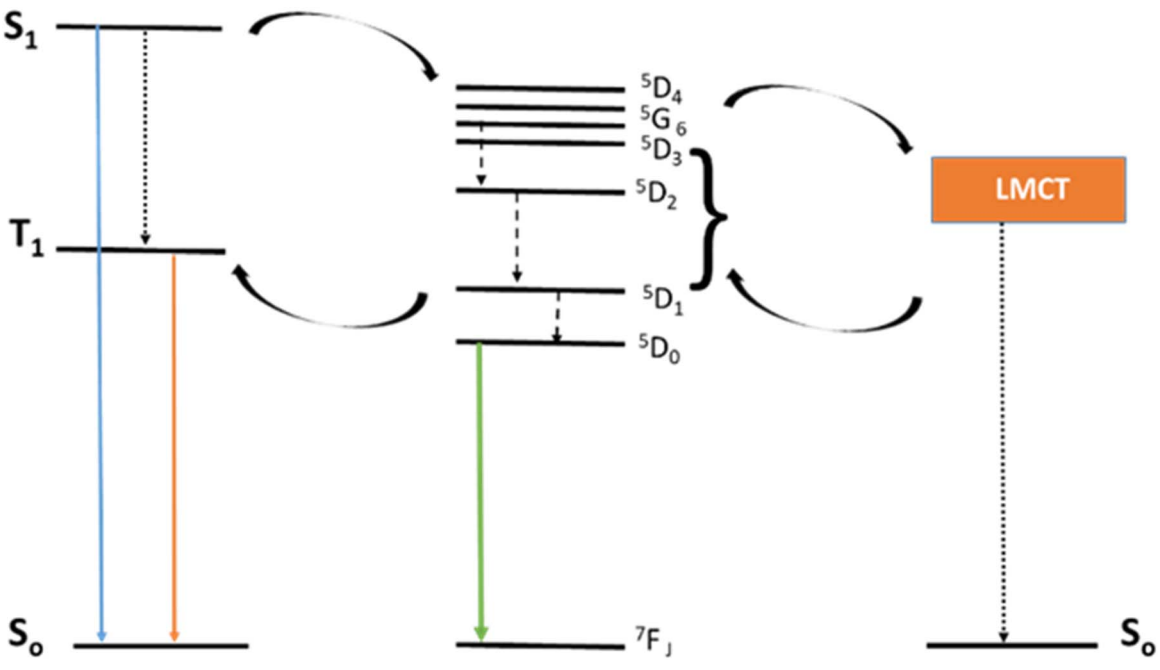

Fig. 3 Schematic of energy level diagram of an imaginary LMCT state. Full vertical lines indicate radiative transitions; dotted vertical lines indicate nonradiative transitions.

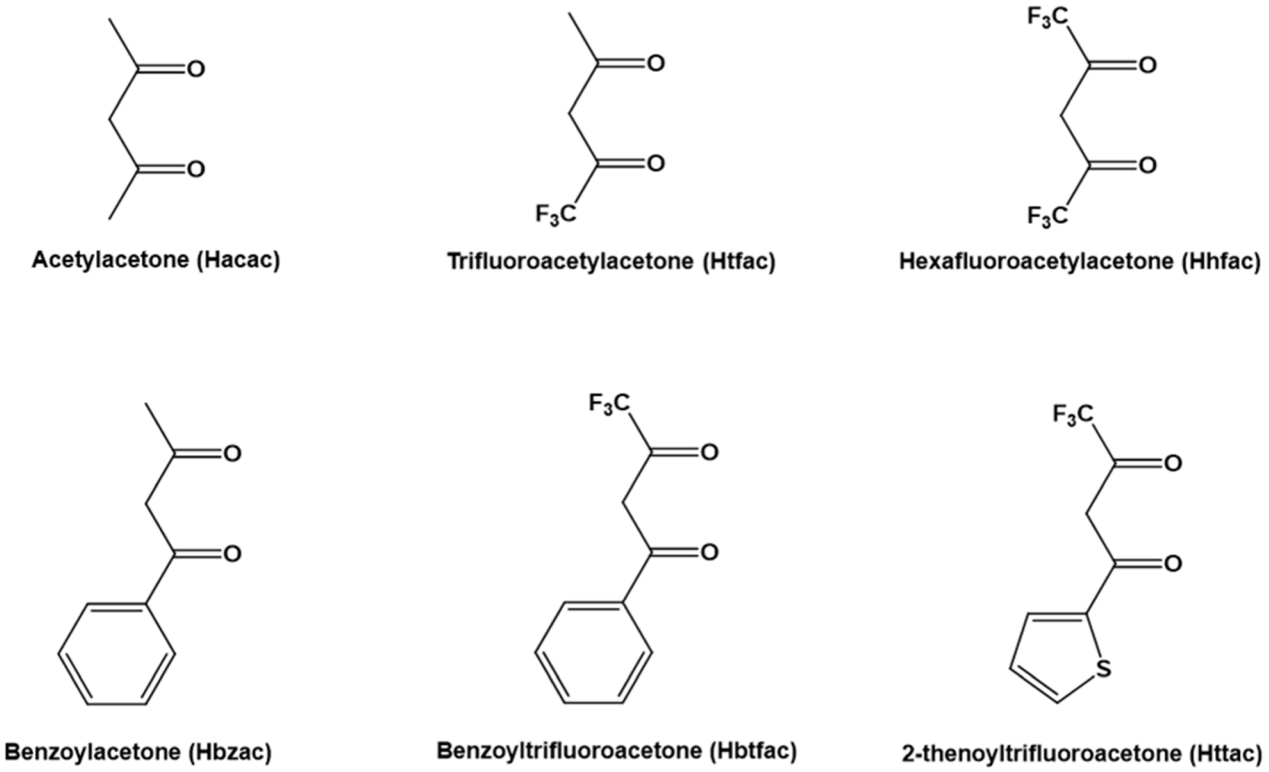

Fig. 4 Molecular structures of some aliphatic and aromatic β-diketone ligands for lanthanide complexes.

2.2. Ln-complexes of carboxylate ligands

In addition to β-diketones, carboxylate ligands (Fig. 5), such as 1,4,7,10-tetraazacyclododecane-1,4,7,10-tetraacetic acid (DOTA),[41] diethylenetriaminepentacetic acid (DTPA),[42–44] ethylenediaminetetraacetic acid (EDTA),[45–48] and some other ligands, such as N-heterocyclic ligands (*e.g.* pyridine, pyrazole),[49–52] phosphonate[53–55] and phosphine oxide,[56–58] are well known as light-harvesting antennae in lanthanide complexes.

2.3. Ln-complexes of supramolecular ligands

Ln ions, because of their electronic configurations, do not have significant coordination ability. As a result, traditional ligands are unable to form inert complexes, particularly in aqueous solutions where solvent molecules efficiently compete for coordination sites. Recent advances in supramolecular chemistry have made it possible to rationalize the production of ligands suited for Ln complexation, such as complexes

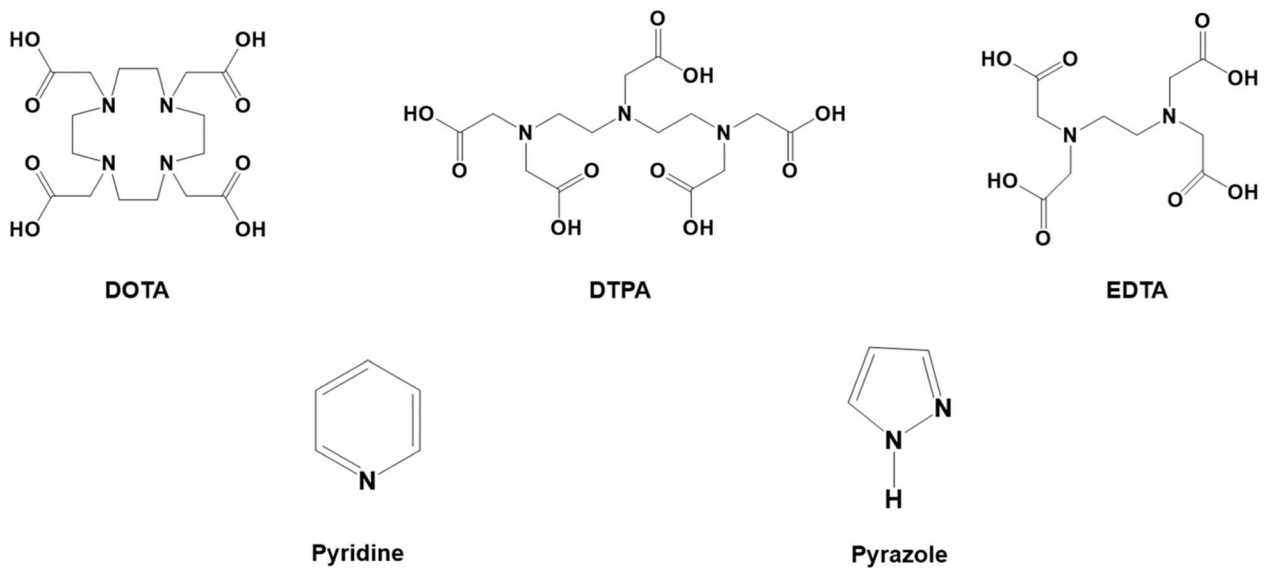

Fig. 5 Chemical structures of some common carboxylates and N-heterocyclic ligands for lanthanide complexes.

containing cryptands,[59–61] calixerenes,[62–64] and 2,2-bipyridine-based macrocyclic ligands[65,66] in which the ligand has a three-dimensional shape and creates a cage around the metal ion.

2.4. Ln-complexes of hybrid ligands

Sometimes, poor thermal stability and luminescence output limit the use of Ln-complexes, and therefore, the Ln-complexes are embedded in an inorganic host matrix. These hybrid materials outperform pure molecular Ln-complexes in terms of photostability, mechanical characteristics and processability. In recent methods, silicon alkoxides, *e.g.*, tetraethoxysilane (TEOS), 3-methacryloxypropyltrimethoxysilane (MAPTMS), 3-aminopropyltriethoxysilane (APTS), 3-glycidoxypropyltrimethoxysilane (GPTMS), *etc.*, have been hydrolyzed and condensed with N-heterocyclic ligands (*e.g.*, 1,10-phenanthroline and 2,2′-bipyridine) to build Schiff bases containing inorganic Si–O–Si networks that can strongly coordinate with Ln^{3+}.[67] Because many organotrialkoxysilanes do not polymerize to produce a gel, the tetraalkoxysilanes are utilized to ensure enough cross-linking in the sol to form a gel. The organic portion can contain an alkyl or aryl group, as well as a functional group such as an amino acid or isocyanate, epoxy, or vinyl groups. Armelao *et al.*[68] reported that Eu^{3+} and Tb^{3+}-based complexes composed of a macrocyclic ligand functionalized with distinct light-harvesting units (*e.g.*, phenanthroline and acetophenone derivatives) and anchored to silica layers showed significant luminescence brightness with quantum yields up to 0.25 for Eu^{3+}- and 0.45 for Tb^{3+}-based hybrids. Some nonvolatile liquids that can solubilize both Ln salts and ligands could also be confined within porous silica matrices to form organic–inorganic hybrid phosphors.[19] For example, polyethylene glycol (PEG-200) can solubilize large quantities of both Ln salts and bipyridine; when confined within silica, it forms a hybrid network that possesses improved luminescence intensities.[69,70] Ionic liquids have been investigated as novel solvents for studying the spectroscopic and photophysical characteristics of Ln ions. The photochemical stability of Ln-diketonate complexes dissolved in ionic liquids is higher than that of the identical complexes dissolved in standard organic solvents such as acetonitrile.[71] Ionic liquids are also used to produce ionogels, which are hybrid materials of ionic liquids encased in the nanoscale pores of a silica matrix;[72,73] they are utilized to fabricate novel luminous materials by incorporating Ln compounds.

In addition to the tetraalkoxysilane, organosilicon molecules with a vinyl group, such as vinyltrimethoxysilane or 3-(trimethoxysilyl)propyl methacrylate, can be added to the precursor solution.[74] Li *et al.* created a composite silicate-poly(methylmethacrylate) matrix doped with $[Eu(tta)_3(phen)]$.[75] Yan used a hybrid SiO_2/PMMA matrix to integrate $[Tb(acac)_3(dam)]$.[76] The emission intensity increased with Tb^{3+} concentration without any concentration-dependent quenching. In contrast, the luminescence intensity of the terbium(III) complex in pure poly(ethyl methacrylate), *i.e.*, the PEMA polymer matrix, reached its maximum at a Tb^{3+} concentration of 1%. The terbium(III) complex might be better distributed in the hybrid matrix than in the PEMA polymer, which explains the difference. Moreover, Park *et al.*[77] and Wang *et al.*[78] reported zeolites as a novel type of mesoporous organic–inorganic hybrids, which have remarkable phosphor properties. Zeolite microcrystals have also been synthesized using organic–inorganic functional linkers capable of coordinating and sensitizing Ln^{3+} ions, as well as self-assembling through hydrogen bonding to produce dense, homogeneous, well-oriented, stable, and highly ordered open-channel luminescent monolayers.[78]

Design implications for Ln-IONPs: from a materials design perspective, the photophysical principles governing lanthanide complexes provide direct guidelines for Ln-IONP construction. Efficient sensitization requires ligands with triplet energy levels positioned at least ~1500–2500 cm^{-1} above the emitting Ln^{+3} level to avoid back-energy transfer, a constraint that becomes more critical in proximity to iron oxide due to additional non-radiative pathways. Furthermore, the suppression of O–H and N–H vibrational quenching through rigid coordination environments or inorganic encapsulation is essential. These considerations rationalize the frequent adoption of silica, polymer, or inert fluoride buffer layers in Ln-IONPs (discussed in Section 6), where controlled spatial separation between the luminescent Ln domain and the iron oxide core preserves emission efficiency while retaining magnetic functionality.

3. Lanthanide nanohybrids

Compared to integrating Ln^{3+}-ligand complexes, embedding Ln^{3+} ions as guests in NP hosts (inorganic matrix) presents an appealing option for generating the pure colors of lanthanides, *e.g.* Y_2O_3:Yb^{3+}/Tm^3,[79] and $NaYF_4$:Yb^{3+}/Tm^3.[80] The stiff host lattices of Ln^{3+}-doped inorganic materials create a stable microenvironment for the Ln^{3+} emitter. Some host materials or other co-doping ions have a higher absorption coefficient than the Ln^{3+} emitter alone, allowing for efficient energy transfer to the Ln^{3+} ions. Consequently, upon stimulation, Ln^{3+}-doped inorganic materials can effectively produce luminescence ranging from the ultraviolet (UV) to the mid-infrared light spectrum. The inorganic matrix serves not only as a host crystal for the Ln^{3+} ions, but also as a sensitizer for their luminescence. These lanthanide-doped nanoparticles have been found to follow two emission processes, namely down-conversion (DC) and up-conversion (UC). The DC process is the conversion of higher energy photons into lower energy photons, which obeys Stokes' law, and the UC process generates a higher energy photon after absorbing two or more lower energy excitation photons.[81–83] A DC or UC system typically consists of an inorganic matrix (referred to as the host) and at least one active Ln^{3+} doping ion (activator). Generally, activators are co-doped with sensitizer ions that have a greater absorption coefficient to achieve more effective light emission. The most used DC activators are Eu^{3+}, Tb^{3+}, Sm^{3+}, and Dy^{3+}, all of which have abundant emission peaks in the entire visible region under UV excitation.[84–87] However, Ce^{3+} ions are found to be a most successful sensitizer in the DC process, because their emission band matches well with several f–f absorption bands of Ln^{3+} (Ln = Eu, Tb, Dy, and Sm) ions. The Ce^{3+}–Ln^{3+} pair has been used in

a myriad of phosphors to date, including $NaGdF_4$:Ce, Ln, $BaYF_5$:Ce, Tb, YPO_4:Ce, Tb, GdF_3:Ce, Ln, and $Sr_3Y_2(BO_3)_4$:Ce, Dy nano/microcrystals.[88–92] On the other hand, owing to the ladder-like energy levels, Er^{3+}, Tm^{3+}, and Ho^{3+} ions are the most common activators in the UC process, while Yb^{3+} ions are the most suited sensitizers for Er^{3+}, Tm^{3+}, and Ho^{3+} ions.[93] In both the DC[94–97] and UC processes[98–102] diverse combinations of emitters have been discovered to give intriguing multicolor emissions.

Design implications for Ln-IONPs: the behavior of lanthanide nanohybrids highlights the importance of host lattice rigidity, dopant distribution, and sensitizer–activator coupling in achieving efficient DC and UC emissions. For Ln-IONPs, these findings imply that embedding Ln^{+3} ions within crystalline fluoride or oxide hosts prior to integration with iron oxide is preferable to direct Ln doping into the iron oxide lattice, which often leads to luminescence quenching. Accordingly, many successful Ln-IONP designs adopt core–shell or heterostructured architectures in which a pre-optimized Ln nanophosphor is magnetically coupled but optically insulated from the iron oxide phase (discussed in Section 6).

4. Factors affecting the properties of Ln nanohybrids

4.1. Effects of particle size and shape

The size of the Ln-based nanoparticles has a significant effect on their optical properties. Van Veggel and co-workers[103] produced and evaluated three distinct nanometer-sized $NaYF_4$:Er^{3+} (2%), Yb^{3+} (20%) particles. Quantum yields (QY) for 100, 30 and 10 nm particles were 0.30, 0.10, and 0.005%, respectively. As the size of the NPs decreased, their surface area relative to their volume increased, resulting in a reduction in QYs. This is because when the size of the dopant ions is reduced, they get closer to the surface and are effectively quenched by the solvent molecule's higher energy vibrations. Conversely, the specific surface area decreases as size increases, which is beneficial for reducing nonradiative relaxation pathways.[104] J. Zhao, *et al.* investigated the UC emission decay curves in hexagonal $NaYF_4$:Yb, Er nanoparticles of various sizes.[105] When the particle size was reduced from 45 to 6 nm, both the green and red emission durations decreased monotonically (Fig. 6(a)). Consequently, as particle size decreased, the upconversion emission efficiency declined dramatically. The overall integrated upconversion fluorescence emission of $NaGdF_4$:Yb, Er nanoparticles increased with particle size (Fig. 6(b)).[106]

The magnetic properties of Ln nanoparticles have also been studied with respect to particle size. When the size of the ferromagnetic particles is lowered to a critical value, the magnetic property is no longer ferromagnetic but superparamagnetic. Because of the spin canting effect, the saturation magnetization (M_S) value of nanoparticles decreases as their size decreases, resulting in changes in MR relaxivities. It was revealed that[107] in four different sizes ranging from 2.5 to 8.0 nm of $NaGdF_4$ nanoparticles, the longitudinal relaxivity (r_1) value increased from 3.0 mM^{-1} s^{-1} to 7.2 mM^{-1} s^{-1} if the particle size was reduced. On the other hand, for $NaDyF_4$ NPs, the r_1 value remained constant as the size changed, but the transverse relaxivity (r_2) value increased as the size increased. Talham and coworkers synthesized three different-sized $Eu_{0.2}$-$Gd_{0.8}PO_4H_2O$ nanoparticles and observed that the longitudinal relaxivity (r_1) values increased with particle size, reaching 6.13 mM^{-1} s^{-1} for a sample of 40 ± 4 nm particles.[108] In addition to the size effect, interestingly, the shape of the host matrix also plays a significant role in emission behavior during the UC process. $NaYF_4$, for example, is one of the most effective host matrices for UC emissions. Two different emission ratios have been discovered when it is co-doped with Yb^{3+} and Er^{3+} in terms of the shape of the host matrix ($NaYF_4$).[109] Green emission was found to dominate in the spectrum profile of hexagonal $NaYF_4$ nanoparticles, resulting in green-colored output. However, in cubic $NaYF_4$ nanoparticles, a yellow color was discovered as an output result due to the red emission's comparability with the green emission.

4.2. Effects of surface modification

Surface modification by ligands or polymers alters the optical properties of Ln-based nanoparticles by affecting some phenomena, including light scattering, vibrational stretching, solvent–surface interaction, and colloidal stability. The luminescence intensity of UCNP@SiO_2–NH_2 particles was lower than that of OA-UCNPs.[110] This decrease can be attributed to the presence of a silica layer, which may scatter light during both the excitation and emission processes. Another reason could be the strong Si–O stretching, which results in non-radiative multiphoton relaxation.[111–114] The reduced luminescence intensity in Ln-based nanoparticles functionalized with organic species, *e.g.*, ligands or polymers, could be due to a nonradiative transition triggered by high vibrational frequencies. Polyaminodextran (AMD)- and polyacrylic acid (PAA)-functionalized Eu:$GdVO_4$ nanocrystals[115] displayed charge transfer (CT) bands with lower intensities compared to unfunctionalized nanoparticles, as shown in Fig. 7(I). Stephan and co-workers have shown that coating with different organic species decreased the UC intensity to different extents.[116] Using OA-coated UCNPs as a reference, researchers discovered that alendronate-coated UCNPs reduced UC intensity by 33%, while PEG-phosphate- and *O*-phospho-L-threonine (OPLT)-coated UCNPs reduced UC intensity by 16% and 6.6%, respectively. The thickness of the shell layer also has a significant impact on UC emission behavior. The intensity of the emission appeared to increase as the shell thickness increased. This phenomenon could be attributed to an increase in colloidal stability or a decrease in the contact between the solvent and the surface of UCNPs. In the case of $NaYF_4$:Yb, Er@$NaYF_4$ core/shell nanocrystals with thicknesses ranging from 0.7 to 2.1 nm, the intensity of Er^{3+} emission was found to increase as the shell thickness increased, as shown in Fig. 7(II).[117] Likewise, the magnetization of NPs is also influenced by diamagnetic surface coatings on magnetic nanoparticles, reducing the saturation magnetization value. The value of M_S was increased by

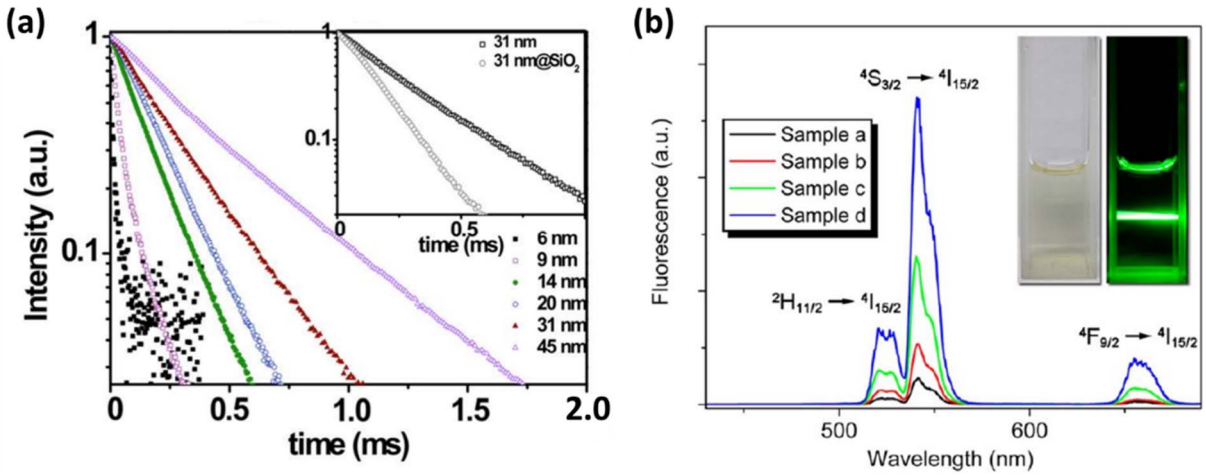

Fig. 6 (a) Evolution of lifetime decays for a series of $NaYF_4$:Yb, Er nanocrystals at the green upconversion emission bands. Inset indicates the lifetime variation of green upconversion luminescence for 31 nm nanocrystals after coating with a ~10 nm-thick silica layer. (b) Normalized fluorescence spectra of sample a (11.5 nm), sample b (14.6 nm), sample c (24.6 nm), and sample d (36.7 nm), recorded upon excitation by a CW 980 nm laser. Inset shows photographs of a cyclohexane solution of sample c taken under ambient light (left) or in the dark under excitation by a 980 nm laser (right).

decreasing the thickness of the surface coating layer, which raised the value of r_2. As the relative coating thickness (L/a) was reduced from 3.5 ± 0.8 to 1.7 ± 0.4, the r_2 value for $NaHoF_4$ nanoparticles coated with PMAO–PEG increased from (7.6 ± 0.3) × 104 to (274.0 ± 6.9) × 104 mM^{-1} s^{-1} per nanoparticle.[118]

4.3. Effects of doping materials

The optical characteristics of a material can be tuned by co-doping Ln ions with other Ln ions.[119,120] The distance between two nearby activator ions and the ion's absorption cross-section are the two key parameters that determine UC processes in a singly-doped nanocrystal system. Most Ln activator ions exhibit low absorption cross-sections, which lead to poor pump efficiency and consequently, low overall UC efficiency in singly-doped UCNPs.

The UC mechanism of a singly-doped nanocrystal system with Er^{3+} ions doped in a $NaYF_4$ host matrix is shown in Fig. 8.[119] Strongly absorbing ions, known as sensitizers, which ensure efficient energy transfer to the activator, are frequently doped to improve the absorption of Ln-doped UCNPs. In order to take advantage of the energy transfer upconversion (ETU) process between ions, singly-excited ions with a suitably broad

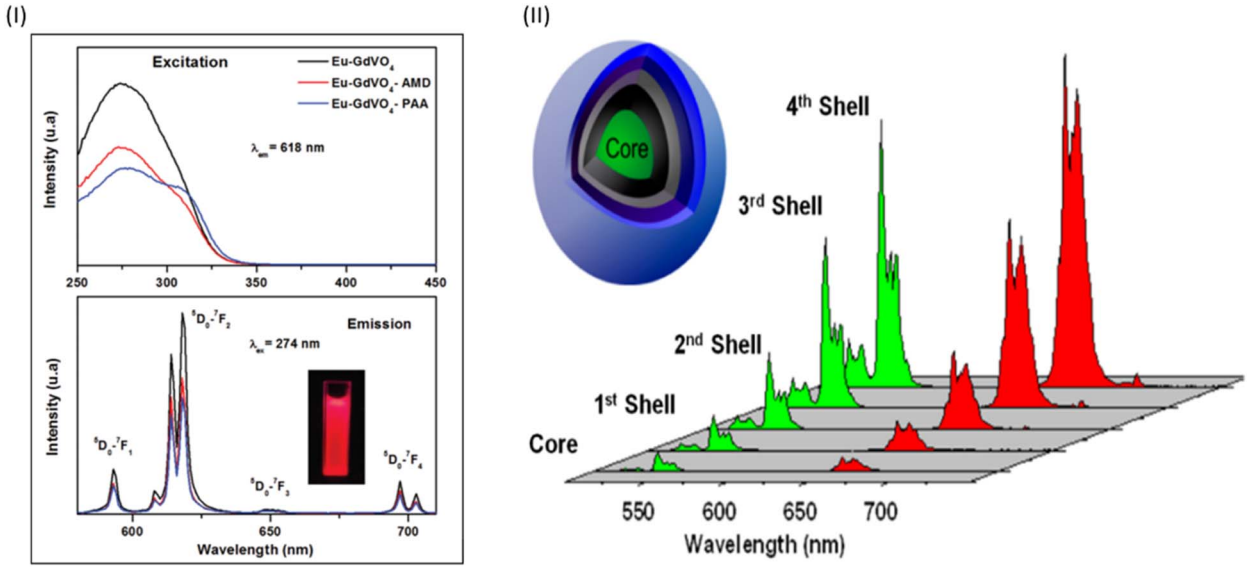

Fig. 7 (I) Excitation spectra (λ_{ex} = 618 nm) (top) and emission spectra (λ_{em} = 274 nm) (bottom) recorded for unfunctionalized and functionalized $Eu_{0.10}Gd_{0.90}VO_4$ nanoparticles. (Inset) Photograph of an aqueous dispersion of $Eu_{0.10}Gd_{0.90}VO_4$ functionalized with PAA under UV (λ = 312 nm) illumination. (II) Upconversion emission spectra of hexane dispersions of core and core–shell NCs with the same concentration of NCs under 980 nm excitation.

absorption cross-section in the NIR region, known as sensitizers, are usually co-doped with the activator. The Yb^{3+}/Er^{3+} combination is a typical example of a sensitizer–activator combination, in which a Yb^{3+} sensitizer is co-doped with an Er^{3+} activator (emitter) to take advantage of the Yb^{3+} ion's high absorption cross section at 980 nm, as well as the Er^{3+} ion's strong emission at visible wavelengths.[120–122] The Yb^{3+} ions absorb most of the incident light due to their higher doping density and wider absorption cross-section. When Ln ions are co-doped with additional Ln ions, the UC pathways grow more complicated, frequently involving several energy transfer processes between the dopants.[119,123] Furthermore, co-doping Er^{3+} with Tm^{3+} or Ho^{3+} reduces green Er^{3+} emission while increasing red emission at 660 nm.[119]

A preliminary examination of over 300 dopant combinations was conducted that revealed some binary and ternary combinations, such as (Er^{3+}/Pr^{3+}, $Yb^{3+}/Er^{3+}/Pr^{3+}$, Er^{3+}/Sm^{3+}) and (Er^{3+}/Tm^{3+}, $Er^{3+}/Tm^{3+}/Gd^{3+}$, Er^{3+}/Ho^{3+}), which produce pure green and pure red emission, respectively, when excited at 980 nm.[124] Multiphonon cross-relaxation processes account for the enhanced red emission in Er^{3+}–Ho^{3+} and Er^{3+}–Tm^{3+} codoped nanoparticles. High doping levels could cause harmful cross-relaxation, resulting in excitation energy quenching; to avoid this quenching effect, the concentration of activator ions should be kept low and properly regulated. Yan and coworkers investigated the UC emission characteristics of hexagonal phased $NaYF_4$:Yb, Er nanoparticles with varying Yb^{3+} and Er^{3+} doping concentrations.[109] It was discovered that as the doping concentration of Yb^{3+} and Er^{3+} increased, the red-to-green emission ratio of Er^{3+} increased. Tan and colleagues explored the UC emissions from nanoparticles with substantial activator doping in a recent study.[125] The red-to-green emission ratio of Er^{3+} considerably improved when the doping concentration of Er^{3+} increased from 1% to 50%, with the color output moving from green to red. Another technique to improve the emission ratio is to combine numerous activators. Chan and co-workers used a combinatorial approach for emissions from UC nanoparticles with dual activators (Er^{3+}/Sm^{3+}, Er^{3+}/Ho^{3+} and Er^{3+}/Tm^{3+}).[119]

4.4. Effect of temperature

Temperature (T) is an important factor that influences not only the quality of particle production but also the phosphor's ultimate luminous performance. T-Dependent emission is seen in almost all luminous compounds and materials.[126] T is connected to the rate of non-radiative transitions (k_{nrt}) *via* the Arrhenius equation:

$$k_{nrt} \sim e^{(-\Delta E/RT)} \quad (1)$$

According to this equation, the non-radiative transition rate increases at higher T.

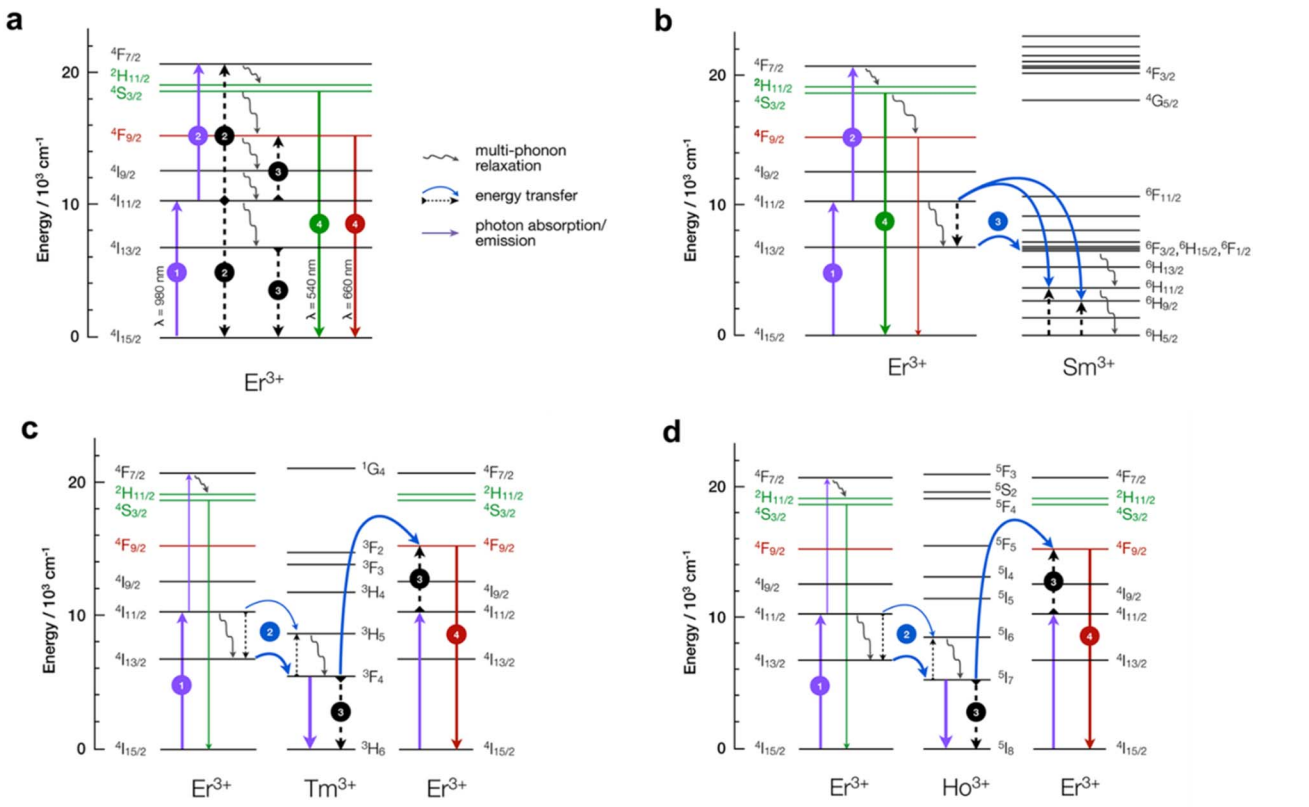

Fig. 8 Energy-transfer routes responsible for spectrally selective emission. Schematic of upconversion luminescence mechanisms in $NaYF_4$ nanocrystals doped with Er^{3+} only (a), Er^{3+}/Sm^{3+} (b), Er^{3+}/Ho^{3+} (c), and Er^{3+}/Tm^{3+} (d), each at a dopant concentration of 2 mol%. The arrows indicate the dominant excitation and relaxation transitions governing the population and depopulation of the energy manifolds contributing to visible emission, as derived from kinetic modeling under 980 nm excitation (λ_{ex} = 980 nm and power density = 10 W cm^{-2}).

The quantum yield (QY) of luminescence decreases with increasing T, according to eqn (2):

$$QY = \frac{\Gamma}{\Gamma + k_{\mathrm{nrt}}} \quad (2)$$

The average time a luminophore remains in its excited state prior to deactivation is defined as the luminescence lifetime (decay time, τ). With increasing T, the lifetime is thermally quenched *via* eqn (3):

$$\tau = \frac{1}{\Gamma + k_{\mathrm{nrt}}} \quad (3)$$

In mathematical terms, luminescence intensity at any time can be expressed by eqn (4):

$$I = I_0 e^{(-t/\tau)} \quad (4)$$

Therefore, with increasing temperature, the intensity decreases as the lifetime decreases.

The emission intensity of cubic phase (α-phase) $NaYF_4$:Yb/Er UCNPs has been observed to be quenched monotonously with increasing the temperature from 10 to 400 K.[127] The up-conversion luminescence (UCL) intensity of Er^{3+} ions increases with increasing temperature in β-phase UCNPs, reaches an optimum at a specific temperature, and subsequently drops with increasing temperature, as shown in Fig. 9(I). UCNPs are an attractive choice for thermal sensing because of their sharp temperature-dependent changes in spectral shape, luminescence lifetime, and luminescence intensity. In 2004, Shao and co-workers[128] reported the unusual behavior of emission increase with increasing temperature (from 25 to 125 °C) for small-sized (30 nm) UCNPs, as shown in Fig. 9(II). This deviation is attributed to the change in the process of phonon-assisted energy transfer. The phonon density increases with rising temperature in smaller nanoparticles, resulting in increased phonon-assisted energy transfer efficiency and improved UC luminescence efficiency.

4.5. Effect of pH

The fluorescence intensities of the NPs are sensitive to the pH of the medium. Singh and co-workers[129] observed that the fluorescence intensity of the HSA@PVP@Gd_2O_3:Eu^{3+} NPs declined progressively as the pH of the dispersion was reduced from pH 7 to pH 4, but the fluorescence intensity was drastically reduced at pH 3 (Fig. 10(a and b)). The fluorescence intensity of the NPs did not change a lot at alkaline pH. The decreased fluorescence of the NPs was observed as the pH of the aqueous dispersion fell below 7, owing to the effective breakdown of the NP structure by the hydronium ions, resulting in Gd^{3+} and Eu^{3+} ions leaching out of the NPs into the aqueous medium. For oleate-free Ln-doped upconverting $NaYF_4$:Er^{3+}/Yb^{3+} NPs, Capobianco and coworkers[130] found pH-dependent behavior; when the pH increased, the intensity of

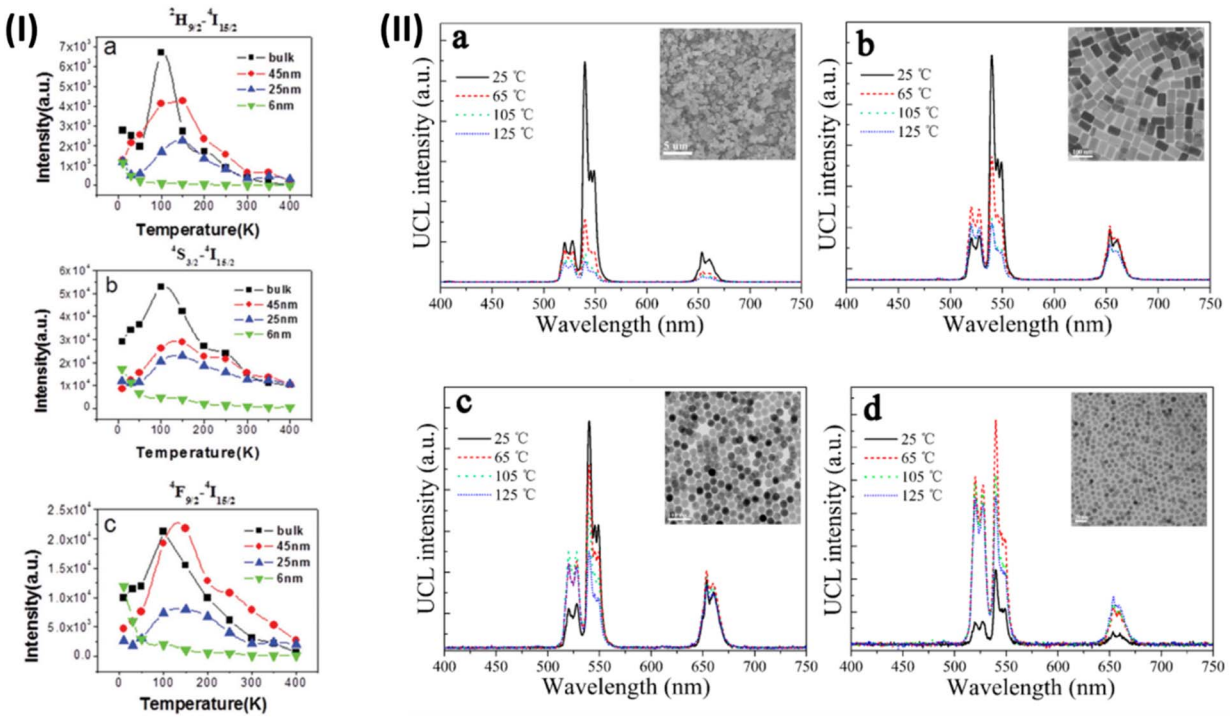

Fig. 9 (I) Comparison of the upconversion emission intensities of $NaYF_4$:Yb^{3+}, Er^{3+} in bulk and nanoparticle forms, measured as dry powders under 980 nm laser diode excitation at an identical power density (2.9 W mm^{-2}). Emissions in the blue (a), green (b), and red (c) regions were recorded over a temperature range of 10 K to 400 K under vacuum conditions. (II) Temperature-dependent upconversion luminescence spectra of (a) bulk $NaYF_4$:Yb^{3+}, Er^{3+}, (b) $NaYF_4$:Yb^{3+}, Er^{3+} UCNPs with dimensions of 66 × 48 nm, (c) 32 nm $NaYF_4$:Yb^{3+}, Er^{3+} UCNPs, and (d) 7 nm $NaGdF_4$:Yb^{3+}, Er^{3+} UCNPs. Insets show the corresponding SEM or TEM micrographs.

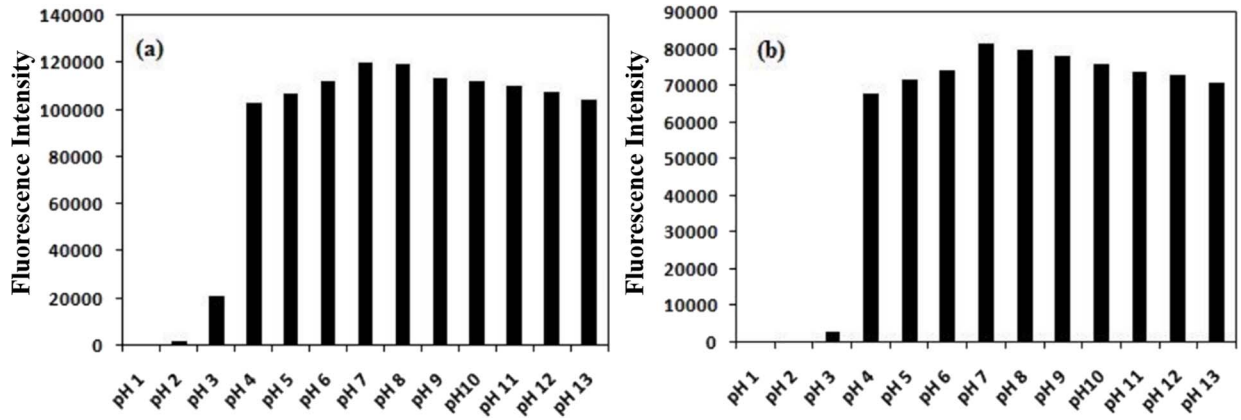

Fig. 10 Fluorescence intensity of (a) PVP@Gd_2O_3:Eu^{3+} NPs and (b) HSA@PVP@Gd_2O_3:Eu^{3+} NPs; dispersed in aqueous media of different pH.

the UC decreased. At low pH, the red emission of Ln-UCNPs is enhanced, with the highest red emission intensity recorded at pH 4 (Fig. 10 and 11).

4.6. Effect of solvent

The efficiency of light emission is greatly influenced by the solvent molecule. If there are high-energy vibrational groups on the surface of the solvent, the excited state can be populated by bridging the energy gap between two states *via* multiphonon relaxation. The presence of oscillator groups in the first coordination sphere of Ln(III) ions was discovered to extinguish the excited states of Ln(III) ions by enabling multiphonon relaxation.[131–133] Capobianco and colleagues[130] discovered that the green emission of hexagonal $NaYF_4$:Yb, Er NPs was greatly quenched by the multiphonon relaxation from various excited states of the Er^{3+} ions due to interactions with surface OH groups from water when the oleate ligands were removed in H_2O. Hydroxyl (OH) groups created vibrational modes at 3200–3600 cm^{-1}, which can be effective as oscillators in inducing the nonradiative relaxation processes of $^2H_{11/2} \rightarrow {}^4F_{9/2}$ and $^4I_{11/2} \rightarrow {}^4I_{15/2}$, which then quenched Er^{3+} green emission. The same team investigated the effects of using D_2O/DCl solution

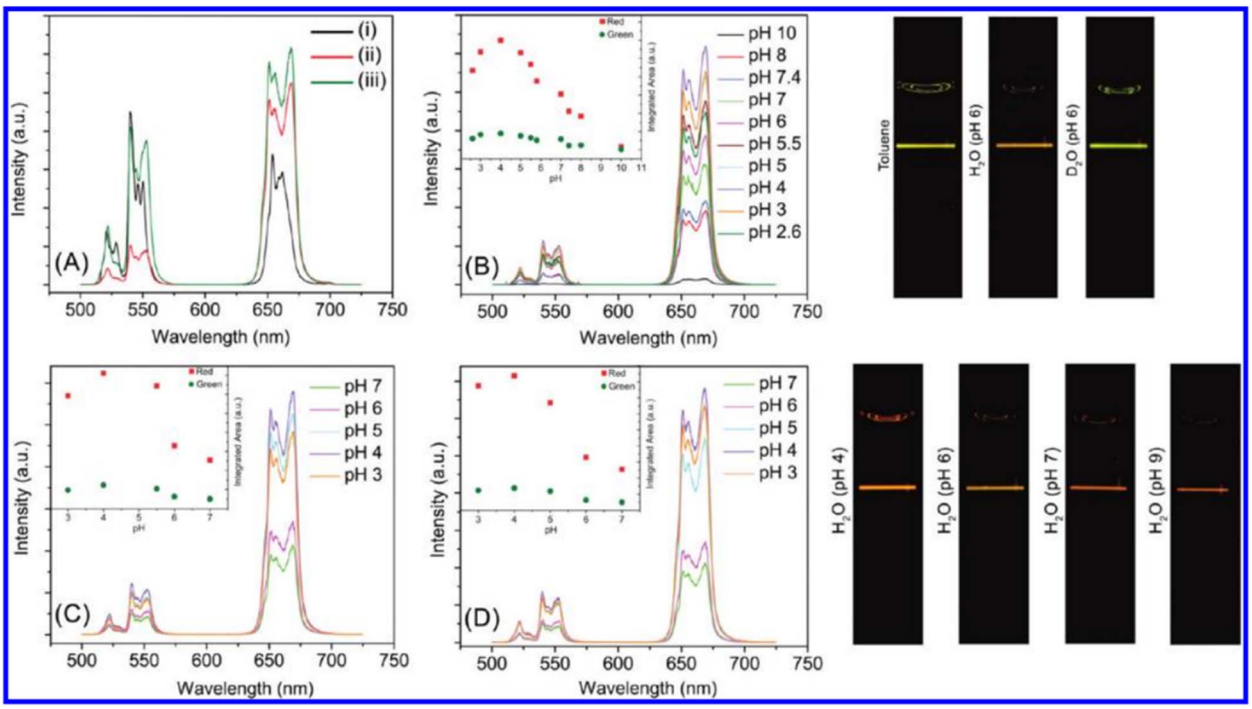

Fig. 11 (A) Upconversion luminescence spectra of oleate-capped Ln-UCNPs dispersed in (i) toluene, (ii) H_2O at pH 4, and (iii) D_2O at pD 4 under continuous wave excitation at 980 nm. The characteristic green emissions of Er^{3+}, centered at ~525 and ~550 nm, correspond to the $^2H_{11/2} \rightarrow {}^4I_{15/2}$ and $^4S_{3/2} \rightarrow {}^4I1_{5/2}$ transitions, respectively. The red emission band at ~660 nm originates from the $^4F_{9/2} \rightarrow {}^4I_{15/2}$ transition of Er^{3+}. (B–D) Influence of solution acidity on the upconversion luminescence of oleate-free Ln-UCNPs, with acidic environments prepared using (B) HCl, (C) HF, and (D) H_3PO_4. Photographs shown on the right highlight visually discernible variations in the red-to-green (R/G) emission ratios of the Ln-UCNPs across different solvents and pH conditions.

instead of H_2O as a solvent. When oleate-free nanoparticles dispersed in D_2O were compared to those dispersed in H_2O, the total UC intensity was higher. The multiphonon relaxation processes in D_2O are obviously lower because the O–D stretching vibration is 2600 cm^{-1}. Furthermore, increasing the DCl concentration results in an increase in the UC luminescence between pD 4 and 7. This finding supports the idea that D^+ plays a role in increasing the UC luminescence of Ln-UCNPs (Fig. 11).

Design implications for Ln-IONPs: collectively, size, surface chemistry, dopant concentration, temperature, pH, and solvent effects dictate the balance between radiative and nonradiative processes in lanthanide nanomaterials. In Ln-IONPs, these parameters must be co-optimized with magnetic requirements, as excessive surface functionalization or thick coatings can preserve luminescence at the expense of saturation magnetization, while insufficient separation leads to fluorescence quenching by iron oxide. These trade-offs underscore the need for rational architectural control—particularly, shell thickness, surface passivation, and dopant distribution in multifunctional Ln-IONPs designed for biomedical applications (discussed in Section 6).

5. Iron oxide magnetic nanoparticles

Iron oxide nanoparticles (IONPs) exist in different forms, such as hematite (α-Fe_2O_3), magnetite (Fe_3O_4), and maghemite (γ-Fe_2O_3). Among them, the most interesting are maghemite and magnetite due to their ferrimagnetic character, which by far surpasses the magnetic behavior of hematite. Magnetite (Fe_3O_4) is a common magnetic iron oxide having a cubic inverse spinel structure with oxygen forming a face-centered cubic (fcc) closed packing structure and Fe cations occupying interstitial tetrahedral sites and octahedral sites.[134] The structure of maghemite (γ-Fe_2O_3) is like that of magnetite, but it differs from Fe_3O_4 in that all of the Fe is in a trivalent state. The unit cell of γ-Fe_2O_3 is cubic, where eight cations occupy tetrahedral sites, and the remaining cations are randomly distributed along the octahedral sites.[135] Typically, α-Fe_2O_3, having a rhombohedral crystal structure, is antiferromagnetic in nature and exhibits weak ferromagnetism at room temperature, and its saturation magnetization (M_S) value is smaller than 1 emu g^{-1}, where γ-Fe_2O_3 and Fe_3O_4 exhibit ferrimagnetism at room temperature, and these M_S values can reach 92 emu g^{-1} (M_S value of bulk iron oxide materials).[136] Magnetite (Fe_3O_4) and maghemite (γ-Fe_2O_3) have a long-range ordering of magnetic moment. The internal magnetic field within the magnetic materials generates magnetostatic energy. Magnetostatic energy is lower in bulk magnetic materials as they consist of multiple domains within which the magnetic moments are parallel. Magnetic nanoparticles show their maximum coercivity at the transition from multi-domains to single domains, and the coercivity then decreases with decreasing size.[137] When the size of magnetic nanoparticles is extremely small, the individual particles have very small magnetic moments. Because of their small magnetic moments, extremely small magnetic nanoparticles exhibit an almost linear relationship between magnetization and the magnetic field of ~30 000 Oe, as shown in Fig. 12(i), which is very similar to the magnetic properties of paramagnetic materials. When the nanoparticles are small enough, superparamagnetism is observed. Superparamagnetic iron oxide nanoparticles (SPIONs) are single-domain magnetic iron oxide particles with diameters ranging from a few nanometers to <20 nm.[138–140] SPIONs show the M–H loops without exhibiting any hysteresis because the forward and backward magnetization curves coincide with each other, as shown in Fig. 12(ii). In the absence of an external magnetic field, SPIONs do not have

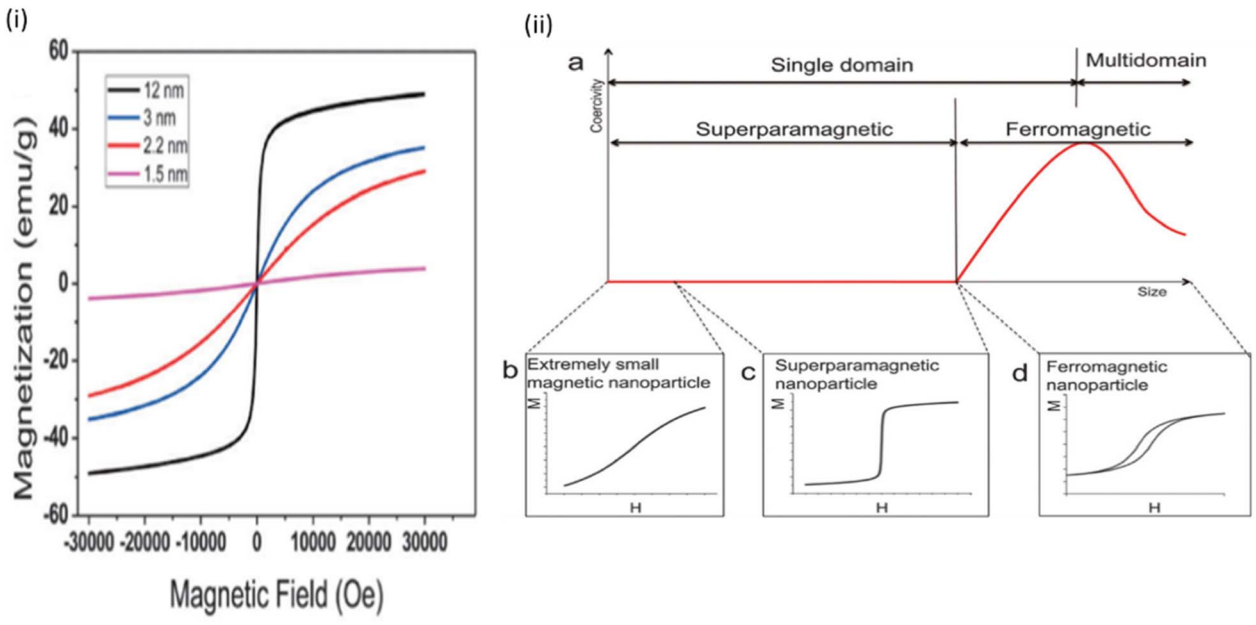

Fig. 12 (i) Field-dependent magnetization (M–H) curves of IONPs with diameters of 1.5 nm (pink), 2.2 nm (red), 3 nm (blue), and 12 nm (black) at 300 K. (ii) (a) Variation of coercivity with nanoparticle size. (b) M–H curve of extremely small magnetic nanoparticles. (c) M–H curve of superparamagnetic nanoparticles. (d) M–H curve of ferromagnetic nanoparticles.

permanent magnetic moments; however, they respond quickly to an external magnetic field and exhibit high saturation magnetization, like ferromagnetic and ferrimagnetic materials. When the magnetic field is removed, the entire system is demagnetized, and the nanoparticles exhibit no remanence of magnetization.

IONPs can yield photoluminescence (PL), although such an effect is rarely reported, most probably due to a weak PL signal. In a study, IONPs with sizes between 10 nm and 5 μm were observed to display PL peaks at 560 nm, 695 nm, and 840 nm, under excitation at 350 and 407 nm. These peaks were attributed to various recombinations of electrons at tetrahedral and octahedral Fe_3O_4 sites.[141] Furthermore, IONPs have a band structure that directly impacts their fluorescence properties. Indeed, the presence of an unfilled shell of Fe^{3+} and Fe^{2+} at the Fe_3O_4 surface,[142] where electrons can transfer from the fluorescent compound attached to them, leads to a mechanism of fluorescence quenching under laser excitation.[143]

6. Ln-based iron oxide nanoparticles (Ln-IONPs)

Ln elements are combined with IONPs to yield multiple features, such as optical and magnetic characteristics, in a single platform. Different methods have been employed to obtain maximum utility; for instance, some Ln elements are directly doped into the iron oxide crystal, and some are combined in the core–shell structure. Although some have been proven effective, most have failed to fulfill expectations. With growing knowledge, more efficient and effective composites have been fabricated in recent years, such as UCNP-based IONPs with enhanced color purity and iron oxide-induced quenching effects. Earlier down-conversion luminescence (DCL)-based IONPs used UV light for excitation, but it is now possible to use NIR-based excitation due to the development of UCNPs–IONPs nanocomposites. NIR excitation has been attracting more attention due to its high penetration depth in the human body and low energy that causes less harm to tissues. However, when iron oxide and Ln matrices are combined to produce a single multifunctional compound, their magnetic and optical properties change significantly due to the mutual impact between them. This phenomenon makes it quite challenging to design Ln-based iron oxide nanocomposites with high application efficacy. In the following section, we discuss the overall development and progress on Ln-based iron oxide nanocomposites.

6.1. Structural architectures of Ln-IONPs and their structure–property relationships

The unique multifunctionality of lanthanide-based iron oxide nanoparticles (Ln-IONPs) originates primarily from their structural configuration rather than from the intrinsic properties of individual components alone. Depending on how lanthanide emitters and iron oxide phases are spatially arranged, Ln-IONPs can be broadly classified into (i) Ln-doped iron oxide lattices, (ii) core–shell architectures, and (iii) heterostructured or composite assemblies. Each structural motif governs distinct optical and magnetic behaviors through interfacial coupling, energy transfer pathways, and magnetic dilution effects. In Ln-doped iron oxide systems, lanthanide ions are incorporated directly into the Fe_3O_4 or γ-Fe_2O_3 lattice. While this approach preserves compact particle size and strong magnetic coupling, it often leads to severe luminescence quenching due to non-radiative energy transfer from excited Ln^{3+} states to the dense electronic states of iron oxide. Consequently, such structures typically exhibit reduced emission intensity, despite maintaining superparamagnetic behavior. For example, yttrium-doped iron oxide nanoparticles synthesized *via* coprecipitation retained a phase-pure spinel structure,[144] as confirmed by XRD, with no secondary yttrium oxide phases detected, indicating successful dopant incorporation into the iron oxide lattice. Subtle diffraction peak shifts and broadening with increasing Y^{3+} content reflect lattice distortion arising from the ionic size mismatch between Y^{3+} and Fe^{3+}, while crystallite sizes remain within the single-domain nanoregime. TEM analysis reveals nearly spherical nanoparticles with narrow size distributions, showing that Y doping does not significantly alter particle morphology. Overall, yttrium ions are substitutionally accommodated within the spinel framework, inducing local structural strain without compromising crystallographic integrity. Another study reported the successful electrochemical synthesis of Y^{3+}-doped iron oxide nanoparticles (Y-IONPs) with controlled structural and morphological features.[145] X-ray diffraction (XRD) analysis confirmed that all samples crystallized predominantly in the inverse spinel iron oxide phase (magnetite/maghemite) without detectable secondary yttrium oxide phases, indicating that yttrium cations were effectively incorporated into the spinel lattice rather than forming separate crystalline compounds. Scanning and transmission electron microscopy (SEM/TEM) revealed that the nanoparticles exhibited a uniform, near-spherical morphology with narrow size distributions in the nanometer regime, and that Y^{3+}-doping had only a subtle influence on the particle shape and average size compared to undoped analogues. The combination of XRD and microscopic characterization thus demonstrated that yttrium incorporation induces minimal structural distortion while preserving high crystallinity and homogeneity, which underpins the observed enhancements in magnetic and electrochemical performance. Douglas and co-workers synthesized Gd-doped magnetite (Fe_3O_4) nanoparticles using a single-source iron/gadolinium polynuclear complex,[146] yielding well-defined octahedral nanoparticles with an average diameter of about 12.6 ± 2.6 nm. X-ray diffraction confirmed that the particles crystallize in the spinel magnetite structure, and the absence of additional diffraction peaks indicates that no separate Gd oxide phases were formed, implying the effective incorporation of Gd into the ferrite lattice. Transmission electron microscopy (TEM) showed (in Fig. 13) that the nanoparticles are uniform in shape and size with narrow distribution, demonstrating that the precursor-derived route produces highly crystalline, monodisperse nanocrystals. Overall, the structural analysis underscores that Gd was successfully integrated into the magnetite framework without disrupting its spinel symmetry, and the particles exhibit consistent octahedral morphology at the nanoscale.

Core–shell structured Ln-IONPs, in which an iron oxide core is separated from a lanthanide-doped shell (or *vice versa*), represent the most effective strategy for balancing magnetic

and optical performances (discussed in Section 7). The introduction of inert spacer layers such as SiO_2, polymer matrices, or fluoride shells suppresses interfacial quenching by increasing the spatial separation between the magnetic core and luminescent centers. This structural insulation preserves lanthanide emission while maintaining sufficient magnetic saturation for MRI or magnetic guidance. Heterostructured and composite Ln-IONPs, including dumbbell-like or satellite configurations, offer further flexibility by enabling the independent optimization of magnetic and optical domains. In these architectures, the minimized electronic overlap at interfaces allows efficient upconversion or down-conversion luminescence while retaining high relaxivity or hyperthermia efficiency. These systems demonstrate that multifunctionality in Ln-IONPs is fundamentally structure-driven. The coexistence of long-lived lanthanide luminescence and strong iron oxide magnetism within a single nanoplatform is inherently nontrivial, as magnetic materials typically act as fluorescence quenchers. In Ln-IONPs, this apparent contradiction is resolved through rational structural design, where spatial separation, interface engineering, and surface passivation regulate energy dissipation pathways. Luminescence efficiency is maximized by isolating Ln^{3+} emitters from iron oxide surfaces, while magnetic performance is preserved by minimizing excessive diamagnetic shell thickness. Thus, the exceptional multimodal performance of Ln-IONPs arises not from simple material combination but from precise nanoscale structural engineering.

A fundamental consideration in this context is that the factor governing luminescence quenching in lanthanide-based iron oxide nanoparticles (Ln-IONPs) is the distance-dependent nonradiative energy transfer between excited Ln^{3+} emitters and the iron oxide core. Two primary mechanisms are responsible for this process: Förster resonance energy transfer (FRET) and Dexter electron exchange. FRET arises from long-range dipole–dipole interactions and is effective over distances typically ranging from ~1 to 10 nm, depending on the spectral overlap between the lanthanide emission and the absorption profile of iron oxide, as well as the relative orientation of transition dipoles. In Ln-IONPs, the broad absorption of iron oxide enables it to act as an efficient energy acceptor, leading to significant luminescence loss when Ln^{3+} centers are located within the Förster radius (R_0). Consequently, spacer layers thinner than a few nanometers are generally insufficient to suppress FRET-induced quenching. At shorter distances (<1 nm), Dexter energy transfer

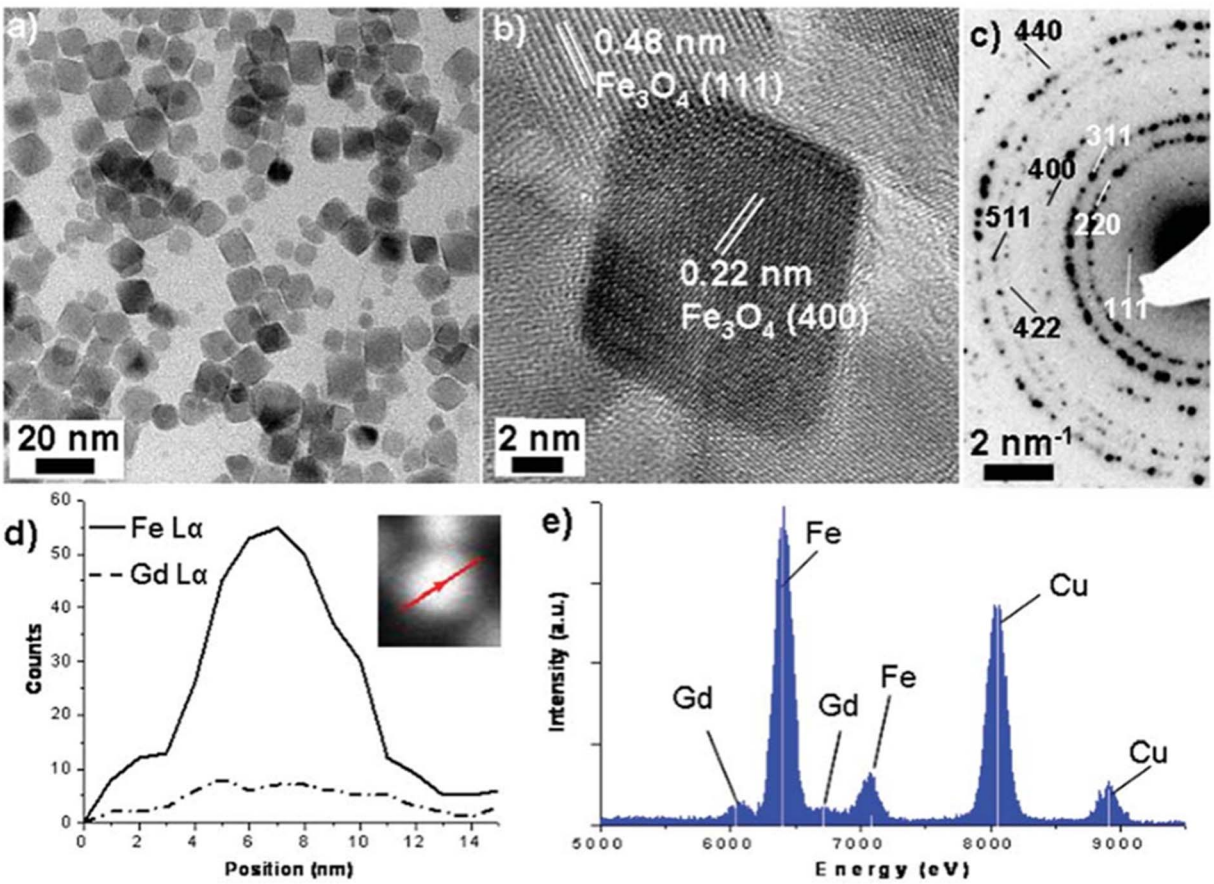

Fig. 13 TEM characterization of Gd:Fe_3O_4 nanoparticles. (a) Low-magnification TEM image showing predominantly octahedral particles. (b) HRTEM image of a representative octahedral nanoparticle with lattice fringes consistent with magnetite. (c) SAED pattern indexed to the Fe_3O_4 crystal structure. (d) STEM-EDX line scan across a single nanoparticle (inset: dark-field image) showing co-localized Fe and Gd Lα signals. (e) EDX spectrum from multiple nanoparticles confirming the presence of Fe and Gd; Cu peaks arise from the TEM grid.

dominates through direct wavefunction overlap, resulting in extremely efficient nonradiative decay. This mechanism explains the severe quenching observed in Ln-doped iron oxide lattices or systems lacking an effective insulating barrier. Complete suppression of Dexter transfer requires physical separation of the luminescent centers from the magnetic core by an electronically insulating layer. Based on these considerations, the introduction of inorganic (*e.g.*, SiO_2) or organic (*e.g.*, polymer) spacer layers with thicknesses typically exceeding ~5–10 nm significantly reduces nonradiative energy transfer, thereby preserving lanthanide luminescence. However, increasing spacer thickness also introduces trade-offs, including reduced magnetic saturation and increased hydrodynamic diameter. Therefore, the rational control of spacer thickness is essential to balance luminescence preservation and magnetic functionality in Ln-IONP design.

6.2. Synthetic methods of Ln-IONPs

The development of simple synthesis procedures for high-quality Ln-based iron oxide magnetic-luminescent NPs with regulated crystalline phases, shapes, and sizes is essential for tuning their physicochemical properties, which is favorable for potential bio-applications in a variety of disciplines. High-quality Ln-IONPs have been synthesized by using a wide range of chemical synthetic techniques, including thermal decomposition, coprecipitation, hydro(solvo)thermal synthesis, sol–gel process, microwave-assisted synthesis, *etc.* The three most popular approaches to producing high-quality Ln^{3+}-based IONPs are thermal decomposition, coprecipitation, and hydro(solvo)-thermal synthesis. Despite the many methods available for producing Ln^{3+}-based IONPs, it remains a significant challenge to synthesize a single micro or nano-composite system with enhanced luminescence and magnetic properties.

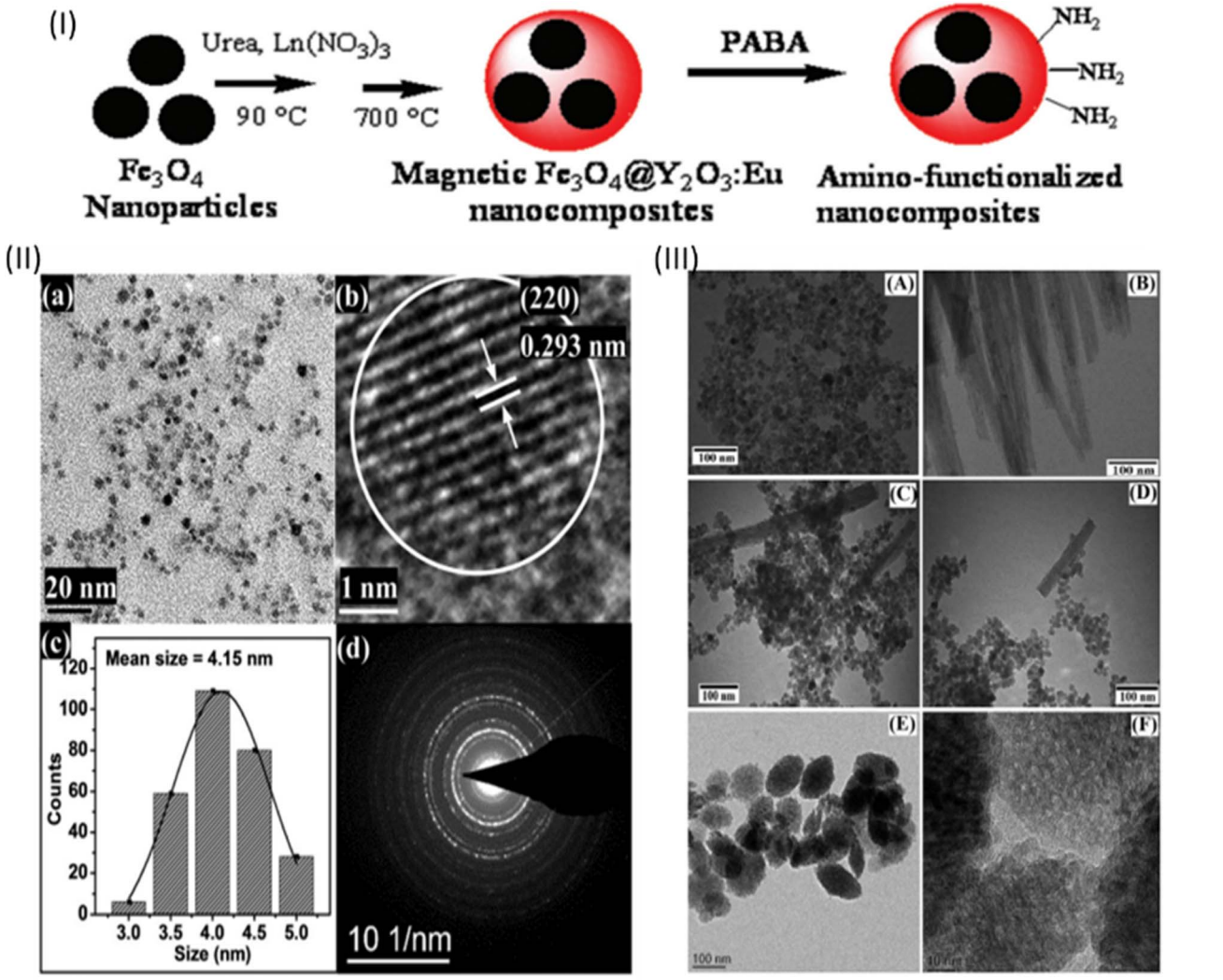

Fig. 14 (I) Schematic for the synthesis and surface modification of magnetic Fe_3O_4@Y_2O_3:Eu nanocomposites. (II) (a) Representative TEM image of highly uniform and well-dispersed Dy-doped γ-Fe_2O_3 nanoparticles at low magnification (scale bar = 20 nm). (b) HRTEM image of the particle with an interplanar distance of 0.293 nm corresponding to the (220) plane of the cubic maghemite. (c) Size distribution histogram with a mean diameter of approximately 4.15 nm acquired *via* Gaussian fits (250 recognizable particles randomly selected from some TEM images). (d) SAED patterns of the particles. (III) TEM images of (A) as-prepared Fe_3O_4, (B) YPO_4:Tb^{3+}, YPO_4:Tb^{3+}@ Fe_3O_4 in (C and D) the absence and (E and F) presence of PAMAM dendrimer.

The direct mixing of magnetic materials, such as Fe_3O_4 NPs, with luminescent materials causes fluorescence quenching effects.[147] In order to solve this issue, researchers have placed an inert layer between the magnetic core and Ln-doped NPs[148,149] and many others have explored modified systematic methods. The synthetic procedures for the preparation of Ln^{3+}-based IONPs, including some other methods that have been effectively exploited, are discussed below.

6.2.1. Coprecipitation method. One of the earliest and most convenient methods for producing Ln^{3+}-based nanocrystals is coprecipitation. With the help of a base in a solvent, the metal, in the form of the hydroxide, is precipitated from a salt precursor. The controlled release of anions and cations aids in the regulation of nucleation and particle growth kinetics, allowing the synthesis of monodisperse nanoparticles. It has several advantages over other technologies, including easy procedures, high product purity, low-cost equipment, and gentle operating conditions, such as the absence of organic solvents, surfactants, and high-temperature treatment. However, the crystallinity of nanoparticles generated by precipitation/coprecipitation in aqueous solution is rather poor, and further heat treatment is frequently required to improve product crystallinity.

Ma *et al.*[150] employed a simple homogeneous precipitation approach to make Fe_3O_4@Y_2O_3:Eu nanocomposites (NCs) with a core–shell structure, in which europium-doped yttrium oxide (Y_2O_3:Eu) acts as a shell around the Fe_3O_4 nanoparticle core, as shown in Fig. 14(I). Many more core–shell structures of Ln-based iron oxide particles have been reported over the years, such as Fe_3O_4@YPO_4:RE (RE = Tb and Eu),[151] Fe_3O_4/$BaMoO_4$:-Dy^{3+},[152] Fe_3O_4@*m*-SiO_2@YPO_4:Tb^{3+},[153] Fe_3O_4@SiO_2/GdOF:*x*Ce^{3+}, *y*Tb^{3+},[154] and Fe_3O_4@LaF_3:Yb^{3+}, Er^{3+}.[155] Sometimes Fe_3O_4 was used as a shell in Ln-IONPs. Srivastava and coworkers[156] synthesized the multifunctional YPO_4:Tb^{3+}@Fe_3O_4 nanohybrid material in the presence of a PAMAM dendrimer, where Fe_3O_4 functions as the shell and YPO_4:Tb^{3+} as the core. The PAMAM dendrimer was used to bind Fe_3O_4 and YPO_4:Tb^{3+} together, and a spindle shape was formed, as shown in Fig. 14(III).

6.2.2. Thermal decomposition method. One of the most popular methods for the synthesis of monodisperse, highly crystalline, well-defined, and phase-pure NCs is thermal decomposition. It is also the most effective approach to manufacturing high-quality NCs smaller than 10 nm, the size at which NCs can be easily removed from the body, and a larger dose can be used.[157,158] F. J. Douglas, *et al.*[159] used a unique single-source precursor (SSP), a bimetallic iron/gadolinium complex, to synthesize gadolinium-doped magnetite nanoparticles (Gd:Fe_3O_4) *via* thermal decomposition. Because bimetallic iron/gadolinium complex precursors can provide both the Ln^{3+} ions and the Fe_3O_4 source, the crystallization process from SSP is easy to manage. The particles are octahedral and well-defined with an average long axis length of 12.6 nm, as shown in Fig. 15(I). L. Yang, *et al.*[160] described the thermal breakdown of metal-oleate complexes to produce Eu-doped iron oxide (EuIO) nanocubes. The sizes of the EuIO nanocubes, *e.g.*, 10, 14, and 20 nm, were regulated by tuning the reflux temperature for 1.0, 1.5 and 2 h, respectively. TEM images revealed a consistent cubic shape with a restricted size distribution, as shown in Fig. 15(II). Shen *et al.*[161] prepared heteronanoparticles of magnetic Fe_3O_4 and Ln (Yb, Er)-doped $NaYF_4$ coupled with a 1,10-decanedicarboxylic acid (DDA) or 11-

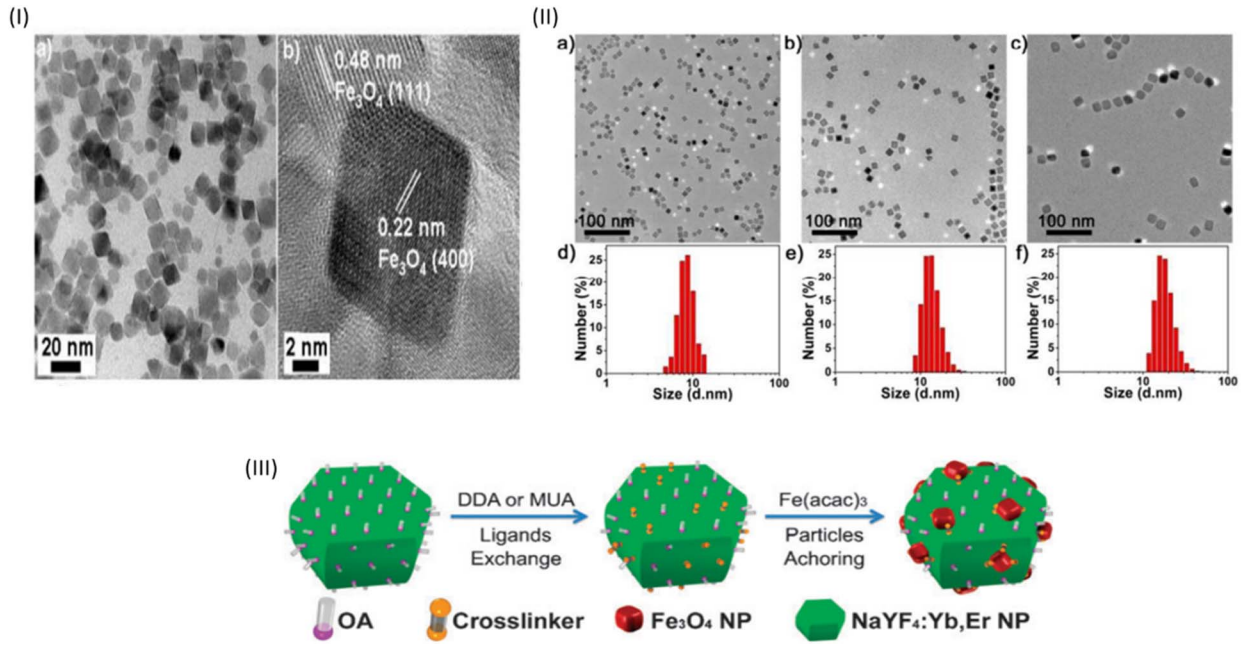

Fig. 15 (I) TEM analysis of the Gd:Fe_3O_4 particles, showing (a) an overview of the NPs with a clear prevalence of octahedral particles, (b) a high-resolution TEM image of a typical octahedral particle, annotated with fringe spacings that are consistent with those of magnetite. (II) TEM images (a–c) and the related DLS analysis profiles (d–f) of monodisperse EuIO nanocubes with different sizes: (a and d) 10.0 ± 1.7 nm, (b and e) 14.0 ± 1.9 nm, and (c and f) 20.1 ± 2.4 nm. (III) schematic of the crosslinker anchoring strategy for bifunctional Fe_3O_4/$NaYF_4$:Yb, Er hetero-NPs.

mercaptoundecanoic acid anchoring group (MUA). The DDA or MUA ligand binds to the OA capping layer and gives the UCNPs overhanging coordinative groups that are stable enough to withstand the thermolysis reaction, as shown in Fig. 15(III). Li and co-workers[162] prepared homogeneous and monodisperse core–shell $NaYF_4$:Yb^{3+}, Tm^{3+}@Fe_3O_4 nanocrystals with an average size of approximately 30 nm.

6.2.3. Hydrothermal/solvothermal method. The hydro(-solvo)thermal method is a typical solution-based chemical synthesis methodology in which reactions take place in a sealed environment at high pressure and temperature, usually above the solvent's critical point, to increase the solubility and reactivity of the inorganic substance. The ability to manufacture highly crystalline phases at considerably lower temperatures and to simultaneously conduct a set of reactions are two possible advantages of this technology over other types of synthetic procedures. The process has drawbacks, such as the necessity for specialized reaction vessels called autoclaves and the inability to watch the nanoparticles grow. In a conventional hydro(solvo)thermal synthesis, reaction precursors, solvents, and functionalized surfactants are combined and heated in a specific reaction vessel. Yang and colleagues[148] used a simple solvothermal approach to make Fe_3O_4@SiO_2@Y_2O_3:Eu^{3+} nanocomposites with a core–shell configuration. The nanoparticles were spherical in shape, with an average particle size of 262.36 nm, consisting of a magnetic core measuring around 210 nm in diameter and a silica shell measuring about 20 nm in thickness. Ln-based iron oxide submicron-rods have also been fabricated[163] and named Fe_3O_4/$NaYF_4$:Yb, Er, about 240 nm in width and 650 nm in length (Fig. 16).

6.2.4. Other synthetic procedures. In addition to the well-established synthetic procedures, many other novel methods have been developed to synthesize Ln-IONPs, including spray pyrolysis, ion-exchange, sol–gel, and microwave-assisted methods. In the following section, several typical studies on the synthesis of Ln-IONPs using these novel routes will be discussed.

The microwave-assisted approach, which can reduce the duration of chemical reactions from hours to minutes, has received a lot of attention in the last few years. The efficient in-core volumetric heating with microwave radiation causes heating directly inside the sample and reduces the reaction time.[164,165] Microwave dielectric heating has the advantages of a fast heating rate and uniform heating without thermal gradients, superheating of the solvents and selective heating features, when compared to traditional heating for chemical reactions.[166–168] N. Shrivastava, *et al.*[169] used a microwave-assisted approach to make core–shell structured Fe_3O_4/SiO_2/$NaGdF_4$:Ce, Eu and Fe_3O_4/SiO_2/$NaGdF_4$:Yb, Er nanoparticles. Small-sized Fe_3O_4/SiO_2/$NaGdF_4$:RE (RE = Ce, Eu, Yb, and Er) nanoparticles (15–20 nm) were formed. Furthermore, a consistent statistical size distribution was observed, with ovoidal forms of 17 nm. The ovoidal shape was attributed to the greater ratio of 1-ODE and OA in Fe_3O_4/SiO_2/$NaGdF_4$:RE compared to $NaGdF_4$:RE, which facilitated the formation or dissolution of RE(oleate) in the solvent by increasing the mobility. As a result, the growth rate of the nanoparticle increased along its radial axis, as opposed to parallel to the axial direction. Thus, the particle shape of Fe_3O_4/SiO_2/$NaGdF_4$:RE materials became more ovoidal. In the present system, despite all samples exhibiting paramagnetic or near-superparamagnetic behavior at room temperature, the ovoidal iron oxide cores display a slightly reduced saturation magnetization (M_S) relative to more isotropic morphologies. This reduction can be attributed to the combined effects of shape anisotropy and enhanced surface spin canting associated with anisotropic facets. Furthermore, the ovoidal morphology increases the surface-to-volume ratio and facet diversity, which enhances surface spin disorder at the iron oxide interface. These disordered surface spins do not fully align with the external magnetic field, thereby lowering the net magnetic moment. This effect becomes more pronounced after SiO_2 coating and $NaGdF_4$:RE shell formation, where interfacial strain and magnetic dilution further suppress magnetic coupling, as evidenced by the reduced magnetization values reported for iron oxide/SiO_2/$NaGdF_4$:RE nanoparticles. A few Ln-IONPs were synthesized using the sol–gel approach. Shen and colleagues[170] used the Stober sol–gel process to make dual-core@shell structured Fe_3O_4–$NaYF_4$@TiO_2 nanocomposites, as shown in Fig. 17(II). TiO_2 has multiple roles in these nanocomposites, including sonodynamic treatment, nucleus

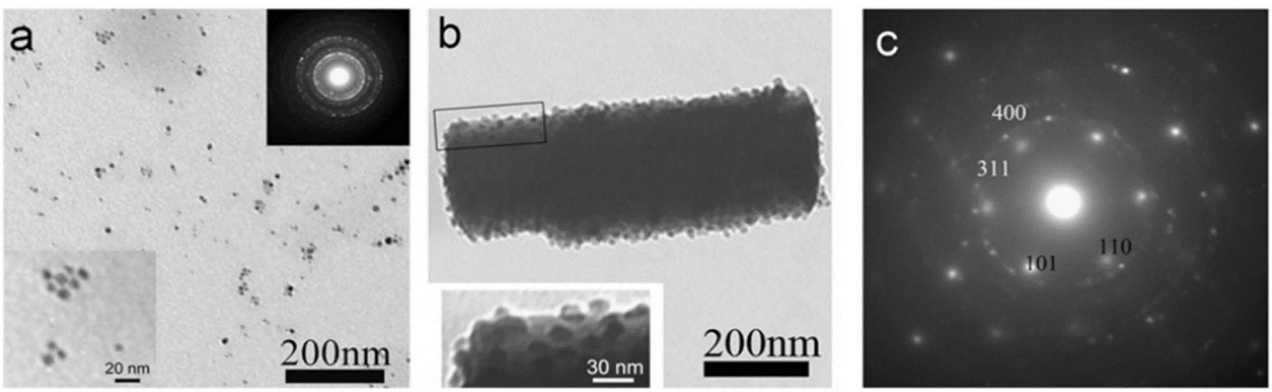

Fig. 16 TEM images of the obtained (a) Fe_3O_4 NPs and (b) Fe_3O_4/$NaYF_4$ hetero-submicro-rods. (c) SAED pattern of Fe_3O_4/$NaYF_4$ hetero-submicro-rods. The insets in (a) show the SAED pattern (right), and an amplified view (left) of Fe_3O_4 NPs. The inset in (b) shows an amplified view of the Fe_3O_4/$NaYF_4$ hetero-submicro-rods.

targeting, and chemotherapeutic medication loading. The self-ignited sol–gel process has been used to create Ho^{3+}-substituted $MnFe_2O_4$ ferrite samples.[171] S. Gai, *et al.*[149] used a two-step sol–gel procedure to create Fe_3O_4@*n*SiO_2@*m*SiO_2@$NaYF_4$:Yb^{3+}, Er^{3+}/Tm^{3+} nanocomposites having a core–shell structure. The nanocomposites were monodisperse and spherically shaped, having a narrow size distribution (around 80 nm) and mesoporous features, as well as visible lattice fringes in high-resolution transmission electron microscopy (HRTEM) images, indicating high crystallinity, as shown in Fig. 17(I). Ion-exchange technologies have also been utilized to create multifunctional Ln-IONPs. For example, F. Zhang, *et al.*[172] created Fe_3O_4@SiO_2@-NaYF/Yb, Er nanorattle hollow spheres with a Ln-doped $NaYF_4$ shell and a SiO_2-coated Fe_3O_4 inner particle, as shown in Fig. 17(III). The hollow core–shell structure has a diameter of 115 nm. Spray pyrolysis has also been reported to make Ln-based iron oxide nanocomposites like Fe_3O_4/Eu:Gd_2O_3.[173] Fe_3O_4 NPs were dispersed in a precursor solution of 20% $Eu(NO_3)_3$ and 80% $Gd(NO_3)_3$ in methanol, which was subsequently sprayed through a hydrogen flame. Spray pyrolysis has also been used to make multifunctional Co:Nd:Fe_2O_3/Gd_2O_3:Eu core–shell nanoparticles.[171]

The integration of polymers into the nanostructure is a novel strategy in the production of Ln-based iron oxide nanocomposites. A magnetic core can be encapsulated or inserted into a polymer matrix that has different luminous entities functionalized on it. For example, M. Runowski and S. Lis[174] created a polyacrylic acid-coated Ln-containing iron oxide nanocomposite (Fe_3O_4/SiO_2/NH_2/PAA/LnF_3). Under UV lamp irradiation, the resulting luminescent–magnetic compounds emit strong red or green emission concurrently. Thermo-responsive polymers have also been used to integrate Ln complexes with IONPs. For example, H. Zhu, *et al.*[175] employed $Eu(AA)_3$Phen-integrated poly(St-NIPAM) as a shell to make magnetic, fluorescent, and thermo-responsive Fe_3O_4/poly(St-NIPAM) nanocomposites. This group reported another similar nanocomposite, where GMA was used as a copolymer instead of NIPAM.[176] Another study used PNIPAM in the fabrication of the Fe_3O_4/SiO_2/PNIPAM/EuW_{10} nanocomposite with core–shell luminescence.[177] R. Piñol, *et al.*[178] reported a single nanoheating and nanotemperature measuring platform made of iron oxide cores functionalized with Eu^{3+} and Tb^{3+} complexes and coated with a P4VP-*b*-P(PMEGA-*co*-PEGA) copolymer. Using a one-pot electrospinning approach, Y. Liu, *et al.*[179] created unique photoluminescent, electrical and magnetic trifunctional flexible $Eu(BA)_3$phen/PANI/Fe_3O_4/PVP hollow nanofibers.

Comparative analysis of the synthesis routes for Ln-IONPs: a comparison of major synthetic strategies is presented in Table 1, which highlights the clear trade-offs between structural control, multifunctional performance, and scalability. Thermal decomposition consistently yields highly crystalline, monodisperse nanoparticles (typically 10–30 nm) with high magnetic

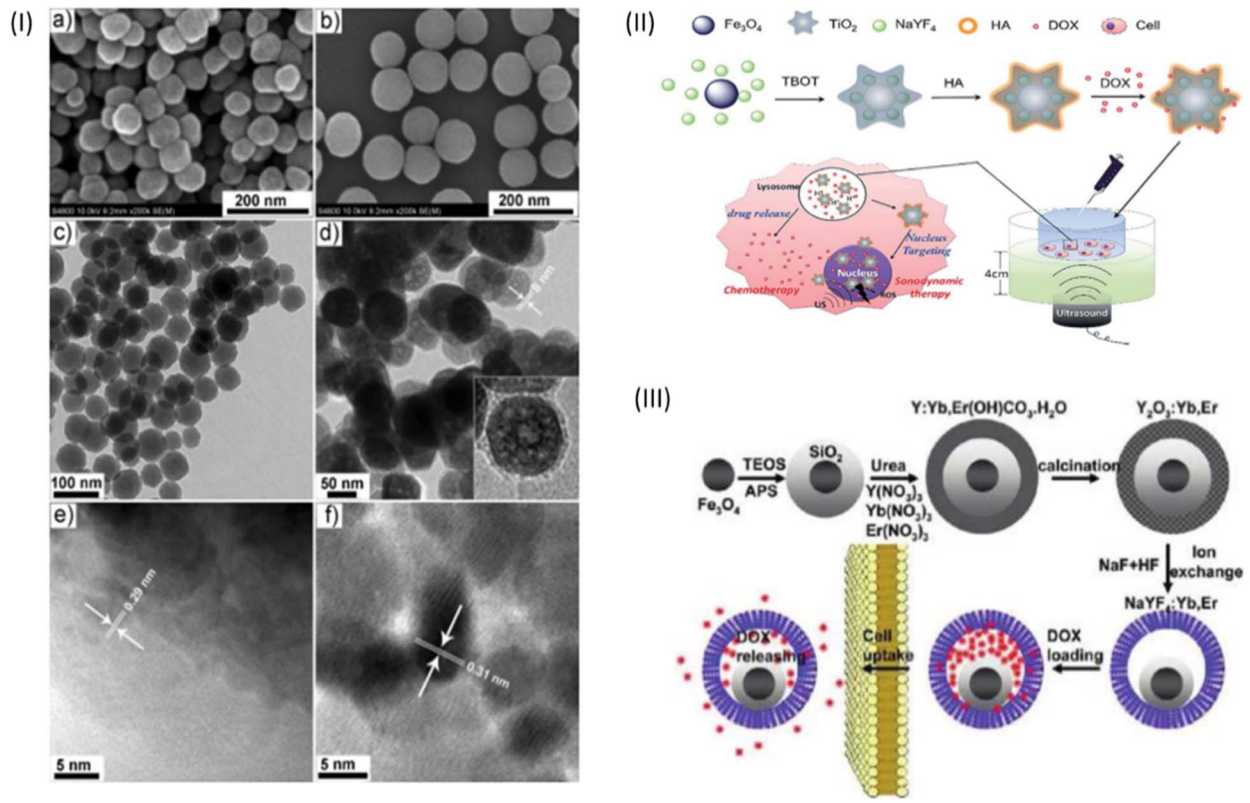

Fig. 17 (I) FE-SEM images of (a) pure Fe_3O_4 and (b) Fe_3O_4@*n*SiO_2@*m*SiO_2@$NaYF_4$:Yb^{3+}, Er^{3+} NPs. TEM images of (c) pure Fe_3O_4 and (d) Fe_3O_4@*n*SiO_2@*m*SiO_2@$NaYF_4$:Yb^{3+}, Er^{3+} NPs. HRTEM images of (e) pure Fe_3O_4 and (f) Fe_3O_4@*n*SiO_2@*m*SiO_2@$NaYF_4$:Yb^{3+}, Er^{3+} NPs. (II) Schematic illustrating the synthesis of HA-coated Fe_3O_4–$NaYF_4$@TiO_2 nanocomposites. (III) Synthetic procedure for the drug-loaded Fe_3O_4@-SiO_2@α-NaYF/Yb, Er nanorattles.

Table 1 Comparative overview of synthesis strategies for lanthanide-based iron oxide nanoparticles (Ln-IONPs), highlighting particle size dispersion, crystallinity, magnetic saturation, luminescence retention, surface functionalization efficiency, and scalability

Synthesis method	Representative Ln-IONPs (from cited studies)	Particle size (nm)	Size dispersion	Crystallinity	Magnetic saturation M_s (emu g^{-1})	Luminescence retention[a]	Surface functionalization efficiency	Scalability	Ref.
Co-precipitation	Fe_3O_4@Y_2O_3:Eu	~80	Moderate to narrow	Low-moderate	~3.4	Strong Eu^{3+} emission retained	High (PABA + biotin)	Moderate	150
	Fe_3O_4@YPO_4:Tb/Eu	~500–600	Moderate	Moderate	~1.7 (from the VSM curve)	Strong Tb^{3+}/Eu^{3+} emission retained	High (drug loading demonstrated)	Moderate	151
	Fe_3O_4/$BaMoO_4$:Dy^{3+}	~10.6	Moderate	Moderate	~14	Strong Dy^{3+} emission preserved	High (β-cyclodextrin *via* APTES)	Moderate	152
	Fe_3O_4@*m*-SiO_2@YPO_4:Tb^{3+}	~52	Moderate to narrow	Moderate	~23 (5-FU loaded nanocomposite)	Present, detectable Tb^{3+} emission	High (β-cyclodextrin + FA *via* GSH linker)	Moderate	153
	Fe_3O_4@SiO_2/GdOF:*x*Ce^{3+}, *y*Tb^{3+}	~30–50	Moderate	Moderate	~3.5	Strong green emission (Tb^{3+} transitions)	High (chitosan)	Moderate	154
	Fe_3O_4@LaF_3:Yb^{3+}, Er^{3+}	~190–220 (controllable)	Monodisperse	Crystalline	~36.7	Strong upconversion emission preserved	Typical ligand exchange or polysilane modification	Moderate	155
	YPO_4:Tb@Fe_3O_4	~10 (Fe_3O_4)	Monodisperse	Crystalline	~2.5	High retention with characteristic strong red emission	High (PAMAM dendrimer used as linker)	High	156
Thermal decomposition	Gd:Fe_3O_4 (Ln-doped)	~12.6	Moderate to narrow	High	~28.9	—	Low (ligand exchange required)	Moderate	159
	(EuIO) nanocubes	~10–20 (size tunable by reaction time)	Narrow	Mixed crystalline	~39.6	—	High (citrate coating for water dispersibility and biocompatibility)	Moderate to high	160
	Fe_3O_4/$NaYF_4$:Yb, Er heteroNPs	~100–200 (hetero-NP assemblies)	Moderate	Crystalline Fe_3O_4	~7.05–9.25	Strong upconversion luminescence (UCL)	Very high	Moderate	161
	$NaYF_4$:Yb^{3+}, Tm^{3+}@Fe_3O_4 nanocrystals	~25–30	Narrow to moderate	Crystalline	~12	Strong NIR-to-NIR UCL emission at ~800 nm	High	Moderate	162
Hydro(solvo) thermal	Fe_3O_4@SiO_2@Y_2O_3:Eu^{3+}	~262.36	Moderate	Moderate–high	~12.62	Strong (Eu^{3+} red emission)	High	Moderate	148
	Fe_3O_4/$NaYF_4$:Yb, Er	~240 (width) ~650 (length)	Moderate	High	~9.4	Bright green UCL	—	High	163

[a] Luminescence retention refers to the preservation of the lanthanide emission signals after integration into the nanoparticle system (important for imaging)."

Table 2 Performance comparison of representative Ln-IONPs synthesized *via* alternative synthetic procedures reported in Section 6.4.1, summarizing structural parameters, magnetic properties, optical retention, surface functionalization efficiency, and scalability

Synthesis method	Representative Ln-IONPs (from cited studies)	Particle size (nm)	Size dispersion	Crystallinity	Magnetic saturation Ms (emu g^{-1})	Luminescence retention[a]	Surface functionalization efficiency	Scalability	Ref.
Microwave-assisted synthesis	$Fe_3O_4/SiO_2/NaGdF_4$ doped with Ce, Eu	~19.1	Narrow	Pure crystalline core	~1.2	Strong down-conversion emission	High	Moderate	169
	$Fe_3O_4/SiO_2/NaGdF_4$ doped with Yb, Er	~16.2	Narrow	Pure crystalline core	~1.2	Up-conversion emission retained	High	Moderate	
Sol–gel process	Fe_3O_4–$NaYF_4$@TiO_2	~20–40	Narrow	Crystalline	~7.5	UCL NIR excitation retained	High	Moderate	170
	Fe_3O_4@*n*SiO_2@*m*SiO_2@$NaYF_4$: Yb^{3+}, Er^{3+}/Tm^{3+}	~80	Narrow	Crystalline core	~38.0	Strong up-conversion emission	High	High	149
Ion-exchange/ controlled etching method	Fe_3O_4@SiO_2@-$NaYF_4$/Yb, Er nanorattle	~115	Narrow	Crystalline core	~1.28	Strong upconversion luminescence	High	Moderate	172
Spray pyrolysis	Fe_3O_4/Eu:Gd_2O_3	~50–100	Broad	High	—	Intense red emission	High	Very high	173
Surface modification and decoration by polymer	$Fe_3O_4/SiO_2/NH_2$/PAA/LnF_3	~50–100	Narrow	Crystalline core	—	Bright lanthanide emission	High	Moderate	174

[a] Luminescence retention refers to the preservation of the lanthanide emission signals after integration into the nanoparticle system (important for imaging).

saturation values (M_S up to ~40 emu g^{-1}), reflecting excellent dopant homogeneity and crystal quality. However, these materials often require post-synthetic ligand exchange to improve surface functionalization efficiency, which can complicate biological translation. In contrast, coprecipitation and hydro(solvo) thermal methods offer better scalability and surface accessibility, enabling efficient functionalization with polymers, biomolecules, or silica shells, though often at the cost of broader size dispersion, moderate crystallinity, and reduced M_S values. Importantly, luminescence retention is strongly architecture-dependent rather than method-dependent: core–shell designs incorporating inert spacers (*e.g.*, SiO_2) or spatially separated Ln-doped phases consistently preserve lanthanide emission across all synthesis routes. Emerging approaches such as microwave-assisted, sol–gel, and ion-exchange methods provide a balanced compromise, delivering narrow size distributions, preserving upconversion or down-conversion luminescence, and improving surface functionalization while maintaining moderate magnetic performance. As summarized in Table 2, the alternative synthetic procedures reported in Section 6.2.4 primarily prioritize surface chemistry control and functional integration over maximal crystallinity or magnetic saturation. Seed-mediated and microemulsion-based strategies demonstrate superior luminescence retention through effective spatial separation, whereas post-synthetic adsorption and layer-by-layer approaches offer high functionalization efficiency at the expense of optical and magnetic performance. These tradeoffs highlight the application-driven nature of the method selection for Ln-IONPs, particularly in biomedical contexts. Overall, no single method is universally optimal; instead, synthesis routes must be selected based on the targeted balance between magnetic strength, optical efficiency, surface chemistry, and scalability.

7. Magnetic and optical properties of Ln-IONPs

7.1. Magnetic properties

Ln ions have a significant effect on the magnetic properties of IONPs. Li and colleagues investigated the effects of five different Ln ions (Gd, Sm, Nd, Y, and Lu) at identical concentrations on the magnetic properties of Fe_3O_4.[180] The saturation magnetization (M_S) values for these bimetallic particles were much less than the expected 96.4 emu g^{-1} for bulk magnetite. Comparatively, the saturation magnetization of magnetite samples doped with Gd^{3+} was the highest (45.9 emu g^{-1}) and the sample doped with Nd^{3+} exhibited the lowest saturation magnetization (26.8 emu g^{-1}). The magnetization curves also showed that the samples doped with Sm, Lu, and Gd were superparamagnetic and had zero coercivity, whereas the samples doped with Nd and Y had a minor hysteresis loop. Eu ions doped with magnetite also decreased the saturation magnetization.[160] The M_S value of EuIO nanocubes was 39.6 emu g^{-1} at 300 K, lower than that of magnetite nanoparticles of the same size (53.4 emu g^{-1}). The drop in magnetization observed in Ln-doped magnetite NPs could be attributed to two factors: a decrease in long-

range magnetic ordering due to spin canting and an increase in magnetic anisotropy.[159] The effect of dysprosium (Dy)-doping on the magnetic properties of magnetite was studied by Shao and colleagues.[181] They observed that increasing the Dy-doping concentration up to 7.5% (molar ratio of metal ions) led to a significant increase in the saturation magnetization from an initial 15 emu g^{-1} to 35 emu g^{-1}. When the doped-Dy content exceeded 7.5%, the saturation magnetization deteriorated. The contribution of a greater magnetic moment of Dy^{3+} is primarily responsible for the considerable increase in magnetization. The saturation magnetization (M_S) values of Fe_3O_4@SiO_2@Y_2O_3:Eu^{3+}, Fe_3O_4@Y_2O_3:Eu^{3+} and bare Fe_3O_4 NPs were determined to be 6.07, 12.62, and 69.27 emu g^{-1}, respectively.[148] Furthermore, the magnetic behavior of Fe_3O_4/SiO_2/$NaGdF_4$:Ce, Eu and Fe_3O_4/SiO_2/$NaGdF_4$:Yb, Er nanocrystals was studied by N. Shrivastava and colleagues,[169] which also exhibited a pronounced decrease in M_S. These considerable drops in M_S values can be attributed to several physical factors, including the presence of thick diamagnetic shells and organic coatings on the Fe_3O_4 cores, as well as the substantial non-magnetic contribution to the total weight of the sample. The M_S values of Fe_3O_4@Y_2O_3:Eu[150] and YPO_4:Tb^{3+}@Fe_3O_4 (ref. 156) nanocomposites were found to be 4.3 and 2.1 emu g^{-1}, respectively. The high non-magnetic contribution to the sample's weight is responsible for this result.

The effects of carboxymethylcellulose modification on the magnetic properties of magnetite were studied by L. Cheng and co-workers.[182] The bare Fe_3O_4 nanoparticles exhibited the highest magnetic response with a saturation magnetization of $M_S \approx$ 60.42 emu g^{-1}, reflecting the strong contribution of the iron oxide core. After silica coating, Fe_3O_4@SiO_2 showed a reduced $M_S \approx$ 28.88 emu g^{-1}, mainly due to the dilution effect of the non-magnetic SiO_2 shell. The fully structured CMC-functionalized Fe_3O_4@SiO_2@$GdPO_4$:Tb^{3+}, Ce^{3+} nanocomposite displayed

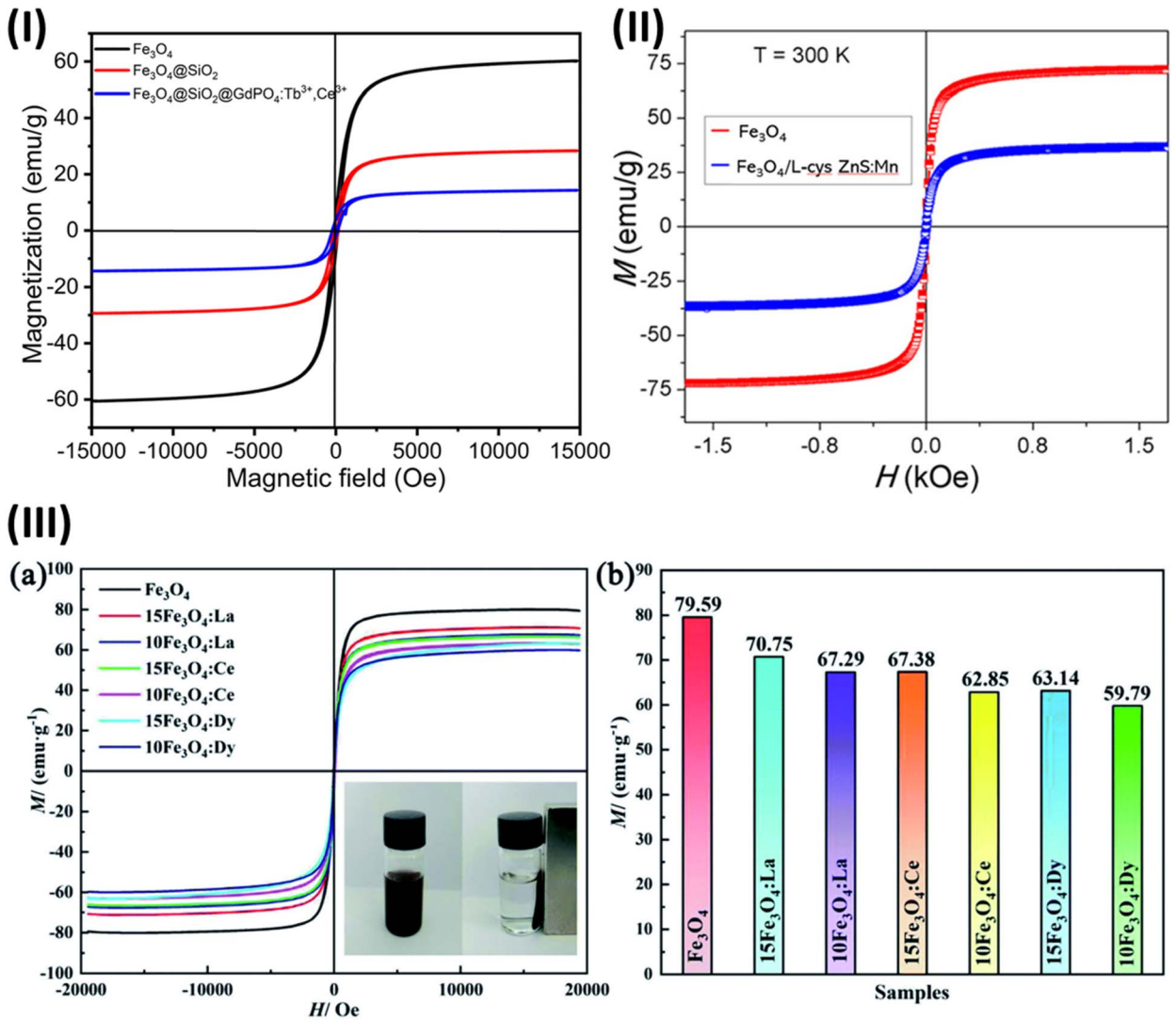

Fig. 18 (I) Room-temperature magnetization *vs.* magnetic field strength for the Fe_3O_4 nanoparticles, Fe_3O_4@SiO_2 nanocomposite and CMC-functionalized Fe_3O_4@SiO_2@$GdPO_4$:Tb^{3+}, Ce^{3+} nanocomposite. (II) M–H curves of Fe_3O_4 and Fe_3O_4/L-Cys ZnS:Mn. (III) (a) The magnetization curves of the nanoparticles at room temperature; the inset in (a) is a photograph of Fe_3O_4 before and after separation with a magnet; (b) the magnetization of the different nanomaterials.

a further decrease in magnetization ($M_S \approx 14.32$ emu g^{-1}) while retaining soft magnetic behavior with low coercivity, as shown in Fig. 18(I). Despite the lowered M_S, the composite demonstrated sufficient magnetic responsiveness to generate heat under an alternating magnetic field, achieving therapeutically relevant temperatures with appreciable specific absorption rate (SAR) values, thus supporting its application in magnetic fluid hyperthermia. The magnetic properties of the rare-earth-doped Fe_3O_4 nanoparticles were studied by Zeng and colleagues.[183] The pristine Fe_3O_4 nanoparticles showed the highest saturation magnetization, while rare-earth-doped samples Fe_3O_4:La^{3+}, Fe_3O_4:Ce^{3+}, and Fe_3O_4:Dy^{3+} exhibited progressively reduced M_S values with increasing dopant concentration, following the trend Fe_3O_4 > La-doped > Ce-doped > Dy-doped, as shown in Fig. 18(III). This decrease is attributed to the partial substitution of magnetic Fe^{2+} ions by Ln^{3+} ions and the consequent weakening of super-exchange interactions. Despite the lowered M_S, all doped nanoparticles retained room-temperature superparamagnetic behavior, ensuring minimal remanence and coercivity. Such tunable magnetic responses are advantageous for applications requiring controlled magnetic manipulation, including magnetic separation, sensing, and potential biomedical uses where moderate magnetization with good dispersibility is preferred.

In Fe_3O_4/L-Cys ZnS:Mn nanocomposites,[184] the Fe_3O_4 core retains room-temperature superparamagnetic behavior, characterized by negligible coercivity and remanence, confirming effective magnetic responsiveness, as shown in Fig. 18(II). The overall saturation magnetization (M_S) decreased after coupling with the non-magnetic ZnS:Mn shell due to magnetic dilution, while preserving magnetic separability. This maintained superparamagnetism enables magnetic manipulation and contributes to multifunctional applications, particularly magnetically controllable luminescent and theranostic systems. In a Gd-doped Fe_3O_4 nanoparticles study,[185] pure Fe_3O_4 nanoparticles exhibited the highest modelled saturation magnetization (M_S ~98 emu g^{-1} for large sizes at low temperature), while Gd-doped Fe_3O_4 showed progressively lower M_S (~85–70 emu g^{-1}) as the Gd concentration increased, due to antiferromagnetic interactions between Gd and Fe spins that weakened the net moment. This tuning of M_S through lanthanide doping retains ferrimagnetic ordering but moderates magnetic strength, and the ability to adjust the M_S and Curie temperature makes these particles promising for controlled magnetic applications such as magnetic sensing, hyperthermia heating, and magnetically guided systems.

7.2. Optical properties

Despite the promise of Ln ions in IONPs, the presence of IONPs adversely affects their luminescence properties. According to Yang and coworkers,[148] the luminous intensities of Fe_3O_4@SiO_2@Y_2O_3:Eu^{3+} composites are much lower than those of pure Y_2O_3:Eu^{3+} samples. The magnetic Fe_3O_4 causes the absorption

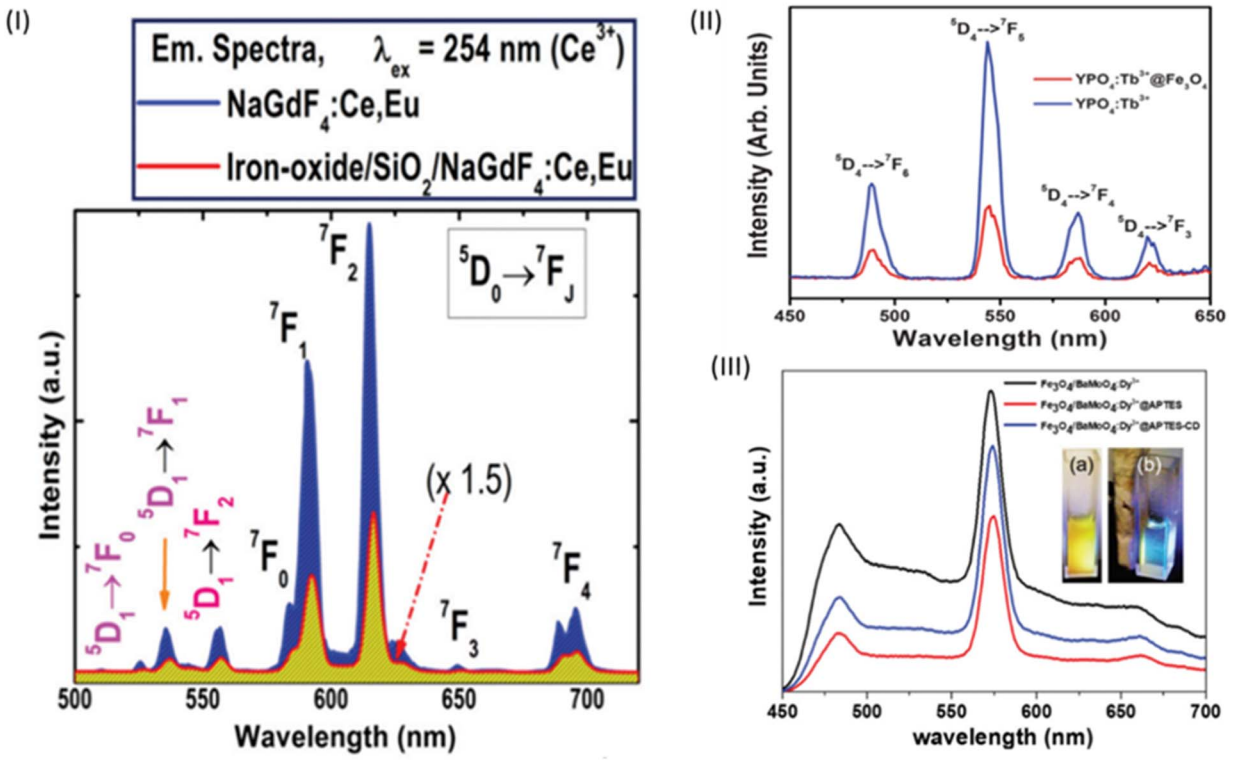

Fig. 19 (I) Emission spectra monitored at an excitation wavelength of 254 nm in the range of 500 nm to 790 nm for NaGdF4:Yb, Er and Fe_3O_4/SiO_2/NaGdF4:Yb, Er NPs. (II) Photoluminescence spectra of YPO_4:Tb^{3+} and YPO_4:Tb^{3+}@Fe_3O_4 when excited at 266 nm. (III) Emission spectra of MLHNPs, MLHNPs@APTES, and MLHNPs@APTES-CD excited at 260 nm. Insets show the photographs taken (a) under (260 nm) UV irradiation and (b) in the presence of a magnetic field.

of the UV energy of Y_2O_3:Eu^{3+}, resulting in a substantial quenching impact on the Y_2O_3:Eu^{3+} sample. Under infrared excitation (980 nm), the visible UC luminescence spectra of the $NaGdF_4$:Yb, Er and $Fe_3O_4/SiO_2/NaGdF_4$:Yb, Er were examined.[169] The intensity of the green emission band of $Fe_3O_4/SiO_2/NaGdF_4$:Yb, Er NPs was found to be approximately half that of the $NaGdF_4$:Yb, Er NPs, as shown in Fig. 19(I). The measured lifetimes of 8.20 and 6.50 ms for $NaGdF_4$:Ce, Eu and $Fe_3O_4/SiO_2/NaGdF_4$:Ce, Eu, respectively, indicate the occurrence of luminescence quenching induced by Fe_3O_4/SiO_2 phases. This quenching effect arises from the close proximity of the Fe_3O_4 or Fe_3O_4/SiO_2 components to the luminescent centers within the $NaGdF_4$ matrix, which facilitates non-radiative energy transfer. A similar reduction in the luminescence intensity of Tb^{3+} was observed in the hybrid YPO_4:Tb^{3+}@Fe_3O_4 material, attributed to the incorporation of the additional Fe_3O_4 component, as shown in Fig. 19(II).[156] When $BaMoO_4$:Dy^{3+} was combined with Fe_3O_4 NPs, a significant reduction in emission intensity was observed, as reported by Phaomei and coworkers.[152] Furthermore, after surface functionalization of the magnetic-luminescent hybrid nanoparticles ($Fe_3O_4/BaMoO_4$:Dy^{3+} MLHNPs) with β-cyclodextrin (CD) using 3-aminopropyltriethoxysilane (APTES) as a coupling agent, the luminescence intensity decreased even further, as shown in Fig. 19(III).

The optical properties of the Fe_3O_4@SiO_2@Y_2O_3:Eu^{3+} nanoparticles are characterized by a strong red luminescence,[147] primarily driven by the electronic transitions of the Eu^{3+} ions. The excitation spectra show a prominent charge transfer band (CTB) at 254 nm, while the emission spectra are dominated by a sharp peak at 610 nm, corresponding to the $^5D_0$ to $^7F_2$ transition. However, the overall luminescence intensity is significantly influenced by the nanoparticle's architecture; the Fe_3O_4 core acts as a quenching agent by absorbing both excitation energy and emitted light. While the SiO_2 interlayer serves as a protective barrier to mitigate this quenching, the intensity remains lower than that of pure phosphors. Furthermore, the material exhibits magneto-optical sensitivity, where the application of an external magnetic field induces a strong quenching effect, further reducing the luminescence intensity over time as magnetic domains align and facilitate non-radiative energy relaxation. The luminescence and magnetic properties of YVO_4:Ln^{3+}@Fe_3O_4(Ln^{3+} = Eu^{3+} or Dy^{3+}) nanocomposites were discussed by Deming and co-workers.[186] The nanoparticles exhibited a broad excitation band centered around 340 nm, attributed to the V–O charge transfer within the VO_4^{3-} groups. This indicates that the host lattice absorbs energy and effectively transfers it to the dopant rare-earth ions. For the europium-doped (Eu^{3+}) samples, the emission spectra are dominated by a sharp, intense red peak at 618 nm, corresponding to the $^5D_0$ to $^7F_2$ transition, which signifies that the Eu^{3+} ions occupy a site without inversion symmetry, as shown in Fig. 20(I). In contrast, the dysprosium-doped (Dy^{3+}) samples show two primary emission peaks at 484 nm (blue) and 574 nm (yellow). Notably, when these phosphor particles are coated with Fe_3O_4 (magnetic) nanoparticles, the luminescence intensity decreases, as shown in Fig. 20(II). This quenching effect is attributed to the absorption of excitation energy by the Fe_3O_4 layer and potential energy transfer from the phosphor host to the magnetic shell. The studies also identify optimal doping concentrations, typically around 5 mol% for Eu^{3+} and 1 mol% for Dy^{3+}, beyond which concentration quenching occurs, reducing the overall emission brightness. The optical properties of the Fe_3O_4/SiO_2-$GdPO_4$:Eu^{3+} hybrid nanoparticles are characterized by efficient red photoluminescence and biexponential decay behavior.[187] These materials exhibit an optimal excitation wavelength at 245 nm, which corresponds to a broad band associated with charge transfer between the O^{2-} and Eu^{3+} ions. Under UV radiation, the nanoparticles emit an intense red light with four characteristic Eu^{3+} emission peaks, primarily the $^5D_0$ to $^7F_2$ transition, indicating a high-symmetry environment for

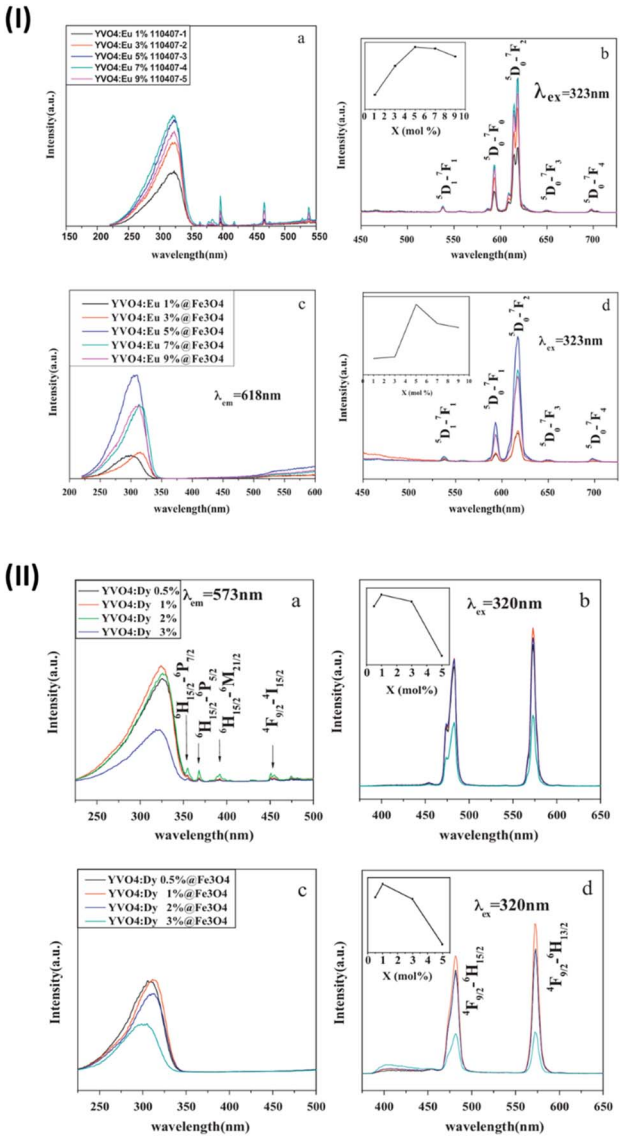

Fig. 20 (I) Excitation spectra of (a) YVO_4:Eu^{3+} and (c) YVO_4:-Eu^{3+}@Fe_3O_4. Emission spectra of (b) YVO_4:Eu^{3+} and (d) YVO_4:-Eu^{3+}@Fe_3O_4; insets of (b) and (d) are plots of emission intensity at 618 nm with various Eu^{3+} doping concentrations. (II) Excitation spectra of (a) YVO_4:Dy^{3+} and (c) YVO_4:Dy^{3+}@Fe_3O_4. Emission spectra of (b) YVO_4:Dy^{3+} and (d) YVO_4:Dy^{3+}@Fe_3O_4; insets of (b) and (d) are plots of emission intensity at 573 nm with various Dy^{3+} doping concentrations.

the Eu^{3+} ions. Specifically, the key optical characteristics include an intense broad excitation band at 245 nm (charge transfer) with less intense peaks at 270 nm and 394 nm arising from f–f transitions. Major emission peaks were observed at 589 nm ($^5D_0$ to $^7F_1$) and 612 nm ($^5D_0$ to $^7F_2$), along with lower energy transitions of $^5D_0$ to $^7F_3$ and $^5D_0$ to $^7F_4$. Increasing the Eu^{3+} concentration from 7.5% to 20% generally increases emission intensity, and higher concentrations eventually lead to concentration quenching *via* cross-relaxation. Furthermore, the emission decay follows a biexponential curve, suggesting that Eu^{3+} ions occupy two distinct environments: one inside the nanocrystal and one on the surface. These bifunctional particles maintain their red luminescence even when dispersed in water and can be manipulated by external magnetic fields.

The nanoparticles, specifically $Fe_3O_4/SiO_2/LaF_3:Ln^{3+}$ (where Ln is Tb or Eu) demonstrate narrow-band, high-intensity emission when incorporated into cellulose fibers.[188] Under UV light, they reveal vibrant multicolor luminescence, which is a result of the lanthanide dopants. For the terbium-doped (Tb^{3+}) particles, the emission spectrum shows four characteristic bands associated with transitions from the $^5D_4$ level to the ^7F_J ground state, with the most intense green emission occurring at 545 nm. In contrast, the europium-doped (Eu^{3+}) particles display a series of sharp red emission lines, primarily the $^5D_0$ to $^7F_2$ transition at approximately 611 nm. These emissions are facilitated by a broad excitation band in the UV region (around 248–251 nm), which triggers an efficient energy transfer (ET) from the host lattice to the lanthanide ions. Furthermore, the luminescence decay curves follow a bi-exponential function with long lifetimes in the millisecond range, confirming that the nanoparticles maintain high quantum efficiency even when embedded within the polymer matrix of the fibers. The nanoparticles (Fe_3O_4@SiO_2:phen:Eu^{3+}) described in the article[148] exhibit multifunctional properties by combining a superparamagnetic magnetite core with a luminescent europium-doped silica shell. Their optical properties are characterized by the signature red emission of Eu^{3+} ions, specifically the $^5D_0$ to ^7F_J ($J = 0$–4) transitions. The most intense peak observed is the hypersensitive $^5D_0$ to $^7F_2$ transition, indicating that the europium ions occupy sites of low symmetry without inversion centers, as shown in Fig. 21(I). To overcome the low absorption coefficients of lanthanide ions and the luminescence quenching typically caused by direct contact with iron oxide, the researchers utilized an "antenna effect" *via* 1,10-phenanthroline. This ligand absorbs near-UV radiation and efficiently transfers energy from its triplet state to the Eu^{3+} ions, while the silica shell acts as a physical barrier to preserve the emission intensity. Consistent with core–shell dynamics, the luminescence intensity decreases as the ratio of the magnetic core to the luminescent shell increases, as shown in Fig. 21(II).

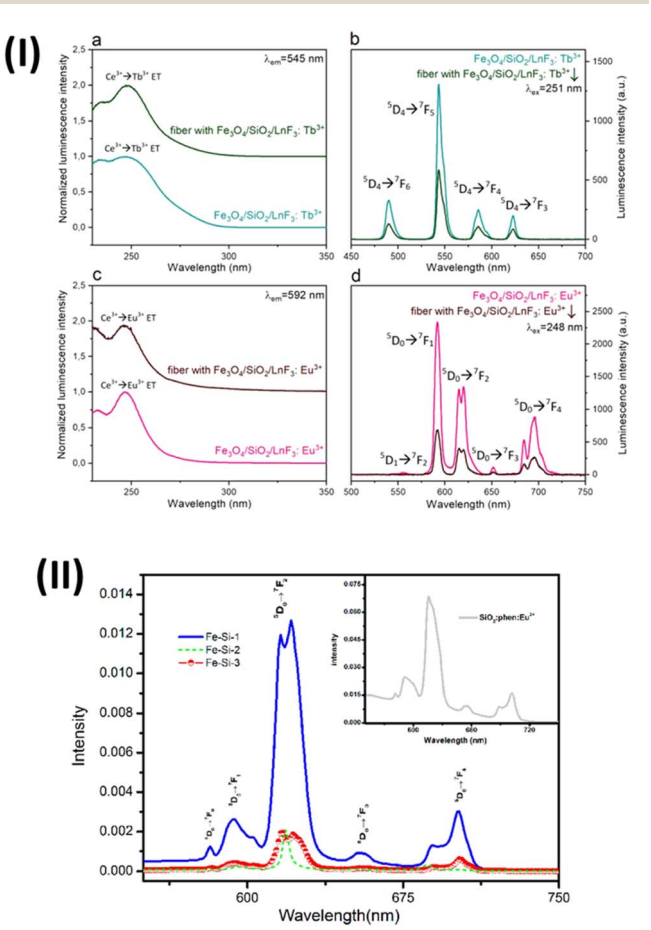

Fig. 21 (I) Excitation (a and c) and emission (b and d) spectra of the prepared materials: $Fe_3O_4/SiO_2/LnF_3:Tb^{3+}$ (a) and fibers modified with $Fe_3O_4/SiO_2/LnF_3:Tb^{3+}$ (b), $Fe_3O_4/SiO_2/LnF_3:Eu^{3+}$ (c) and fibers modified with $Fe_3O_4/SiO_2/LnF_3:Eu^{3+}$ (d). (II) PL spectra of Fe_3O_4@SiO_2:phen:Eu samples with different shell compositions and Eu concentrations, and SiO_2:phen:Eu^{3+} (inset).

8. Applications of Ln-IONPs

8.1. Bioimaging applications

Imaging techniques in the biomedical field have emerged as indispensable tools for detecting, diagnosing, screening, and monitoring the treatment of diseases such as cancer. The imaging methods include optical imaging, magnetic resonance imaging (MRI), X-ray computed tomography (CT scans), and radioisotope imaging. Molecular imaging techniques, such as MRI, CT, PET and optical imaging, each have their own set of benefits and drawbacks in terms of spatial resolution, penetration depth, and application areas. MRI has a high penetration depth and outstanding spatial resolution (many tens of micrometers), but it has poor sensitivity and limited planar resolution. Although a CT scan provides excellent anatomical information, it suffers from poor soft-tissue contrast, low planar resolution, and low sensitivity. PET imaging can provide a high-sensitivity (picomolar) visualization approach, but it is generally limited by low spatial/planar resolution. The only technology that can deliver cellular/molecular-level information (when the penetration depth is low) is optical imaging, which has the highest sensitivity (nearly single-molecule) and outstanding planar resolution. The integration of the advantages of two or more imaging modalities in one nanoparticle to generate multimodal bioimaging is widely desired to obtain more complementary and accurate information about the anatomical structure and physiological function for clinical diagnosis and

prognosis. The combination of Ln-based NPs with IONPs is a strong choice for application as a multimodal contrast agent and achieving multimodal bioimaging, such as in UCL/MRI, UCL/MRI/CT, UCL/MRI/PET, UCL/CT and MRI/CT. Some common multimodal bioimaging applications are discussed in the following sections.

Magnetic NPs possess interesting properties that allow them to be guided by an external magnetic field for targeted biodetection and bioimaging. Magnetic-assisted PL detection of DNA has been studied by using Fe_3O_4@$NaYF_4$:Yb/Er NPs.[189] The UCL intensity of Fe_3O_4@$NaYF_4$:Yb/Er NPs linked to target DNA demonstrated a nice linear dependency on target DNA concentration in the region of 7.8 to 78.0 nM. Likewise, Au-coated $NaYF_4$:Yb/Er@Fe_3O_4 multifunctional nanoparticles (MFNPs) were used as probes for the *in vivo* imaging and manipulation of mouse mesenchymal stem cells (mMSCs), employing magnetic-field-guided targeted optical imaging.[190] The MFNP-labeled mMSCs were injected intraperitoneally into the middle of the abdomen and guided to a wound near a magnet, where substantial UCL and T_2-weighted MR signals were recorded; no UCL or MR signals were detected at another site without a magnet. Hollow Fe_3O_4@$NaLuF_4$:Yb, Tm core–shell NPs, with a superparamagnetic Fe_3O_4 core, an r_2 relaxivity value of 21.63 s^{-1} mM^{-1} and a luminescent $NaLuF_4$:Yb, Tm shell, were employed for UCL/CT imaging, as shown in Fig. 22(II).[191] By encapsulating $NaYF_4$:Yb, Er NPs, Fe_3O_4 NPs, and squaraine dye into amphiphilic polymers, X. Zhu and colleagues[192] synthesized a new nanocomposite for a new triple-modal UCL/DCL/MRI imaging. Even when mice were injected with it, the nanocomposite displayed robust UCL, DCL and MRI (r_2 = 86 s^{-1} mM^{-1}) signals. The UCL and DCL signal levels in collected organs were consistent, demonstrating the nanocomposite's durability. Novel Fe_3O_4@YPO_4:RE (RE = Tb, Eu) hybrid spheres produced by Chen and colleagues[151] have successfully tagged human cervical cancer HeLa cells. After 96 hours of incubation with Fe_3O_4@YPO_4:Tb hybrid spheres, HeLa cells were imaged using fluorescence microscopy. Diffuse staining inside the cytoplasm revealed that Fe_3O_4@YPO_4:Tb hybrid spheres successfully labeled the HeLa cells. EuIO nanoparticles are also able to display both T_1 and T_2 MRI contrast effects.[160] Intravenous injection of EuIO nanoparticles into healthy Sprague Dawley rats at a dose of 2.0 mg [Fe + Eu] per kg of body weight resulted in significantly brighter T_1-weighted MR images of the heart after a minute of injection, as well as prominent T_2 contrast in the rat liver region. Because of the MR and UCL bimodal imaging and long-term lymph tagging *in vivo* capacity, $NaYF_4$:Yb^{3+}, Tm^{3+}@Fe_xO_y nanocrystals have been used in living cell imaging, as shown in Fig. 22(I),[193] and

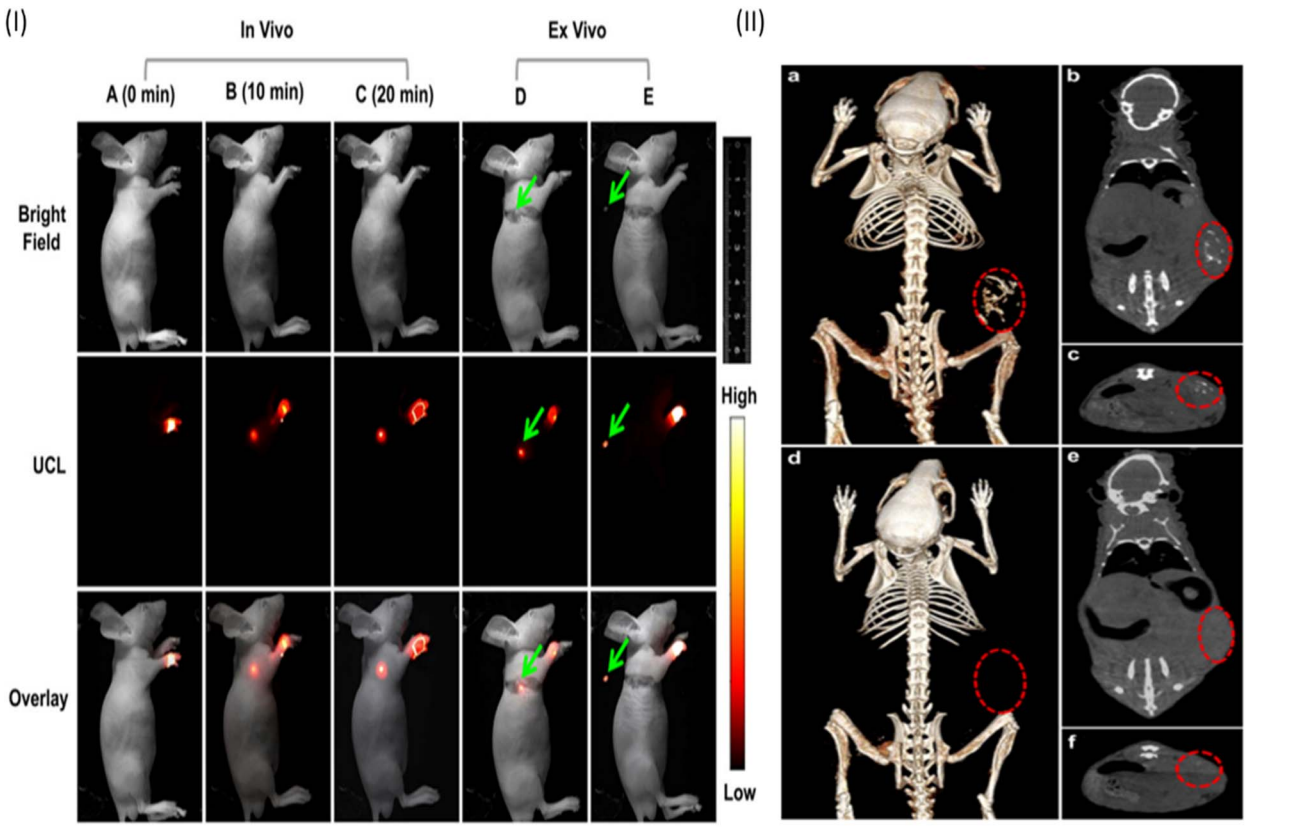

Fig. 22 (I) *In vivo* UCL imaging of the lymphatic system after the injection of $NaYF_4$:Yb^{3+}, Tm^{3+}@Fe_xO_y nanocrystals into a nude mouse at various times: (A) 0 min, (B) 10 min and (C) 20 min; (D and E) *ex vivo* images of the lymphatic system of a nude mouse sacrificed 40 minutes after injection. Green arrows mark the lymph nodes. (II) *In vivo* CT volume-rendered images (a and d); maximum intensity projection of the coronal (b and e) and transversal (c and f) images of the tumor-bearing mouse before (d–f) and 30 min after (a–c) intratumoral injection; the position of the tumor is marked by red circles.

Table 3 Representative lanthanide-based iron oxide nanoparticle (Ln-IONP) systems, targeted applications, and key reported performance metrics

Ln-IONP system	Structural design	Primary application(s)	Key reported performance metrics	Main limitation/performance gap	Ref.
Fe_3O_4@$NaYF_4$:Yb, Er	Core–shell	Optical imaging (UCL), MRI	Linear UCL detection of DNA (7.8–78 nM); magnetic guidance	Moderate MRI sensitivity	189
Au-coated $NaYF_4$:Yb, Er@Fe_3O_4	Core–shell–shell	*In vivo* UCL/MRI cell tracking	Strong T_2-weighted MR signal; magnetic field-guided localization	Complex synthesis	190
Hollow Fe_3O_4@$NaLuF_4$:Yb, Tm	Hollow core–shell	UCL/CT imaging	$r_2 = 21.63\ s^{-1}\ (mM)^{-1}$; strong UCL	Reduced magnetization due to hollow structure	191
Eu-doped iron oxide (EuIO) nanocubes	Ln-doped Fe_3O_4	Dual-mode MRI (T_1/T_2)	Enhanced T_1 heart contrast and T_2 liver contrast *in vivo*	No optical imaging modality	160
Fe_3O_4@YPO_4:RE (RE = Tb, Eu)	Core–shell	Fluorescence bioimaging + magnetic manipulation/ separation	Successful labeling of HeLa cells with clear intracellular fluorescence	Limited *in vivo* circulation and deep tissue penetration	151
$NaYF_4$:Yb,Tm@Fe_xO_y	Core–shell	UCL/MRI lymph imaging	$r_2 = 171.5\ s^{-1}\ (mM)^{-1}$ Long-term lymph node retention; bright UCL	Limited penetration depth	193
Fe_3O_4@SiO_2@α-$NaYF_4$:Yb, Er nanorattles	Core–shell–rattle	Drug delivery + imaging	96% tumor reduction (DOX, magnetic targeting); UCL retained	Reduced SAR due to inert shells	172
Fe_3O_4@m-SiO_2@YPO_4:Tb^{3+}	Core–shell	Drug delivery + fluorescence imaging	5-FU loading ≈ 91.6%; Tb^{3+} emission preserved	Moderate magnetic saturation	153
Fe_3O_4/$BaMoO_4$:Dy^{3+}	Hybrid	Drug delivery + imaging	Drug encapsulation efficiency ≈ 81%	Limited *in vivo* validation	152
$NaYF_4$:Yb,Er,Fe_3O_4@polymer	Polymer composite	Multimodal imaging (UCL/MRI) + magnetic targeted drug delivery	Efficient DOX loading and magnetic targeting	Reduced magnetic saturation; quantitative r_2 relaxivity not reported	194
MLHNPs@APTES-CD	Fe_3O_4 core with β-cyclodextrin coating	Adsorption and controlled release studies of methylene blue dye	Adsorption behavior analyzed by Langmuir and Freundlich isotherm models	Detailed quantitative metrics are not fully reported	195
$NaYF_4$:Yb,Er@Fe_3O_4@Au-PEG	Core–shell–shell	Photothermal therapy (PTT), MRI	Tumor temperature ≈ 50 °C; complete tumor ablation	Potential Au-related toxicity	196 and 182
Gd-doped Fe_3O_4 ($Gd_{0.02}Fe_{2.98}O_4$)	Ln-doped Fe_3O_4	Magnetic hyperthermia	SAR ≈ 36 W g^{-1} (52 kHz); reduced tumor growth	Moderate heating efficiency	197
Y^{3+}-doped Fe_3O_4 (0.1%)	Ln-doped Fe_3O_4	Magnetic hyperthermia	SAR = 194 ± 27 W g^{-1} (413 kHz)	Performance drops at higher doping	198
Fe_3O_4/Au/$Eu(TTA)_3$ NCs	Hybrid composite	Hyperthermia + fluorescence imaging	SAR up to 200 W g^{-1} (dual heating); λ_{em} ≈ 614 nm	Reduced heating with thick shells	199
CMC-functionalized Fe_3O_4@SiO_2@$GdPO_4$:Tb^{3+}, Ce^{3+} NCs	Core–shell and hybrid composite	Hyperthermia + imaging	SAR = 57 W g^{-1} (4.58 × 106 kA m^{-1} s^{-1})	Reduce heat generation efficiency and uncontrolled lanthanide release or toxicity	200

have demonstrated considerable promise for assisting in clinical lymph node investigation and diagnosis without the need for skin surgery.

Conclusively, the initial proof-of-concept studies were focused on the successful synthesis of stable colloids; recent studies have achieved *in vivo* relevance by reporting competitive performance metrics. For instance, the shift from *in vitro* labeling to deep-tissue *in vivo* imaging is substantiated by the high relaxivity values summarized in Table 3. The $NaYF_4$:Yb, Tm@Fe_xO_y core–shell system achieved a transverse relaxivity (r_2) of 171.5 mM^{-1} s^{-1} at 3.0*T*, significantly outperforming the commercial agent Feridex (108 mM^{-1} s^{-1}). This translates to a superior signal-to-noise ratio in lymphatic node mapping. Furthermore, for tri-modal probes (MRI/CT/UCL), the use of a lutetium-based shell ($NaLuF_4$:Yb, Tm) provided a specific r_2 value of 21.63 mM^{-1} s^{-1}, demonstrating that these platforms can effectively serve as negative contrast agents while maintaining high X-ray attenuation for CT imaging.

8.2. Drug delivery

Ln^{3+}-based IONPs have been extensively studied as a drug delivery vehicle in recent years. The luminescence of Ln ions is used to locate disease sites, while the magnetic properties of the IONPs are used to perform magnetic-field-guided drug delivery. It is believed that these dual modalities of nanoplatforms reduce side effects in non-infected areas, providing real-time therapy monitoring and magnetically controlled targeting. Various Ln-IONPs-tailored drug-delivery systems have been developed to achieve this purpose. For example, Fe_3O_4@SiO_2@α-$NaYF_4$:Yb/Er nanorattles (MUC-F-NR) have been developed and loaded with DOX for cancer treatment,[172] where the characteristic UC emissions of Er^{3+} reveal the active accumulation of DOX-loaded MUC-F-NR in the tumor. The use of an external magnetic field to target tumors resulted in a 96% reduction in tumor size by DOX-loaded MUC-F-NR (1.0 mg kg^{-1}) in mice.[172] DOX-loaded MUC-F-NR exhibited good *in vivo* treatment efficacy (96%) for liver cancer in murine hepatocarcinoma (H22) tumor-bearing mice in the presence of a magnetic field. It was also revealed that the luminescence emission intensity of the DOX-loaded carrier increased with cumulative DOX release, reaching its maximum when the release was complete. The organic groups in DOX, which produce high-energy vibrations to quench the UCL emissions, are to blame for the decreased luminescence. The link between emission intensity and drug release extent allows for the monitoring and tracking of the delivery process and therapeutic efficiency. Liu *et al.*[194] fabricated $NaYF_4$:Yb, Er, Fe_3O_4@polymer composite particles capable of delivering drugs to specific cells or tissues in a controlled manner. The $NaYF_4$:Yb, Er, Fe_3O_4@-polymer-DOX therapeutic system predominantly killed cells located near the magnet, whereas cells positioned farther away generally remained viable. β-Cyclodextrin- and folic acid-modified Fe_3O_4@*m*-SiO_2@YPO_4:Tb^{3+} nanocomposites have been loaded with the hydrophobic anticancer drug 5-fluorouracil (5-FU).[153] Its high drug loading capacity, combined with magnetic and luminescent properties, makes it a promising candidate for targeted drug delivery and cellular imaging. In comparison to the initial drug solution, the percentage of 5-FU adsorbed onto the fluorescent magnetic carrier is typically 91.6%, which equates to 114.5 mg of medication per unit mass of nanoparticles. Phaomei and colleagues[152] recently reported Fe_3O_4/$BaMoO_4$:Dy^{3+} magnetic luminous hybrid nanoparticles (MLHNPs) modified with β-CD and used as a carrier for substituted triazole derivative anticancer medicines. For MLHNPs@APTES-CD, the maximum adsorption density was 74.46 mg g^{-1}, and the drug encapsulation efficiency was 81.24%. In comparison to the other β-CD functionalized nanocarriers tested, the highest release was around 80%.[195,201–204]

Therefore, the translational significance of Ln-IONPs in drug delivery is moving beyond simple loading capacity to measurable therapeutic outcomes. While proof-of-concept studies report high drug encapsulation efficiencies (*e.g.*, about 81% for polymer-coated systems), *in vivo* relevance is best evidenced by tumor suppression rates. A notable example is the use of MUC-F-NR nanorattles, which achieved a 96% tumor reduction in mouse models, attributed to the synergistic effect of targeted chemotherapy and the large surface area (up to 114.5 mg g^{-1} loading for 5-FU). These metrics, highlighted in the quantitative summary in Table 3, provide a clear benchmark for assessing the potential of these carriers in clinical oncology compared to non-targeted delivery systems.

8.3. Therapeutic applications

The application of Ln-IONPs in imaging-guided photothermal therapy (PTT) has reached a significant milestone. To counteract the severe luminescence quenching induced by the iron oxide core, the integration of plasmonic materials such as gold (Au) or silver (Ag) nanostructures has emerged as a potent strategy. This enhancement is primarily driven by Surface Plasmon Resonance (SPR), where the collective oscillation of conduction electrons in the metal creates a concentrated local electromagnetic field. When the SPR frequency is tuned to match the excitation or emission transitions of the lanthanide ions, it can significantly enhance the absorption cross-section (increasing excitation efficiency) or the radiative decay rate (Purcell effect). However, the efficiency of this plasmonic boost is strictly governed by the spatial separation between the metal and the luminescent centers; precise architectural control using inert spacers is required to prevent deleterious energy transfer and maximize the Near-Field Enhancement (NFE).

For dual-mode imaging-guided PTT, PEG-modified $NaYF_4$:-Yb, Er@Fe_3O_4@Au nanocomposites have been employed.[196] The $NaYF_4$:Yb, Er core exhibited efficient UC emissions, whereas the Fe_3O_4 and Au shells were responsible for both T_2-weighted MRI and photothermal heating. For the targeted PTT of cancer cells, the photothermal effect of multifunctional nanoparticles (MFNP) was evaluated on KB cells incubated for 30 minutes with folic acid (FA)-conjugated PEG–MFNPs (0.05 mg mL^{-1}), followed by 808 nm laser irradiation (1 W cm^{-2}) for 5 minutes. Upon exposure to the 808 nm near-infrared (NIR) laser, the temperature of the MFNP solution rose from approximately 20 °C to 50 °C within 5 minutes. Following NIR laser irradiation, the

majority of KB cells treated with FA–PEG–MFNP were destroyed, whereas the untreated and PEG–MFNP-treated cells exhibited negligible or significantly lower levels of cell death.

In addition to molecular targeting, the magnetic characteristics of MFNP can also be used for magnetically targeted PTT. PEG–MFNP were incubated with HeLa cells at 37 °C for 2 hours under the influence of an external magnetic field. UCL imaging demonstrated a greater MFNP uptake in cells located near the magnet. Upon 808 nm NIR laser irradiation for 5 minutes, the cells close to the magnet were effectively destroyed, whereas those farther from the magnet remained largely unaffected. These findings clearly highlight the unique molecular/magnetic dual-targeted cancer PTT of MFNPs. The same nanocomposites were later used to produce magnetically targeted *in vivo* tumor PTT.[182] The surface temperature of tumors reached approximately 50 °C following the intravenous administration of the nanocomposites, whereas irradiated tumors without nanocomposites exhibited a lower temperature of about 38 °C. Tumors in mice injected with the nanocomposites and subjected to a tumor-targeted magnetic field were completely eradicated after NIR light irradiation. The coupling of $NaYF_4$:Yb, Er@Fe_3O_4@AuPEG NPs with FA molecules resulted in a unique molecular/magnetic dual targeting cancer PTT agent, which may provide more selective and targeted therapy.[196] The photothermal impact of multifunctional $NaYF_4$:Yb, Er@PE_3@-Fe_3O_4 nanocomposites has also been significantly increased.[144]

8.4. Magnetic hyperthermia

Magnetic hyperthermia (MH) leverages the capacity of magnetic nanoparticles (MNPs) to convert energy from an alternating magnetic field (AMF) into heat, raising the local temperature of the tumour tissue to ~42–46 °C and thereby inducing cancer cell death or sensitising tumours to adjunct therapies. The classical iron-oxide MNPs (Fe_3O_4/γ-Fe_2O_3) are widely employed due to their biocompatibility and well-established synthesis routes, yet to meet clinical-level performance, they must deliver a high specific absorption rate (SAR) under safe AMF conditions.

In recent years, the incorporation of lanthanide ions (for example, Gd^{3+}, Tb^{3+}, Eu^{3+}, Dy^{3+}) into iron-oxide hosts has emerged as a promising strategy to tailor magnetic anisotropy, saturation magnetization (M_S) and multifunctionality. For example, Philip Drake and coworkers[197] developed Gd-doped Fe_3O_4 ($Gd_{0.02}Fe_{2.98}O_4$) NPs for use in tumour therapy *via* magnetic fluid hyperthermia (MFH), which exhibited a SAR ~36 W g^{-1} of Fe at 52 kHz, about four times higher than

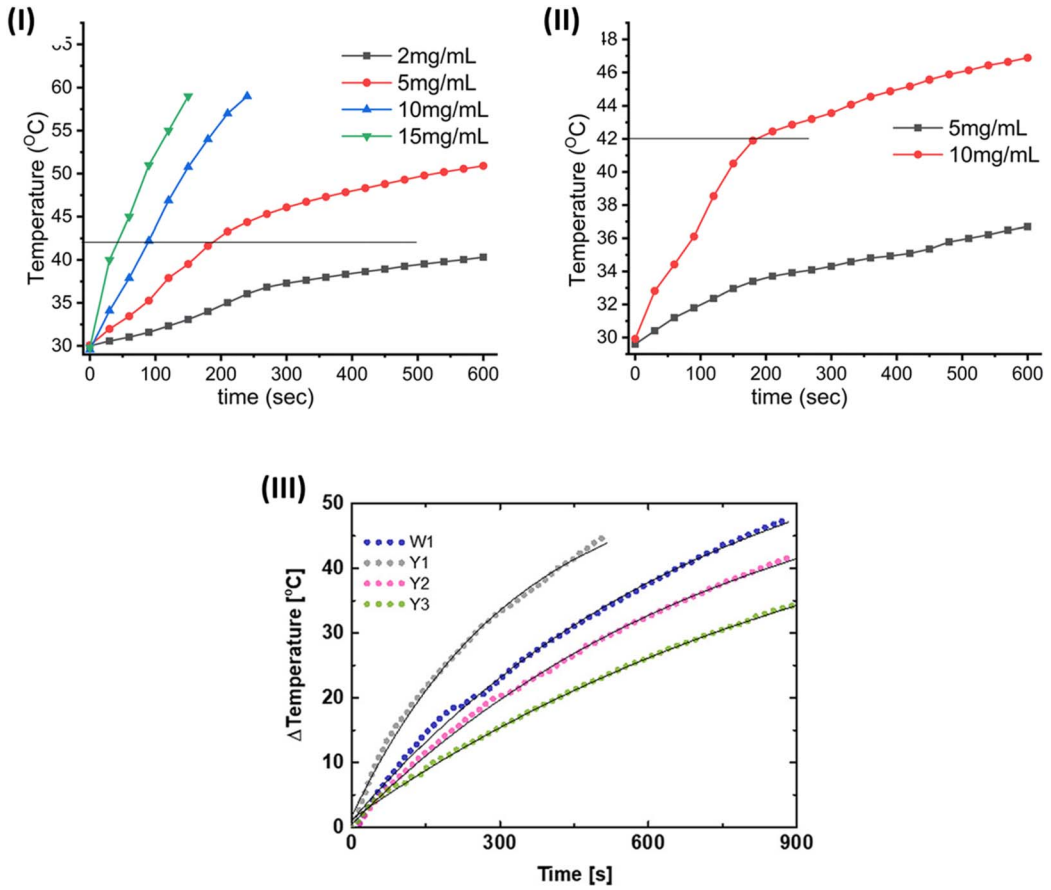

Fig. 23 Induction heating (temperature *vs.* time) profile of the (I) bare Fe_3O_4 nanoparticles and (II) Fe_3O_4@SiO_2@$GdPO_4$:Tb^{3+}, Ce^{3+} nanocomposites at different concentrations. Magnetic field strength (H_0) of 3.05 × 106 kA m^{-1} s^{-1} was maintained at a fixed applied frequency (f) of 178 kHz. (III) Measurement of the hyperthermic effect for Fe_3O_4 magnetic nanoparticles doped with different amounts of Y^{3+} ($W1$ = 0%, $Y1$ = 0.1%, $Y2$ = 1% and $Y3$ = 10%) ions at f = 413 kHz and a field amplitude H_0 of 16 kA m^{-1} s^{-1}.

undoped Fe_3O_4 in a mouse tumour model, with significantly slower tumour growth. In another report, Przemyslaw Kowalik and coworkers[198] designed Fe_3O_4 MNPs doped with different amounts of Y^{3+} (0.1%, 1%, and 10%) ions and measured the hyperthermic effect, as shown in Fig. 23(III). The best result was found for 0.1% Y^{3+}, which achieved SAR = 194 ± 27 W g^{-1} (at 16 kA m^{-1}, 413 kHz) and showed reduced viability of 4T1 cancer cells (viability of ~68% at 100 μg mL^{-1}) after MH treatment. Additionally, a multifunctional Eu(III) complex, doped with an Fe_3O_4/Au nanocomposite, *i.e.*, Fe_3O_4/Au/Eu(TTA)$_3$ NCs (60–70 nm), was synthesized by Hoang Thi Khuyen and coworkers.[199] The SAR values of 118.8, 136.5 and 200.3 W g^{-1} were achieved by magnetic, photothermal and dual heating modes, respectively, while enabling fluorescence imaging (λ_{max} = 614 nm) of HT29 colorectal cells. Synthetic advances include controlled doping *via* co-precipitation, core–shell and hybrid composite architectures (*e.g.*, CMC-functionalized Fe_3O_4@SiO_2@$GdPO_4$:Tb^{3+}, Ce^{3+} NCs), which allow simultaneous imaging and hyperthermia functionality.[200] However, bare Fe_3O_4 NPs exhibited a significantly higher SAR value (76 W g^{-1}) than the CMC-functionalized NCs (57 W g^{-1}) at the field strength of 4.58 × 10^6 kA m^{-1} s^{-1} for the same amount of sample (5 mg mL^{-1}), owing to the non-magnetic SiO_2 shell and inactive $GdPO_4$/CMC components that reduce the heat generation efficiency, as shown in Fig. 23(I and II). Despite these encouraging advances, translation remains challenging because intracellular confinement, protein corona formation and inter-particle dipolar interactions often reduce effective heating in tumour tissues *vs.* aqueous systems. Moreover, lanthanide release or toxicity must be controlled *via* robust chelation/coating.

The recent studies on Ln-doped iron oxides have shown that the doping level is a critical performance metric; for example, 0.1% Y^{3+}-doped Fe_3O_4 exhibited an exceptional SAR of 194 W g^{-1} at 413 kHz. In contrast, Gd-doping ($Gd_{0.02}Fe_{2.98}O_4$) reached a SAR of 36 W g^{-1} at 52 kHz, which, despite being lower, represented a four-fold increase over undoped magnetite at the same frequency. These quantitative gains in heating efficiency are essential for achieving the localized tumor temperature rise of 50 °C required for complete tumor ablation *in vivo*, as demonstrated in core–shell–shell $NaYF_4$:Yb, Er@Fe_3O_4@Au-PEG models. As summarized in Table 3, the variation in SAR values across different lanthanide dopants highlights the necessity of precise stoichiometry for therapeutic optimization.

Understanding the role of lanthanide-induced magnetic anisotropy is key to interpreting SAR enhancement and guiding future hyperthermia-oriented design. The enhancement of the specific absorption rate (SAR) observed in lanthanide-doped iron oxide nanoparticles can be fundamentally attributed to doping-induced modifications in magnetic anisotropy. The incorporation of lanthanide ions such as Gd^{3+} or Tb^{3+} into the iron oxide lattice perturbs the local crystal field and exchange interactions due to their large ionic radii and strong 4f spin–orbit coupling. Unlike Fe^{2+}/Fe^{3+} ions, lanthanide ions exhibit pronounced single-ion anisotropy, which contributes to an increase in the effective magnetocrystalline anisotropy constant (K_{eff}) of the nanoparticles. An increase in K_{eff} directly influences magnetic relaxation dynamics by shifting the Néel relaxation time toward the frequency range of the applied alternating magnetic field. This improved matching between relaxation time and field frequency enhances hysteresis losses and energy dissipation per cycle, leading to higher heat generation efficiency. Lanthanide doping can also induce controlled spin canting and surface disorder, further contributing to anisotropy enhancement without significantly compromising superparamagnetic behavior. Notably, Gd^{3+} doping often provides a balance between increased anisotropy and preserved magnetization due to its half-filled $4f^7$ configuration, whereas Tb^{3+}, with stronger spin–orbit coupling, can induce larger anisotropy but may reduce saturation magnetization at higher doping levels. These observations highlight the importance of optimizing lanthanide species and doping concentration to maximize SAR while maintaining biocompatible magnetic performance.

9. Biosafety evaluations of Ln-IONPs

Toxicity testing is required for the nanoparticles that are to be used in biomedical applications. The main assessing techniques are introduced in the following portion of this review, and the biosafety of various multifunctional Ln-IONPs will be explored based on their evaluation results. Across reported studies, biosafety outcomes are strongly influenced by nanoparticle composition, surface coating, and structural configuration, rather than by the presence of lanthanide ions alone.

9.1. Cell viability

Studies on the *in vitro* viability of cells with targeted NPs are considered the most practical way for evaluating the cytotoxicity of Ln^{3+}-based nanoparticles. CCK-8, MTT, XTT, and MTS are among the test kits that have been developed for this purpose. The most often used is 3-(4,5-dimethylthiazol-2-yl)-2,5-diphenyltetrazolium bromide (MTT). A comparative analysis of these assays across different Ln-IONP systems revealed consistent design-dependent trends in cytotoxicity, particularly with respect to lanthanide confinement and surface passivation. The following are the results of cell viability tests performed on different samples.

In a cell viability test, lanthanide-doped iron oxide–fluoride hybrid nanocrystals, $NaYF_4$:Yb^{3+}, Tm^{3+}@Fe_xO_y were found to exhibit moderate, concentration-dependent toxicity.[162] When incubated with KB cells for 24 and 48 hours, the half maximum inhibitory concentrations (IC_{50}) of these nanocrystals were 295 and 190 g mL^{-1}, respectively, indicating that they are relatively safe. Similar behavior has been reported for directly doped or weakly shielded Ln-Fe_3O_4 systems, where partial reductions in viability at higher doses were attributed to enhanced cellular uptake or possible Ln^{3+} ion leakage.[148,151,158,163] Nevertheless, within concentration ranges relevant for imaging or diagnostic applications, these materials generally remained cytocompatible. The toxicity of DOX-loaded and DOX-free core–shell Fe_3O_4@SiO_2@-$NaYF_4$/Yb, Er nanorattles (MUC-F-NR) on the viability of human hepatoma cell (QGY-7703) revealed that DOX-free MUC-F-NR had no adverse effect on the cells; however, DOX-loaded MUC-F-NRs demonstrated considerable

cytotoxicity even at low concentrations (0.2 to 4 μg mL^{-1}).[172] The continuous release of drug molecules from the MUC-F-NR is responsible for increased cytotoxicity. Comparable trends have been observed for other drug-loaded Ln-IONP platforms, where reduced cell viability primarily reflects controlled drug release rather than intrinsic nanoparticle toxicity.[172,190,195,205]

Almost all of the cells in the γ-Fe_2O_3 and Tb-γ-Fe_2O_3 groups were alive, showing that the nanocrystals were non-toxic.[206] Normal embryonic kidney 293 cells were used to test the cytotoxicity of Dy-doped and undoped IONPs.[181] Both cells treated with Dy-doped γ-IONPs and cells treated with pure undoped γ-IONPs showed high normalized relative viability. Even at a high dose of 200 mg mL^{-1}, over 88.6% of the normal embryonic kidney 293 cells survived, demonstrating that the Dy-doped γ-IONPs have little cytotoxicity. Similar findings have been reported for lanthanide-associated iron oxide nanostructures with robust crystal lattices, where cytotoxic effects remained minimal in the absence of surface ligand-induced stress.[155,161] Gd-doped magnetite (Gd:Fe_3O_4) nanoparticles were assessed by F. J. Douglas, *et al.*[159] For doses below 0.1 mg mL^{-1}, the MTT assay revealed that cell metabolic activity (viability) persisted in the 70–80% range for Gd:Fe_3O_4 particles and in the 90–100 percent range for undoped Fe_3O_4 particles. The reasons for the modest loss in cell viability in the Gd-doped samples are unknown; likely, the 'leakage' of free Gd^{3+} from the doped particles caused the cell viability to suffer. This observation is in alignment with other reports on Ln-doped iron oxide systems, where incomplete lanthanide confinement led to narrower cytocompatible windows.[148,151,158,163]

With the help of their sample toxicity evaluation, cells incubated with YPO_4:Tb^{3+}@Fe_3O_4 NPs were viable up to a concentration of 1 mg mL^{-1}, but the cell viability dropped dramatically when they were incubated with YPO_4:Tb^{3+}-PAMAM without Fe_3O_4, and cell death occurred even at a lower concentration of 0.1 mg mL^{-1}, indicating that Fe_3O_4 NPs play an important role in biocompatibility.[156] The control cell viability was 99% without treatment, but induced magnetic hyperthermia significantly reduced the cell viability, as shown in Fig. 24(I). It should be emphasized, however, that the dendrimer PAMAM is non-toxic up to a concentration of 1 mg mL^{-1}. MTT assay results indicated that at the maximum metal ion concentration (120 g [Fe + Eu] per mL), the sodium citrate-coated EuIO nanocubes showed little cytotoxicity when incubated with SMMC-7721 cells or MRC-5 cells, demonstrating good biocompatibility.[160] Additional studies on polymer-coated and citrate-stabilized Ln-IONPs, including Eu-doped iron oxide nanocubes and polymer-encapsulated upconversion iron oxide systems, further confirmed minimal cytotoxicity at relatively high nanoparticle concentrations.[160,161,182,196] In these systems, cell viability was largely preserved unless therapeutic agents were incorporated, reinforcing the importance of surface chemistry in governing nano–bio interactions.

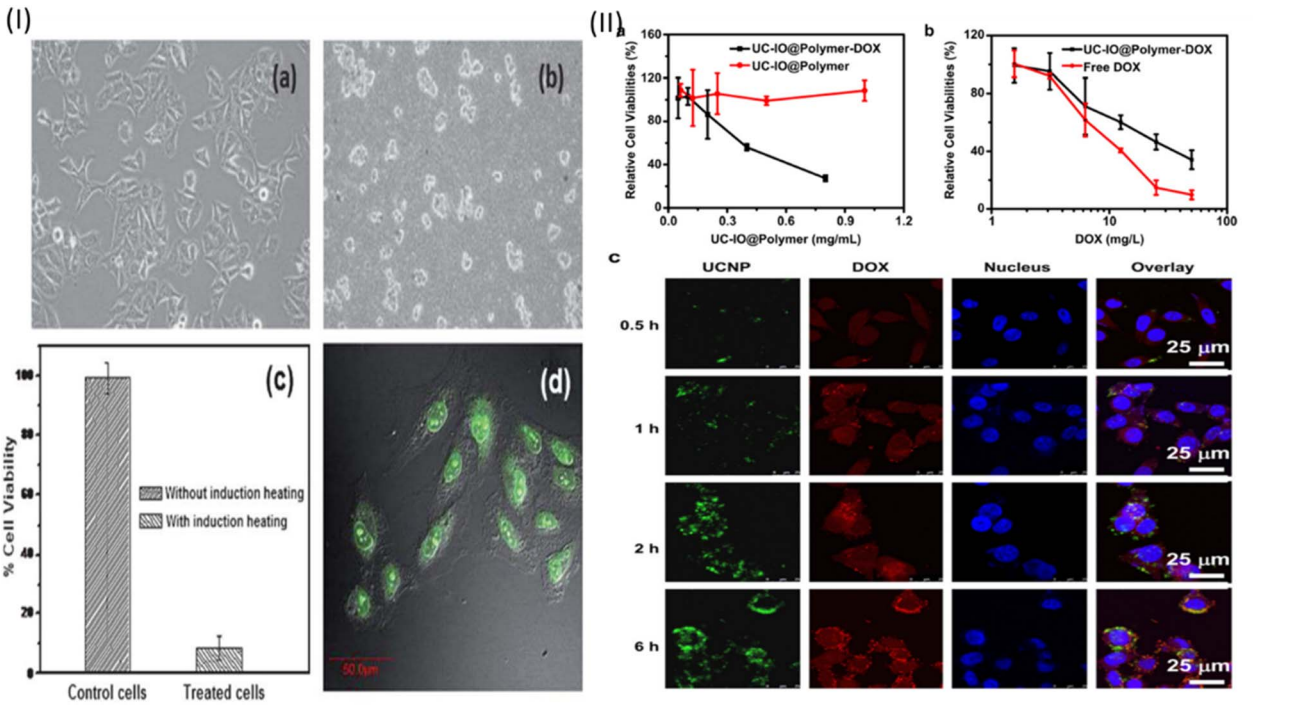

Fig. 24 (I) Optical images of (a) control HeLa cells, (b) HeLa cells treated with YPO_4:Tb^{3+}@Fe_3O_4 nanohybrids followed by AC induction heating; magnification 10×. (c) Percentage cell viability profile of the control and treated HeLa cells with and without induction heating. (d) Confocal microscopy images of HeLa cells treated with the nanohybrids. (II) *In vitro* cell experiments of the UC-IO@Polymer-DOX nanocomposite. (a) Relative viabilities of HeLa cells 24 h after being incubated with UC-IO@Polymer and UC-IO@PolymerDOX. (b) Relative viabilities of HeLa cells 24 h after being incubated with DOX and UC-IO@Polymer-DOX. (c) Confocal images of HeLa cells incubated with UC-IO@Polymer-DOX for 0.5, 1, 2, and 6 h. UCL emissions from UCNPs (green) and DOX fluorescence (red) were recorded under the excitation of 980-nm and 488-nm lasers, respectively.

In contrast, core–shell and heterostructured architectures, such as YPO_4:Tb^{3+}@Fe_3O_4, Fe_3O_4@SiO_2@Ln-based phosphors, and Fe_3O_4/$NaYF_4$:RE^{3+} hybrids, consistently demonstrated high cell viability across multiple cell lines and incubation periods.[148,151,154,168,169] These findings underscore the protective role of physical separation between the lanthanide-containing phase and the biological environment. Even for smaller particle sizes, cytotoxic responses remained limited when surface passivation was maintained.[189,190] The cell viability of Fe_3O_4@*m*SiO_2@YPO_4:Tb@CD–GSH@FA nanocomposites, assessed using an MTT assay, revealed that the nanocarrier had no cytotoxicity against both L929 and HeLa cells.[153] Fe_3O_4@*m*SiO_2@YPO_4:Tb@CD–GSH@FA nanoparticles are biocompatible up to a large dose of 200 g and for a lengthy incubation period (72 h), indicating their promising application potential.

The viability of mouse 4T1 breast cancer cells was about 97.7% when the concentration of Fe_3O_4 in $NaYF_4$:Yb, Er@PE_3@Fe_3O_4 solution was 0.01 mg mL^{-1}.[144] The viability of cancer cells was steadily reduced with an increase in the concentration of the nanocomposites. However, at a 100-fold higher concentration, *i.e.*, at 1 mg mL^{-1} of Fe_3O_4, the cancer cell viability remained at 91.9%, indicating that Fe_3O_4 in $NaYF_4$:Yb, Er@PE_3@Fe_3O_4 nanocomposites has a low cellular toxicity. Polymer-encapsulated UC iron oxide (UC-IO@Polymer) nanocomposites produced by Xu and colleagues[194] were immobilized with DOX. The MTT cell viability results showed that UC-IO@Polymer was non-toxic, but UC-IO@Polymer-DOX was clearly harmful; this was most likely due to the delayed release of DOX from the UC-IO@Polymer-DOX nanocomposites. Confocal pictures of cells incubated with UC-IO@Polymer-DOX for various periods indicated the time-dependent uptake of nanocomposites, from which DOX was gradually released for cell nucleus entry, as shown in Fig. 24(II). Overall, the accumulated cell viability data suggest that Ln-IONPs that employ hydrophilic coatings, silica or polymer shells, and heterostructured designs define a relatively broad cytocompatible regime, whereas directly doped or poorly shielded systems exhibit increased sensitivity to dose and particle size.

9.2. Hemolysis

Hemolysis is the disruption of red blood cell (erythrocyte) membranes, which causes the release of hemoglobin. The nanoparticles that produce considerable hemolysis are not suitable for biomedical applications because they can cause anemia.[207] The surface functionality of nanoparticles, such as hydrophobicity, hydrophilicity, and surface charge, generally influences the hemolytic behavior of that particular entity.[208] Accordingly, hemolysis assays provide a critical measure of blood compatibility for Ln-IONPs intended for systemic administration.

L. S. da Costa and colleagues investigated the effects of functionalized IONCs@SiO_2TTA-Eu and IONCs@SiO_2TTAEu-DBM nanomaterials bearing positive and negative surface charges, respectively.[209] Hemolysis was not observed for the IONCs@SiO_2TTA-Eu nanocomposite, but it was observed in the presence of the dibenzoylmethane (DBM) ligand, resulting in the disintegration of around 80% of the red blood cells (RBCs). This phenomenon is related to the surface charges of the materials, which created differences in nano-biointeractions and changed the interaction with RBCs. The absence of hemolytic impact was observed for IONCs@SiO_2TTA-Eu because the surface charge of the IONCs@SiO_2TTA-Eu and the charges on the membrane surface of RBCs are both positive. When compared to IONCs@SiO_2 and IONCs@SiO_2TTAEu-DBM NPs, experimental results revealed that the IONCs@SiO_2TTA-Eu has good biocompatibility, exhibiting non-toxic effects against red blood cells (hemolysis), implying that the ligand DBM is directly associated with the toxic impact. Similar observations have been reported for other cationic or ligand-exposed Ln-IONPs, where strong electrostatic interactions with erythrocyte membranes resulted in pronounced hemolysis.[151,158,189,190] By contrast, silica-coated and polymer-passivated Ln-IONPs, including Fe_3O_4@SiO_2@Ln hybrids and polymer-coated magnetic–luminescent nanocomposites, consistently exhibited negligible hemolytic activity across wide concentration ranges. These results indicate that hemotoxic effects are primarily governed by surface chemistry rather than by the magnetic or lanthanide components themselves.

The zebrafish (*Danio rerio*) has been used as a promising biological model for *in vivo* nanotoxicity, nanomedicine, and nanosafety research.[210,211] Their mortality, deformity, edema, hatching rate, overall length, and yolk sac size were measured. The benefits of using this model include the ability to evaluate multiple parameters at once, such as embryonic development, genotoxicity, oxidative stress, and so on, allowing the assessment of potential environmental risks in aquatic systems, and also in human health, due to its genetic similarity to humans.[212,213] L. U. Khan, *et al.*[154] used zebrafish embryos to perform a thorough physicochemical characterization and *in vivo* toxicity evaluation of the multifunctional Fe_3O_4@SiO_2/GdOF:*x*Ce^{3+}, *y*Tb^{3+} nanoplatform. In a classic fish embryo toxicity (FET) assay, no mortality was seen in the control groups, and no significant differences in total length or yolk sac size were observed among any treatment groups. Though the hatching rate differed among the groups at 48 hours after fertilization (hpf), all embryos hatched by 72 hpf, indicating that there was no major risk. Furthermore, zebrafish larvae exposed to a concentration of 100 mg L^{-1} during incubation showed deformity (5.53%) and edema (19.44%). There were no significant differences in mortality, overall length, yolk sac size, or edema in embryo toxicity tests with and without chorion. However, when compared to a typical FET, the production of edema with and without chorion, as well as the deformity of embryos with chorion, was dramatically reduced.

The most often used mammalian models for *in vivo* toxicological assessments are murine models, which include mice and rats. Physical and behavioral indications, histological examination, hematological and blood biochemistry analysis, and immunotoxicity are all common toxicity evaluation criteria in mouse models. A. Xia, *et al.*[162] used the histological examination of lymphatic node sections to assess the *in vivo* toxicity of $NaYF_4$:Yb^{3+}, Tm^{3+}@Fe_xO_y nanocrystals. The treated mice did not display any clear toxicological reactions, such as weight loss,

Table 4 Qualitative synthesis of biosafety data for Ln-IONPs: influences of composition, architecture, and coating on cell viability and hemocompatibility

NP type/architecture	Surface/coating	Observed viability/hemolysis	Possible reason(s)	Notes	Ref.
Hybrid ($NaYF_4$:Yb^{3+}, Tm^{3+}@Fe_xO_y)	Iron oxide-fluoride	Viability: moderate; IC_{50} ~190–295 μg mL^{-1}	Concentration-dependent toxicity	Safe for bioimaging; no *in vivo* toxic reaction in mice	162
Nanorattle (Fe_3O_4@SiO_2@$NaYF_4$/Yb, Er)	Silica (SiO_2)	Viability: no adverse effects for DOX-free	Continuous drug (DOX) release causes high toxicity in loaded versions	Architecture allows controlled drug release	172
Doped IONP (Gd:Fe_3O_4)	Doped *vs.* undoped	Viability: 70–80% (doped) *vs.* 90–100% (undoped) at <0.1 mg mL^{-1}	Potential "leakage" of free Gd^{3+} from the doped particles	Incomplete confinement leads to narrower cytocompatibility windows	159
Doped IONP (Dy:Fe_2O_3)	Robust crystal lattice	Viability: >88.6% even at 200 mg mL^{-1}	Robust crystal lattice prevents ion leakage	Minimal cytotoxicity in the absence of surface ligand-induced stress	181
Core–shell (YPO_4:Tb^{3+}@Fe_3O_4)	Fe_3O_4 shell/PAMAM	Viability: high (viable up to 1 mg mL^{-1})	Physical separation/confinement by Fe_3O_4 shell	Removal of the Fe_3O_4 shell leads to cell death at 0.1 mg mL^{-1}	156
Nanocube (EuIO)	Sodium citrate	Viability: high (biocompatible up to 120 μg mL^{-1})	Citrate stabilization provides good biocompatibility	Minimal cytotoxicity confirmed in multiple cell lines	160
Multilayer hybrid (Fe_3O_4@*m*SiO_2@YPO_4:Tb)	Silica/GSH/FA	Viability: no cytotoxicity against L929/HeLa up to 200 μg	Multilayer shell provides robust protection	Long incubation (72 h) confirms application potential	153
Polymer hybrid ($NaYF_4$:Yb, Er@PE_3@Fe_3O_4)	Polymer (PE_3)	Viability: 91.9% at 1 mg mL^{-1} concentration	Surface passivation limits cellular toxicity	Polymer encapsulation ensures safety at high doses	144
Functionalized IONC (IONCs@SiO_2TTA-Eu)	Silica/positive charge	Hemolysis: not observed (0%)	Positive surface charge matches the RBC membrane surface	Good blood compatibility for systemic administration	208
Functionalized IONC (IONCs@SiO_2TTA-Eu-DBM)	DBM ligand/negative charge	Hemolysis: ~80% RBC disintegration	Negative charge/DBM ligand triggers toxic nano-bio interaction	Hemotoxicity is primarily governed by surface chemistry	208

aberrant behavior, or a change in reproductive capacity, after being injected with the nanocrystals in their right forepaws for one month or more. The results of the toxicity tests suggest that $NaYF_4$:Yb^{3+}, Tm^{3+}@Fe_xO_y nanocrystals can be safely used as a bioimaging agent.

Taken together, the reported cell viability and hemolysis studies indicate that the biomedical relevance of Ln-IONPs is intrinsically design-conditional, with safer biological profiles emerging for heterostructured and surface-passivated systems, while insufficient lanthanide confinement, high surface charge, or ultrasmall dimensions substantially narrow the cytocompatibility and hemocompatibility windows. To provide a clearer overview of these relationships, Table 4 presents the reported cell viability and hemolysis data, grouping toxicity outcomes by particle architecture and surface chemistry to identify safer design windows for clinical application.

10. Limitations and future scope

10.1. Key limitations of Ln-IONPs

Despite significant progress, the rational design of lanthanide-based iron oxide nanoparticles (Ln-IONPs) with simultaneously high luminescence efficiency and strong magnetic performance remains challenging. A central challenge in Ln-IONPs is the inherent incompatibility between lanthanide luminescence and iron oxide magnetism. Iron oxide nanoparticles possess dense electronic states and strong spin–lattice coupling, which act as efficient nonradiative energy acceptors for excited lanthanide ions. As a result, the direct integration of luminescent Ln^{3+} centers with iron oxide cores often leads to severe photoluminescence quenching. This fundamental issue limits the optical performance of Ln-IONPs and necessitates careful architectural design. Therefore, the difficulty lies not merely in combining iron oxide nanoparticles (IONPs) with lanthanide-based luminescent materials, but in engineering a nanoscale architecture that suppresses interfacial quenching while preserving magnetic saturation. Luminescence quenching caused by nonradiative energy transfer from excited Ln^{3+} ions to the iron oxide core remains the most critical limitation. To mitigate this effect, a minimum spatial separation between the magnetic and luminescent components is required. The introduction of ultrathin but optically inert buffer layers with controlled thickness can effectively suppress quenching while minimizing magnetic dilution. Advanced shell materials with low phonon energies and high chemical stability, as well as gradient or asymmetric architectures, may offer improved balance between optical insulation and magnetic efficiency. Consequently, inorganic (*e.g.*, SiO_2) or organic (*e.g.*, polymer) spacer layers are commonly introduced, where lanthanide emitters are either doped into the coating layer or grafted onto its surface. However, such distancing strategies often necessitate multistep synthetic routes, increasing structural complexity and reducing reproducibility, which rely on precise synthetic routes involving sequential coating, functionalization, and post-modification processes. While these approaches provide flexibility, they often suffer from poor reproducibility, limited scalability, and batch-to-batch variability. Moreover, the difficulty in achieving stable chemical bonding between luminescent components and coating layers frequently restricts synthetic strategies to physical insertion or weak surface attachment due to the difficulty in achieving robust chemical bonding between luminescent components and the coating layer. Inadequate embedding or weak surface binding can lead to lanthanide leaching, particularly under physiological conditions, compromising both optical stability and biosafety. Although multilayered architectures have been introduced to suppress leaching and quenching, these strategies often exacerbate other issues. Surface coating inevitably increases particle size and introduces diamagnetic components, resulting in reduced saturation magnetization (M_S). Enlarged hydrodynamic diameter and diminished magnetic response can adversely affect biological performance, particularly for applications that require efficient cellular uptake, prolonged circulation, or magnetic manipulation. Although Ln-based iron oxide nanoparticles offer great promise as T_1–T_2 dual-modal MRI contrast agents, their development remains at an early stage. Magnetic coupling between iron oxide cores and paramagnetic lanthanide ions can disrupt relaxation mechanisms, often diminishing T_1 contrast efficiency. Additionally, ultrasmall iron oxide nanoparticles can simultaneously contribute to both r_1 and r_2 relaxivities, complicating signal interpretation. Upconversion nanoparticles (UCNPs) based Ln-IONPs have gained attention for theranostic applications due to near-infrared excitation and magnetic targeting capabilities. However, the presence of iron oxide significantly reduces the upconversion quantum efficiency, limiting imaging depth and sensitivity. Multi-activator strategies have shown limited success due to cross-relaxation effects. Thus, a fundamental trade-off exists between luminescence preservation and magnetic performance, underscoring the need for more precise structural control.

10.2. Future directions

Ln-IONPs exhibit tremendous potential in diagnostics and theranostics because they offer numerous benefits over traditional biomarkers and therapeutic agents, due to the distinctive 4f orbitals of lanthanides and the strong magnetic properties of iron oxide NPs. Here, we highlight some potential future directions for research on Ln-IONPs aimed at achieving more effective and comprehensive functionalities.

(i) A primary future direction lies in developing advanced structural designs that effectively suppress interfacial luminescence quenching without significantly compromising magnetic performance. Rather than relying on thick insulating shells, future strategies should focus on ultrathin, low-phonon, and chemically stable buffer layers with precisely controlled thickness. Gradient shells, anisotropic architectures, and asymmetric heterostructures may offer new pathways to decouple optical and magnetic domains while minimizing magnetic dilution.

(ii) To facilitate translational applications, future efforts should prioritize the development of simplified and scalable synthetic methodologies. One-pot or self-assembly-driven approaches, as well as modular ligand-exchange strategies

that allow reproducible functionalization, could significantly reduce synthetic complexity. Emphasis should be placed on achieving batch-to-batch consistency, monodispersity, and robust surface chemistry compatible with biological environments.

(iii) Preventing lanthanide leaching remains essential for long-term optical stability and biosafety. Future research should explore covalent anchoring strategies, lattice incorporation, and cross-linked polymer or inorganic matrices that firmly immobilize luminescent centers. Designing chemically stable coordination environments resistant to hydrolysis and ion exchange under physiological conditions will be critical for *in vivo* applications.

(iv) Balancing high saturation magnetization with minimal particle size remains a central challenge. Future studies should focus on maximizing magnetic core efficiency through shape engineering, crystalline phase control, and dopant optimization. The use of magnetically active or multifunctional shells may compensate for magnetic losses induced by surface coatings, enabling smaller yet magnetically responsive Ln-IONPs suitable for biological use.

(v) The development of reliable T_1–T_2 dual-modal MRI contrast agents based on Ln-IONPs remains in its infancy. Future research should systematically investigate how nanoscale structural parameters, such as core–shell spacing, ion distribution, and surface chemistry, govern spin relaxation mechanisms. Decoupling T_1-active lanthanide centers from T_2-dominant iron oxide cores through rational architecture design could enable more sensitive and accurate dual-modal imaging. Compared to the rapid-paced development of the single-modal contrast agents (T_1 or T_2), research on Ln^{3+}-based iron oxide dual-modal CAs is still in its early stages. To simultaneously achieve high sensitivity and biocompatibility, a complementary T_1–T_2 dual-modal contrast agent (CA) that provides both T_1 and T_2 signals is highly desirable for the precise diagnosis. For future work, the following factors should be taken into consideration: (a) the IONPs can interfere with the relaxation process of the paramagnetic lanthanide-based T_1 contrast agents (*e.g.* Gd^{3+} or Eu^{3+}) and can thus significantly reduce the T_1 signal. Specifically, when the size of IONPs decreased to ultrasmall dimensions, the IONPs showed r_2 for T_2 contrast agents and also r_1 for T_1-weighted images. Therefore, the combined influences of size, shape, crystal structure, doping percentage and surface functionalities on the electronic spin properties of Gd^{3+}, Eu^{3+}, Fe^{3+}, and Fe^{2+} ions should be investigated more thoroughly. (b) More improvements must be made to the synthesis methods in terms of producing monodisperse nanoparticles; the method must be well-controlled and reproducible, and optimum conditions should be explored for coating with a water-dispersible layer. Furthermore, the majority of the identified CAs still have only *in vitro* testing or preliminary animal research as their diagnostic applications. In order to expand the use of nanoparticles in clinical settings, it is required that their biocompatibility, pharmacokinetics, biodistribution, and metabolism be assessed.

(vi) Upconversion-based Ln-IONPs hold great promise for deep-tissue imaging and theranostics due to their NIR-triggered emissions, magnetic guiding ability and heat-producing efficiency; however, their optical efficiency is still limited in magnetically active environments. Future strategies should include the incorporation of antenna ligands, sensitizer-rich architectures, and plasmonic enhancement to improve excitation efficiency and emission intensity. Careful control of interfacial coupling and electromagnetic interactions is essential to avoid additional quenching effects. For further advancement of UCNPs-based Ln-IONPS, the following aspects should be considered: (a) deep-tissue imaging makes upconversion luminescence attractive towards biological applications, but their relatively low quantum yield in the presence of iron oxide limits the optical applications. The establishment of an effective strategy to significantly enhance the efficiency of upconversion emissions has always been highly desirable. Multi-activator containing upconversion systems have been introduced to overcome this issue, but cross-relaxation prevents them from obtaining the expected photoluminescence intensity. The introduction of antenna ligands that can donate energy to Ln^{3+} luminescent centers will be a possible way to address low UCL intensity in the presence of IONPs. Furthermore, instead of a silica or polymer layer, using a layer of plasmonic material (gold or silver) on iron oxide nanoparticles might boost the luminescence intensity due to the surface plasmon effect. More investigations are necessary in the future to explore the efficacy of these methods. (b) For *in vitro* and *in vivo* testing, bioimaging and therapeutic models are, at present, mainly focused on the cells (*in vitro*) and on the mice (*in vivo*). To improve the UCNPs-based IONPs bioimaging applications, additional biological models, such as those of large animals and plants, should be considered. Future research should expand biological testing to include large animal models, long-term toxicity studies, and comprehensive pharmacokinetic analyses. Standardized protocols for biosafety, biodistribution, and clearance will be essential to bridge the gap between laboratory research and clinical translation.

(vii) Future work should focus on rational lanthanide selection and doping-level optimization to precisely tune magnetic anisotropy and relaxation dynamics for maximized SAR under clinically relevant field conditions.

(viii) For biomedical applications, the long-term biodistribution, degradation, and clearance of lanthanide-based iron oxide nanoparticles (Ln-IONPs) are critical factors governing their safety and clinical feasibility. Following systemic administration, Ln-IONPs are predominantly sequestered by the mononuclear phagocyte system (MPS), with major accumulation occurring in the liver and spleen due to uptake by Kupffer cells and splenic macrophages. The clearance pathway of Ln-IONPs is strongly dependent on particle size, surface chemistry, and structural integrity. Ultrasmall nanoparticles (hydrodynamic diameter typically <5–6 nm) or their degradation products may undergo partial renal clearance, whereas larger or aggregated particles are primarily eliminated through hepatobiliary pathways. Iron oxide cores are generally biodegradable under physiological conditions, where Fe^{2+}/Fe^{3+} ions can enter endogenous iron metabolic pathways, including storage in ferritin or incorporation into hemoglobin. In

contrast, lanthanide ions do not participate in natural metabolic cycles and may pose long-term accumulation risks if released from the nanoparticle matrix. The stable immobilization of lanthanide components within inert lattices, chelated coordination environments, or robust core–shell architectures is therefore essential to minimize ion leaching. Surface coatings that resist enzymatic degradation and prevent the premature release of lanthanide ions play a crucial role in ensuring long-term biosafety. Future design strategies should focus on developing biodegradable or transformable Ln-IONPs that undergo controlled structural disassembly into renally- or hepatobiliary-clearable components over time. Additionally, long-term *in vivo* studies evaluating chronic toxicity, bioaccumulation, and clearance kinetics across multiple biological models will be indispensable for advancing Ln-IONPs toward clinical translation.

(ix) Future progress in Ln-IONPs will benefit from the closer integration of theoretical modeling, simulation, and advanced characterization techniques. Predictive models that correlate structure with optical and magnetic behavior can guide experimental design, reduce trial-and-error synthesis, and accelerate the optimization of multifunctional nanoplatforms.

11. Conclusions

Lanthanide-based iron oxide nanoparticles (Ln-IONPs) have evolved into one of the most promising classes of multifunctional nanoplatforms for next-generation biomedical technologies. By integrating the sharp, stable luminescence of lanthanide ions with the superparamagnetism and biocompatibility of iron oxide, these hybrid nanostructures offer unparalleled opportunities for multimodal imaging, magnetically actuated drug delivery, and image-guided therapy. Over the past decade, significant progress has been made in tailoring the structural design of Ln-IONPs through controlled doping, buffer-layer engineering, polymer integration, and advanced synthetic strategies, such as thermal decomposition, hydro(-solvo)thermal growth, microwave-assisted crystallization, and sol–gel assembly. These developments have enabled improved photostability, enhanced magnetic relaxivity, reduced fluorescence quenching, and more sophisticated multifunctional architectures. Despite these advances, several challenges remain before Ln-IONPs can fully transition from laboratory demonstrations to clinical use. Foremost among these are the persistent luminescence quenching caused by the proximity of iron oxide, the need for optimized core–shell interfaces, and the difficulty in achieving both high magnetic response and bright luminescence within a single construct. Furthermore, comprehensive *in vivo* studies are still required to assess long-term toxicity, biodegradation pathways, immune interactions, and organ clearance. Addressing these limitations will require a deeper understanding of interfacial energy transfer, dopant distribution, and the physicochemical properties that dictate biological fate. Innovations in surface chemistry, polymer-templated assembly, inert spacer layers, hollow nanoreactors, and stimuli-responsive coatings are expected to accelerate the development of Ln-IONPs with higher diagnostic accuracy and stronger therapeutic performance. Combining optical, magnetic, thermal, and chemical functionalities within a single, compact nanoplatform opens new doors for precision nanomedicine, including multimodal imaging, real-time therapy monitoring, and synergistic photothermal-photodynamic treatments. With continued advances in rational design and biocompatible engineering, Ln-IONPs hold substantial promise as clinically relevant agents for integrated diagnosis and therapy.

Author contributions

Tanvir Hossain – investigation, data curation, and original draft preparation; Md. Shamiull Alim Munna – investigation, methodology development, writing, and original draft preparation; Md. Shahidul Islam – formal analysis, validation, and reviewing; O. Thompson Mefford – conceptualization, supervision, and critical reviewing; Hasan Ahmad – resources, project administration, and reviewing; and Md. Mahbubor Rahman – conceptualization, supervision, funding acquisition, and final manuscript reviewing and editing.

Conflicts of interest

The authors declare that there are no financial interests or personal relationships that could have influenced the work presented in this article.

Abbreviations

1-ODE	1-Octadecene
AA or acac	Acetylacetonate
AMD	Polyamino-dextran
AMF	Alternating magnetic field
APTES	3-Aminopropyl triethoxysilane
BA	Benzoate
CAs	Contrast agents
CCK-8	Cholecystokinin-8 or cell counting kit-8
CD	β-Cyclodextrin
CMC	Carboxymethylcellulose
CT	Computed tomography
dam	*N*,*N*-Dimethylacetamide
DBM	Dibenzoylmethane
DC	Down-conversion
DCL	Down-conversion luminescence
DDA	1,10-Decanedicarboxylic acid
DOTA	1,4,7,10-Tetraazacyclododecane-1,4,7,10-tetraacetic acid
DTPA	Diethylenetriaminepentaacetic acid
EDTA	Ethylenediaminetetraacetic acid
ETU	Energy transfer upconversion
FDA	Food and drug administration
GMA	Glycidyl methacrylate
GPTMS	3-Glycidoxypropyltrimethoxysilane
HA	Hyaluronic acid
HAS	Human serum albumin
IONPs	Iron oxide nanoparticles

ISC	Intersystem crossing
LCMD	Light conversion molecular devices
LD	Laser diode
LMCT	Ligand-to-metal charge transfer
Ln	Lanthanide(s)
Ln-IONPs	Lanthanide-based iron oxide nanoparticles
Ln-NPs	Lanthanide nanoparticles
MAPTMS	3-Methacryloxypropyltrimethoxysilane
MF	Magnetic field
MFH	Magnetic fluid hyperthermia
MFNPs	Multifunctional nanoparticles
MH	Magnetic hyperthermia
MLHNPs	Magnetic luminescent hybrid nanoparticles
mMSCs	mouse mesenchymal stem cells
MNPs	Magnetic nanoparticles
MPTMA	3-(Trimethoxysilyl)propyl methacrylate
MRI	Magnetic resonance imaging
MTS	3-(4,5-Dimethylthiazol-2-yl)-5-(3-carboxymethoxyphenyl)-2-(4-sulfophenyl)-2*H*-tetrazolium
MTT	3-(4,5-Dimethylthiazol-2-yl)-2,5-diphenyltetrazolium Bromide
MUA	11-Mercaptoundecanoic acid
NCs	Nanocomposites
NFE	Near-field enhancement
NIR	Near infra-red
NPs	Nanoparticles
OA	Oleic acid
PAA	Polyacrylic acid
PAMAM	Poly(amidoamine)
PANI	Polyaniline
PEG	Polyethylene glycol
PET	Polyethylene terephthalate
phen	1,10-Phenanthroline
PL	Photoluminescent
PMAO	Polymethylaluminoxane
PMMA	Poly(methyl methacrylate)
PNIPAM	Poly(*N*-isopropylacrylamide)
poly(St-NIPAM)	poly(Styrene-*co*-*N*-isopropylacrylamide)
PTT	Photothermal therapy
PVP	Polyvinylpyrrolidone
QDs	Quantum dots
RE	Rare earth
SAR	Specific absorption rate
SOC	Spin–orbit coupling
SPIONs	Superparamagnetic iron oxide nanoparticles
SPR	Surface plasmon resonance
SSP	Single-source precursor
TEOS	Tetraethoxysilane
tta	2-Thenoyltrifluoroacetone
TTA	Thenoyltrifluoroacetone
UC	Up-conversion
UCL	Up-conversion luminescence
UCNPs	Up-conversion nanoparticles
XTT	2,3-Bis-(2-methoxy-4-nitro-5-sulfophenyl)-2*H*-tetrazolium-5-carboxanilide

Data availability

This article is a review and does not involve the generation of primary datasets. All data supporting the discussion are available in the cited literature and referenced sources.

Acknowledgements

The authors gratefully acknowledge the Ministry of Science and Technology, Bangladesh, for financial support of this work. We also thank the Polymer Colloids and Nanomaterials (PCN) Research Lab and the researchers who assisted with chemical analyses for their valuable support.

References

1 M. Norek and J. A. M. Peters, Contrast Agents Based on Dysprosium or Holmium, *Prog. Nucl. Magn. Reson. Spectrosc.*, 2011, **59**, 64.
2 B. Wang, S. Jiang, X. Wang and S. Gao, Magnetic molecular materials with paramagnetic lanthanide ions, *Sci. China, Ser. B: Chem.*, 2009, **52**(11), 1739–1758.
3 S. Viswanathan, Z. Kovacs, K. N. Green, S. J. Ratnakar and A. D. Sherry, Alternatives to Gadolinium-Based Metal Chelates for Magnetic Resonance Imaging, *Chem*, 2010, **110**, 2960.
4 Y. Wang, K. Zheng, S. Song, D. Fan, H. Zhang and X. Liu, Remote manipulation of upconversion luminescence, *Chem. Soc. Rev.*, 2018, **47**(17), 6473–6485.
5 M. Montalti, L. Prodi, N. Zaccheroni, L. Charbonnière, L. Douce and R. Ziessel, A luminescent anion sensor based on a europium hybrid complex, *J. Am. Chem. Soc.*, 2001, **123**(50), 12694–12695.
6 L.-D. Sun, Y.-F. Wang and C.-H. Yan, Paradigms and challenges for bioapplication of rare earth upconversion luminescent nanoparticles: small size and tunable emission/excitation spectra, *Accounts Chem. Res.*, 2014, **47**(4), 1001–1009.
7 F. Wang and X. Liu, Recent advances in the chemistry of lanthanide-doped upconversion nanocrystals, *Chem. Soc. Rev.*, 2009, **38**(4), 976–989.
8 Y. Liu, D. Tu, H. Zhu and X. Chen, Lanthanide-doped luminescent nanoprobes: controlled synthesis, optical spectroscopy, and bioapplications, *Chem. Soc. Rev.*, 2013, **42**(16), 6924–6958.
9 S. S. Lucky, K. C. Soo and Y. Zhang, Nanoparticles in photodynamic therapy, *Chem. Rev.*, 2015, **115**(4), 1990–2042.
10 L. Cheng, C. Wang, L. Feng, K. Yang and Z. Liu, Functional nanomaterials for phototherapies of cancer, *Chem. Rev.*, 2014, **114**(21), 10869–10939.
11 S. Kossatz, *et al.*, Efficient treatment of breast cancer xenografts with multifunctionalized iron oxide nanoparticles combining magnetic hyperthermia and anti-cancer drug delivery, *Breast Cancer Res.*, 2015, **17**(1), 1–17.

12 X. Liu, *et al.*, Comprehensive understanding of magnetic hyperthermia for improving antitumor therapeutic efficacy, *Theranostics*, 2020, **10**(8), 3793–3815, DOI: 10.7150/thno.40805.
13 H. Xin, F. Y. Li, M. Shi, Z. Q. Bian and C. H. Huang, Efficient electroluminescence from a new terbium complex, *J. Am. Chem. Soc.*, 2003, **125**(24), 7166–7167.
14 J. Yu, D. Parker, R. Pal, R. A. Poole and M. J. Cann, A europium complex that selectively stains nucleoli of cells, *J. Am. Chem. Soc.*, 2006, **128**(7), 2294–2299.
15 I. A. Hemmilä and I. L. Hemmila, *Applications of Fluorescence in Immunoassays*, Wiley-Interscience, 1991, vol. 117.
16 B. Wang, J. Hai, Q. Wang, T. Li and Z. Yang, Coupling of luminescent terbium complexes to Fe3O4 nanoparticles for imaging applications, *Angew. Chem.*, 2011, **123**(13), 3119–3122.
17 J. Wang, *et al.*, First oxadiazole-functionalized terbium (III) $β$-diketonate for organic electroluminescence, *J. Am. Chem. Soc.*, 2001, **123**(25), 6179–6180.
18 J. Kido and Y. Okamoto, Organo lanthanide metal complexes for electroluminescent materials, *Chem. Rev.*, 2002, **102**(6), 2357–2368.
19 K. Binnemans, Lanthanide-based luminescent hybrid materials, *Chem. Rev.*, 2009, **109**(9), 4283–4374.
20 T. K. Christopoulos and E. P. Diamandis, *Fluorescence Immunoassays*, Academic Press, Inc., 1996, DOI: 10.1016/b978-012214730-2/50015-7.
21 G. A. Crosby, R. E. Whan and J. J. Freeman, Spectroscopic studies of rare earth chelates, *J. Phys. Chem.*, 1962, **66**(12), 2493–2499.
22 R. E. Whan and G. A. Crosby, Luminescence studies of rare earth complexes: benzoylacetonate and dibenzoylmethide chelates, *J. Mol. Spectrosc.*, 1962, **8**(1–6), 315–327.
23 G. A. Crosby, R. E. Whan and R. M. Alire, Intramolecular energy transfer in rare earth chelates. Role of the triplet state, *J. Chem. Phys.*, 1961, **34**(3), 743–748.
24 A. V Hayes and H. G. Drickamer, High pressure luminescence studies of energy transfer in rare earth chelates, *J. Chem. Phys.*, 1982, **76**(1), 114–125.
25 S. Sato and M. Wada, Relations between intramolecular energy transfer efficiencies and triplet state energies in rare earth $β$-diketone chelates, *Bull. Chem. Soc. Jpn.*, 1970, **43**(7), 1955–1962.
26 M. Tanaka, G. Yamaguchi, J. Shiokawa and C. Yamanaka, Mechanism and rate of the intramolecular energy transfer in rare earth chelates, *Bull. Chem. Soc. Jpn.*, 1970, **43**(2), 549–550.
27 O. L. Malta, Ligand—rare-earth ion energy transfer in coordination compounds. A theoretical approach, *J. Lumin.*, 1997, **71**(3), 229–236.
28 S. Petoud, J.-C. G. Bünzli, T. Glanzman, C. Piguet, Q. Xiang and R. P. Thummel, Influence of charge-transfer states on the Eu (III) luminescence in mononuclear triple helical complexes with tridentate aromatic ligands, *J. Lumin.*, 1999, **82**(1), 69–79.
29 W. M. Faustino, O. L. Malta and G. F. De Sá, Intramolecular energy transfer through charge transfer state in lanthanide compounds: a theoretical approach, *J. Chem. Phys.*, 2005, **122**(5), 54109.
30 W. H. Fonger and C. W. Struck, Eu+ 3 5 D Resonance Quenching to the Charge-Transfer States in Y2O2S, La2O2S, and LaOCl, *J. Chem. Phys.*, 1970, **52**(12), 6364–6372.
31 N. Filipescu, W. F. Sager and F. A. Serafin, Substituent effects on intramolecular energy transfer. II. Fluorescence spectra of europium and terbium $β$-diketone chelates, *J. Phys. Chem.*, 1964, **68**(11), 3324–3346.
32 P. M. Marcos, *et al.*, Lanthanide cation binding properties of homooxacalixarene diethylamide derivatives, *Supramol. Chem.*, 2011, **23**(1–2), 93–101, DOI: 10.1080/10610278.2010.510562.
33 G. F. De Sa, *et al.*, Spectroscopic properties and design of highly luminescent lanthanide coordination complexes, *Coord. Chem. Rev.*, 2000, **196**(1), 165–195.
34 Y. S. Yang, M. L. Gong, Y. Y. Li, H. Y. Lei and S. L. Wu, Effects of the structure of ligands and their Ln3+ complexes on the luminescence of the central Ln3+ ions, *J. Alloys Compd.*, 1994, **207**, 112–114.
35 L.-R. Lin, H.-H. Tang, Y.-G. Wang, X. Wang, X.-M. Fang and L.-H. Ma, Functionalized lanthanide (III) complexes constructed from azobenzene derivative and $β$-diketone ligands: Luminescent, magnetic, and reversible trans-to-cis photoisomerization properties, *Inorg. Chem.*, 2017, **56**(7), 3889–3900.
36 Z. Ahmed and K. Iftikhar, Sensitization of visible and NIR emitting lanthanide (III) ions in noncentrosymmetric complexes of hexafluoroacetylacetone and unsubstituted monodentate pyrazole, *J. Phys. Chem. A*, 2013, **117**(44), 11183–11201.
37 J. Yuasa, T. Nakagawa, Y. Kita, A. Kaito and T. Kawai, Photoactivatable europium luminescence turn-on by photo-oxygenation of $β$-diketone having pyrrole rings, *Chem. Commun.*, 2017, **53**(50), 6748–6751.
38 S. V. Eliseeva, D. N. Pleshkov, K. A. Lyssenko, L. S. Lepnev, J.-C. G. Bunzli and N. P. Kuzmina, Deciphering three beneficial effects of 2, 2′-bipyridine-N, N′-dioxide on the luminescence sensitization of lanthanide (III) hexafluoroacetylacetonate ternary complexes, *Inorg. Chem.*, 2011, **50**(11), 5137–5144.
39 M. Li, Y. Zhou, Y. Yao, T. Gao, P. Yan and H. Li, Designing water-quenching resistant highly luminescent europium complexes by regulating the orthogonal arrangement of bis-$β$-diketone ligands, *Dalton Trans.*, 2021, **50**(28), 9914–9922.
40 T. Zhu, P. Chen, H. Li, W. Sun, T. Gao and P. Yan, Structural effects on the photophysical properties of mono-$β$-diketonate and bis-$β$-diketonate Eu III complexes, *Phys. Chem. Chem. Phys.*, 2015, **17**(24), 16136–16144.
41 J. Vipond, *et al.*, A bridge to coordination isomer selection in lanthanide(III) DOTA-tetraamide complexes, *Inorg. Chem.*, 2007, **46**(7), 2584–2595, DOI: 10.1021/ic062184+.
42 L. Fusaro, F. Mocci, R. N. Muller and M. Luhmer, Insight into the dynamics of lanthanide-DTPA complexes as

revealed by oxygen-17 NMR, *Inorg. Chem.*, 2012, **51**(15), 8455–8461, DOI: 10.1021/ic3010085.

43 D. R. Reddy, L. E. Pedró Rosa and L. W. Miller, Luminescent trimethoprim - Polyaminocarboxylate lanthanide complex conjugates for selective protein labeling and time-resolved bioassays, *Bioconjugate Chem.*, 2011, **22**(7), 1402–1409, DOI: 10.1021/bc200131k.

44 S. L. Clegg and P. R. Zalupski, Ion Interaction Models and Measurements of Eu3+ Complexation: DTPA in Aqueous Solutions at 25 °C Containing 1:1 Na+ Salts and Malonate pH Buffer, *Ind. Eng. Chem. Res.*, 2016, **55**(7), 2097–2118, DOI: 10.1021/acs.iecr.5b03920.

45 D. Maffeo, *et al.*, Novel polycarboxylated EDTA-type cyclodextrins as ligands for lanthanide binding: Study of their luminescence, relaxivity properties of Gd(iii) complexes, and PM3 theoretical calculations, *Org. Biomol. Chem.*, 2010, **8**(8), 1910–1921, DOI: 10.1039/b924980j.

46 L. Xu, S. J. Rettig, C. Orvig, M. Mall and B. C. Vt, *"XuL01InorgChem.pdf"*, 2001, pp. 3734–3738, 18.

47 J. J. Michels, J. Huskens and D. N. Reinhoudt, Noncovalent binding of sensitizers for lanthanide(III) luminescence in an EDTA-bis(β-cyclodextrin) ligand, *J. Am. Chem. Soc.*, 2002, **124**(9), 2056–2064, DOI: 10.1021/ja017025y.

48 K. Matharu, S. K. Mittal and S. K. A. Kumar, Conductometric performance of two-pole and five-ring conductivity cell probes for lanthanide determination using EDTA and DCTA as potential sequestering agents, *Ind. Eng. Chem. Res.*, 2012, **51**(35), 11328–11334, DOI: 10.1021/ie301141g.

49 X. P. Yang, B. S. Kang, W. K. Wong, C. Y. Su and H. Q. Liu, Syntheses, crystal structures, and luminescent properties of lanthanide complexes with tripodal ligands bearing benzimidazole and pyridine groups, *Inorg. Chem.*, 2003, **42**(1), 169–179, DOI: 10.1021/ic025799p.

50 S. Bala, *et al.*, Construction of Polynuclear Lanthanide (Ln = DyIII, TbIII, and NdIII) Cage Complexes Using Pyridine-Pyrazole - Based Ligands: Versatile Molecular Topologies and SMM Behavior, *Inorg. Chem.*, 2015, **54**(17), 8197–8206, DOI: 10.1021/acs.inorgchem.5b00334.

51 C. S. Bonnet, *et al.*, A Pyridine-Based Ligand with Two Hydrazine Functions for Lanthanide Chelation: Remarkable Kinetic Inertness for a Linear, Bishydrated Complex, *Inorg. Chem.*, 2015, **54**(12), 5991–6003, DOI: 10.1021/acs.inorgchem.5b00804.

52 M. Heitzmann, *et al.*, Comparison of two tetrapodal N,O ligands: Impact of the softness of the heterocyclic N-donors pyridine and pyrazine on the selectivity for Am(lll) over Eu(lll), *Inorg. Chem.*, 2009, **48**(1), 246–256, DOI: 10.1021/ic8017024.

53 F. A. A. Paz, S. M. F. Vilela and J. P. C. Tomé, Layered metal-organic frameworks based on octahedral lanthanides and a phosphonate linker: Control of crystal size, *Cryst. Growth Des.*, 2014, **14**(10), 4873–4877, DOI: 10.1021/cg500875m.

54 P. Hermann, *"Department of Inorganic Chemistry, Univerzita Karlova (Charles University), Hlavova 2030, 12843 Prague 2, Czech Republic School of Chemical Sciences, Dublin City University, Glasnevin, Dublin 9, Ireland"*, 2012.

55 A. R. Patterson, W. Schmitt and R. C. Evans, Lighting up two-dimensional lanthanide phosphonates: Tunable structure-property relationships toward visible and near-infrared emitters, *J. Phys. Chem. C*, 2014, **118**(19), 10291–10301, DOI: 10.1021/jp501359m.

56 S. Miyazaki, *et al.*, Dual Energy Transfer Pathways from an Antenna Ligand to Lanthanide Ion in Trivalent Europium Complexes with Phosphine-Oxide Bridges, *J. Phys. Chem. A*, 2020, **124**(33), 6601–6606, DOI: 10.1021/acs.jpca.0c02224.

57 C. Boehme and G. Wipff, Carbamoylphosphine oxide complexes of trivalent lanthanide cations: Role of counterions, ligand binding mode, and protonation investigated by quantum mechanical calculations, *Inorg. Chem.*, 2002, **41**(4), 727–737, DOI: 10.1021/ic010658t.

58 H. Iwanaga and F. Aiga, Quantum Yield and Photoluminescence Intensity Enhancement Effects of a Diphosphine Dioxide Ligand on a 6-Coordinate Eu(III)-β-Diketonate Complex with Low Luminescence, *ACS Omega*, 2021, **6**(1), 416–424, DOI: 10.1021/acsomega.0c04826.

59 P. Ghosh, P. K. Bharadwaj, J. Roy and S. Ghosh, Transition metal (II)/(III), Eu(III), and Tb(III) ions induced molecular photonic OR gates using trianthryl cryptands of varying cavity dimension, *J. Am. Chem. Soc.*, 1997, **119**(49), 11903–11909, DOI: 10.1021/ja9713441.

60 T. F. Jenkins, D. H. Woen, L. N. Mohanam, J. W. Ziller, F. Furche and W. J. Evans, Tetramethylcyclopentadienyl Ligands Allow Isolation of Ln(II) Ions across the Lanthanide Series in [K(2.2.2-cryptand)][(C5Me4H)3Ln] Complexes, *Organometallics*, 2018, **37**(21), 3863–3873, DOI: 10.1021/acs.organomet.8b00557.

61 M. E. Fieser, *et al.*, Structural, spectroscopic, and theoretical comparison of traditional vs recently discovered Ln2+ ions in the [K(2.2.2-cryptand)][(C5H4SiMe3)3Ln] complexes: The variable nature of Dy2+ and Nd2+, *J. Am. Chem. Soc.*, 2015, **137**(1), 369–382, DOI: 10.1021/ja510831n.

62 A. F. Danil de Namor and O. Jafou, Complexation of calixarene derivatives and lanthanide cations in nonaqueous media, *J. Phys. Chem. B*, 2001, **105**(33), 8018–8027, DOI: 10.1021/jp011124g.

63 J. C. G. Bünzli, F. Besançon and F. Ihringer, Bimetallic lanthanide supramolecular edifices with calixarenes, *ACS Symp. Ser.*, 2000, **757**, 179–194, DOI: 10.1021/bk-2000-0757.ch014.

64 F. Arnaud-Neu, S. Barboso, D. Byrne, L. J. Charbonnière, M. J. Schwing-Weill and G. Ulrich, Binding of lanthanides(III) and thorium(IV) by phosphorylated calixarenes, *ACS Symp. Ser.*, 2000, **757**, 150–164, DOI: 10.1021/bk-2000-0757.ch012.

65 N. Sabbatini, M. Guardigli, I. Manet, F. Bolletta and R. Ziessel, Synthesis and Luminescence of Lanthanide Complexes of a Branched Macrocyclic Ligand Containing 2,2′-Bipyridine and 9-Methyl-1,10-phenanthroline Subunits, *Inorg. Chem.*, 1994, **33**(5), 955–959, DOI: 10.1021/ic00083a020.

66 L. Prodi, M. Maestri, V. Balzani and R. Ziessel, Luminescent Eu3+, Tb3+, and Gd3+ Complexes of a Branched-Triazacyclononane Ligand Containing Three 2,2′ -Bipyridine Units, *Inorg. Chem.*, 1991, **30**(20), 3798–3802, DOI: 10.1021/ic00020a006.

67 J.-L. Liu, B. Yan and L. Guo, *"Photoactive Ternary Lanthanide-Centered Hybrids with Schiff-Base Functionalized Polysilsesquioxane Bridges and N-Heterocyclic Ligands"*, Wiley Online Library, 2010.

68 L. Armelao, *et al.*, Design of luminescent lanthanide complexes: From molecules to highly efficient photo-emitting materials, *Coord. Chem. Rev.*, 2010, **254**(5–6), 487–505.

69 V. Bekiari, G. Pistolis and P. Lianos, Intensely luminescent materials obtained by combining lanthanide ions, 2, 2 '-bipyridine, and poly (ethylene glycol) in various fluid or solid environments, *Chem. Mater.*, 1999, **11**(11), 3189–3195.

70 V. Bekiari, G. Pistolis and P. Lianos, Improvement of the emission properties of sol-gel silica matrices containing Eu3+ in the presence of poly (ethylene glycol)-200, *J. Non-Cryst. Solids*, 1998, **226**(1–2), 200–203.

71 P. Nockemann, *et al.*, Photostability of a highly luminescent europium $β$-diketonate complex in imidazolium ionic liquids, *Chem. Commun.*, 2005, **34**, 4354–4356.

72 M.-A. Néouze, J. Le Bideau and A. Vioux, Versatile heat resistant solid electrolytes with performances of liquid electrolytes, *Prog. Solid State Chem.*, 2005, **33**(2–4), 217–222.

73 M.-A. Néouze, J. Le Bideau, F. Leroux and A. Vioux, A route to heat resistant solid membranes with performances of liquid electrolytes, *Chem. Commun.*, 2005, (8), 1082–1084.

74 Y.-H. Han, A. Taylor, M. D. Mantle and K. M. Knowles, Sol-gel-derived organic–inorganic hybrid materials, *J. Non-Cryst. Solids*, 2007, **353**(3), 313–320.

75 H. R. Li, H. J. Zhang, J. Lin, S. B. Wang and K. Y. Yang, Preparation and luminescence properties of ormosil material doped with Eu (TTA) 3phen complex, *J. Non-Cryst. Solids*, 2000, **278**(1–3), 218–222.

76 B. Yan, Sol-gel preparation and luminescence of silica/polymer hybrid material incorporated with terbium complex, *Mater. Lett.*, 2003, **57**(16–17), 2535–2539.

77 S. S. Park, B. An and C.-S. Ha, High-quality, oriented and mesostructured organosilica monolith as a potential UV sensor, *Microporous Mesoporous Mater.*, 2008, **111**(1–3), 367–378.

78 Y. Wang, H. Li, Y. Feng, H. Zhang, G. Calzaferri and T. Ren, Orienting zeolite L microcrystals with a functional linker, *Angew. Chem.*, 2010, **122**(8), 1476–1480.

79 Q. Lü, A. Li, F. Guo, L. Sun and L. Zhao, Experimental study on the surface modification of Y2O3: Tm3+/Yb3+ nanoparticles to enhance upconversion fluorescence and weaken aggregation, *Nanotechnology*, 2008, **19**(14), 145701.

80 Z. Li, H. Guo, H. Qian and Y. Hu, Facile microemulsion route to coat carbonized glucose on upconversion nanocrystals as high luminescence and biocompatible cell-imaging probes, *Nanotechnology*, 2010, **21**(31), 315105.

81 G. Chen, C. Yang and P. N. Prasad, Nanophotonics and nanochemistry: Controlling the excitation dynamics for frequency up- and down-conversion in lanthanide-doped nanoparticles, *Acc. Chem. Res.*, 2013, **46**(7), 1474–1486, DOI: 10.1021/ar300270y.

82 A. Gnach and A. Bednarkiewicz, Lanthanide-doped up-converting nanoparticles: Merits and challenges, *Nano Today*, 2012, **7**(6), 532–563, DOI: 10.1016/j.nantod.2012.10.006.

83 A. C. Tropper, J. N. Carter, R. D. T. Lauder, D. C. Hanna, S. T. Davey and D. Szebesta, Analysis of blue and red laser performance of the infrared-pumped praseodymium-doped fluoride fiber laser, *J. Opt. Soc. Am. B*, 1994, **11**(5), 886–893.

84 K. B. Morebodi, S. N. Ogugua, V. Kumar and H. C. Swart, The effects of Eu3+ concentration on the photoluminescence of Na4Ca (PO3)6 phosphors prepared by a solid-state reaction method, *Chem. Phys. Impact*, 2024, **9**, 100718, DOI: 10.1016/j.chphi.2024.100718.

85 A. J. S. Silva, *et al.*, Tunable visible luminescence from Tb3+/Fe3+ co-doped LiAl5O8 under UV and X-ray excitation, *J. Lumin.*, 2025, **288**, 121497, DOI: 10.1016/j.jlumin.2025.121497.

86 J. Biswas and S. Jana, Visible luminescence and energy migration mechanism of Sm3+ in phospho-tellurite glasses by co-activating with Tb3+ ions for solid state lighting device applications, *Phys. B*, 2023, **657**, 414812, DOI: 10.1016/j.physb.2023.414812.

87 Y. Dai, *et al.*, Single-Composition White Light Emission from Dy3+ Doped Sr2CaWO6, *Materials*, 2019, **12**(3), 431, DOI: 10.3390/ma12030431.

88 J. Liang, T. Fan, J. Lü, T. Guan, T. Deng and B. Xiong, Dual-mode luminescence anti-counterfeiting and white light emission of $NaGdF_4$:Ce,Eu,Tb/carbon dot hydrophilic nanocomposite ink, *RSC Adv.*, 2023, **13**(37), 25681–25690, DOI: 10.1039/D3RA04368A.

89 Y. Lei, *et al.*, Microwave-assisted synthesis of hydrophilic $BaYF_5$:Tb/Ce,Tb green fluorescent colloid nanocrystals, *Dalton Trans.*, 2011, **40**(1), 142–145, DOI: 10.1039/C0DT00873G.

90 R. S. Perala, V. N. K. Putta, B. P. Singh, R. S. Ningthoujam and R. Acharya, Sorption Studies of Eu^{3+} Ions Using YPO_4 and YPO_4 :20% Ce Nanoparticles, Optical Properties, and in Conjunction with Instrumental Neutron Activation Analysis, *ACS Omega*, 2025, **10**(15), 14616–14625, DOI: 10.1021/acsomega.4c06813.

91 T. Grzyb, M. Runowski and S. Lis, Facile synthesis, structural and spectroscopic properties of GdF3:Ce3+, Ln3+ (Ln3+=Sm3+, Eu3+, Tb3+, Dy3+) nanocrystals with bright multicolor luminescence, *J. Lumin.*, 2014, **154**, 479–486, DOI: 10.1016/j.jlumin.2014.05.020.

92 K. Li, D. Chen, R. Zhang, Y. Yu, J. Xu and Y. Wang, Enhanced luminescence in Ce3+/Dy3+: Sr3Y2(BO3)4 phosphors via energy transfer, *Mater. Res. Bull.*, 2013, **48**(5), 1957–1960, DOI: 10.1016/j.materresbull.2013.01.042.

93 M. Runowski, S. Goderski, D. Przybylska, T. Grzyb, S. Lis and I. R. Martín, Sr_2 LuF_7 :Yb^{3+} –Ho^{3+} –Er^{3+} Upconverting Nanoparticles as Luminescent Thermometers in the First,

Second, and Third Biological Windows, *ACS Appl. Nano Mater.*, 2020, **3**(7), 6406–6415, DOI: 10.1021/acsanm.0c00839.

94 R. Komban, K. Koempe and M. Haase, Influence of different ligand isomers on the growth of lanthanide phosphate nanoparticles, *Cryst. Growth Des.*, 2011, **11**(4), 1033–1039.

95 D. Yang, *et al.*, Size and shape controllable synthesis and luminescent properties of BaGdF5: Ce3+/Ln3+ (Ln= Sm, Dy, Eu, Tb) nano/submicrocrystals by a facile hydrothermal process, *Nanoscale*, 2011, **3**(6), 2589–2595.

96 Q. Ju, Y. Liu, D. Tu, H. Zhu, R. Li and X. Chen, Lanthanide-Doped Multicolor GdF3 Nanocrystals for Time-Resolved Photoluminescent Biodetection, *Chem.–Eur. J.*, 2011, **17**(31), 8549–8554.

97 F. Wang, X. Fan, M. Wang and Y. Zhang, Multicolour PEI/NaGdF4: Ce3+, Ln3+ nanocrystals by single-wavelength excitation, *Nanotechnology*, 2006, **18**(2), 25701.

98 N. Niu, *et al.*, Tunable multicolor and bright white emission of one-dimensional NaLuF 4: Yb 3+, Ln 3+(Ln= Er, Tm, Ho, Er/Tm, Tm/Ho) microstructures, *J. Mater. Chem.*, 2012, **22**(21), 10889–10899.

99 G. Chen, *et al.*, Lanthanide-doped ultrasmall yttrium fluoride nanoparticles with enhanced multicolor upconversion photoluminescence, *J. Mater. Chem.*, 2012, **22**(38), 20190–20196.

100 S. Huang, *et al.*, Rapid, morphologically controllable, large-scale synthesis of uniform Y (OH) 3 and tunable luminescent properties of Y 2 O 3: Yb 3+/Ln 3+(Ln= Er, Tm and Ho), *J. Mater. Chem.*, 2012, **22**(31), 16136–16144.

101 X. Zhang, *et al.*, Facile and mass production synthesis of $β$-NaYF 4: Yb 3+, Er 3+/Tm 3+ 1D microstructures with multicolor up-conversion luminescence, *Chem. Commun.*, 2011, **47**(44), 12143–12145.

102 H. Qiu, *et al.*, Tuning the size and shape of colloidal cerium oxide nanocrystals through lanthanide doping, *Chem. Commun.*, 2011, **47**(34), 9648–9650.

103 F. C. J. M. van Veggel, C. Dong, N. J. J. Johnson and J. Pichaandi, Ln 3+-doped nanoparticles for upconversion and magnetic resonance imaging: some critical notes on recent progress and some aspects to be considered, *Nanoscale*, 2012, **4**(23), 7309–7321.

104 F. Wang, J. Wang and X. Liu, Direct evidence of a surface quenching effect on size-dependent luminescence of upconversion nanoparticles, *Angew. Chem., Int. Ed.*, 2010, **49**(41), 7456–7460.

105 J. Zhao, *et al.*, Upconversion luminescence with tunable lifetime in NaYF 4: Yb, Er nanocrystals: role of nanocrystal size, *Nanoscale*, 2013, **5**(3), 944–952.

106 C. Liu, *et al.*, Magnetic/upconversion fluorescent NaGdF4: Yb, Er nanoparticle-based dual-modal molecular probes for imaging tiny tumors in vivo, *ACS Nano*, 2013, **7**(8), 7227–7240.

107 N. J. J. Johnson, W. Oakden, G. J. Stanisz, R. Scott Prosser and F. C. J. M. van Veggel, Size-tunable, ultrasmall NaGdF4 nanoparticles: insights into their T1 MRI contrast enhancement, *Chem. Mater.*, 2011, **23**(16), 3714–3722.

108 Y. Li, T. Chen, W. Tan and D. R. Talham, Size-dependent MRI relaxivity and dual imaging with Eu0. 2Gd0. 8PO4·H2O nanoparticles, *Langmuir*, 2014, **30**(20), 5873–5879.

109 H.-X. Mai, Y.-W. Zhang, L.-D. Sun and C.-H. Yan, Highly efficient multicolor up-conversion emissions and their mechanisms of monodisperse NaYF4: Yb, Er core and core/shell-structured nanocrystals, *J. Phys. Chem. C*, 2007, **111**(37), 13721–13729.

110 A. Bagheri, H. Arandiyan, N. N. M. Adnan, C. Boyer and M. Lim, Controlled direct growth of polymer shell on upconversion nanoparticle surface via visible light regulated polymerization, *Macromolecules*, 2017, **50**(18), 7137–7147.

111 Z. Li, Y. Zhang, B. Shuter and N. Muhammad Idris, Hybrid lanthanide nanoparticles with paramagnetic shell coated on upconversion fluorescent nanocrystals, *Langmuir*, 2009, **25**(20), 12015–12018.

112 Y.-H. Chien, *et al.*, Near-infrared light photocontrolled targeting, bioimaging, and chemotherapy with caged upconversion nanoparticles in vitro and in vivo, *ACS Nano*, 2013, **7**(10), 8516–8528.

113 Z. Li, L. Wang, Z. Wang, X. Liu and Y. Xiong, Modification of NaYF4: Yb, Er@ SiO2 nanoparticles with gold nanocrystals for tunable green-to-red upconversion emissions, *J. Phys. Chem. C*, 2011, **115**(8), 3291–3296.

114 V. Mahalingam, F. Vetrone, R. Naccache, A. Speghini and J. A. Capobianco, Colloidal Tm3+/Yb3+-doped LiYF4 nanocrystals: multiple luminescence spanning the UV to NIR regions via low-energy excitation, *Adv. Mater.*, 2009, **21**(40), 4025–4028.

115 N. O. Nuñez, S. Rivera, D. Alcantara, M. Jesus, J. Garcia-Sevillano and M. Ocaña, Surface modified Eu: GdVO 4 nanocrystals for optical and MRI imaging, *Dalton Trans.*, 2013, **42**(30), 10725–10734.

116 A. Nsubuga, *et al.*, Facile preparation of multifunctionalisable 'stealth'upconverting nanoparticles for biomedical applications, *Dalton Trans.*, 2018, **47**(26), 8595–8604.

117 N. J. J. Johnson, A. Korinek, C. Dong and F. C. J. M. van Veggel, Self-focusing by Ostwald ripening: a strategy for layer-by-layer epitaxial growth on upconverting nanocrystals, *J. Am. Chem. Soc.*, 2012, **134**(27), 11068–11071.

118 X. Zhang, B. Blasiak, A. J. Marenco, S. Trudel, B. Tomanek and F. C. J. M. van Veggel, Design and regulation of NaHoF4 and NaDyF4 nanoparticles for high-field magnetic resonance imaging, *Chem. Mater.*, 2016, **28**(9), 3060–3072.

119 E. M. Chan, *et al.*, Combinatorial discovery of lanthanide-doped nanocrystals with spectrally pure upconverted emission, *Nano Lett.*, 2012, **12**(7), 3839–3845.

120 F. Auzel, Upconversion processes in coupled ion systems, *J. Lumin.*, 1990, **45**(1–6), 341–345.

121 R. A. Hewes and J. F. Sarver, Infrared excitation processes for the visible luminescence of Er 3+, Ho 3+, and Tm 3+ in Yb 3+-sensitized rare-earth trifluorides, *Phys. Rev.*, 1969, **182**(2), 427.

122 Y. Mita, Luminescence Processes in Yb3+-Sensitized Rare-Earth Phosphors, *J. Appl. Phys.*, 1972, **43**(4), 1772–1778.
123 R. B. Anderson, S. J. Smith, P. S. May and M. T. Berry, Revisiting the NIR-to-visible upconversion mechanism in $β$-NaYF4: Yb3+, Er3+, *J. Phys. Chem. Lett.*, 2014, **5**(1), 36–42.
124 E. M. Chan, Combinatorial approaches for developing upconverting nanomaterials: high-throughput screening, modeling, and applications, *Chem. Soc. Rev.*, 2015, **44**(6), 1653–1679.
125 W. Wei, *et al.*, Cross relaxation induced pure red upconversion in activator-and sensitizer-rich lanthanide nanoparticles, *Chem. Mater.*, 2014, **26**(18), 5183–5186.
126 J. R. Lakowicz, *Principles of Fluorescence Spectroscopy*, Springer, 2006.
127 W. Yu, W. Xu, H. Song and S. Zhang, Temperature-dependent upconversion luminescence and dynamics of NaYF 4: Yb 3+/Er 3+ nanocrystals: influence of particle size and crystalline phase, *Dalton Trans.*, 2014, **43**(16), 6139–6147.
128 D. Li, Q. Shao, Y. Dong and J. Jiang, Anomalous temperature-dependent upconversion luminescence of small-sized NaYF4: Yb3+, Er3+ nanoparticles, *J. Phys. Chem. C*, 2014, **118**(39), 22807–22813.
129 N. Vashistha, A. Chandra and M. Singh, HSA functionalized Gd 2 O 3: Eu 3+ nanoparticles as an MRI contrast agent and a potential luminescent probe for Fe 3+, Cr 3+, and Cu 2+ detection in water, *New J. Chem.*, 2020, **44**(33), 14211–14227.
130 N. Bogdan, F. Vetrone, G. A. Ozin and J. A. Capobianco, Synthesis of ligand-free colloidally stable water dispersible brightly luminescent lanthanide-doped upconverting nanoparticles, *Nano Lett.*, 2011, **11**(2), 835–840.
131 G. De, *et al.*, Effect of OH- on the upconversion luminescent efficiency of Y2O3: Yb3+, Er3+ nanostructures, *Solid State Commun.*, 2006, **137**(9), 483–487.
132 S. Xu, D. Fang, Z. Zhang and Z. Jiang, Effect of OH- on upconversion luminescence of Er3+-doped oxyhalide tellurite glasses, *J. Solid State Chem.*, 2005, **178**(6), 2159–2162.
133 N. Bogdan, F. Vetrone, G. A. Ozin and J. A. Capobianco, Synthesis of Ligand-Free Colloidally Stable Water Dispersible Brightly Luminescent Lanthanide-Doped Upconverting Nanoparticles, *Nano Lett.*, 2011, **11**(2), 835–840, DOI: 10.1021/nl1041929.
134 S. Sun and H. Zeng, Size-controlled synthesis of magnetite nanoparticles, *J. Am. Chem. Soc.*, 2002, **124**(28), 8204–8205, DOI: 10.1021/ja026501x.
135 W. Wu, C. Z. Jiang and V. A. L. Roy, Designed synthesis and surface engineering strategies of magnetic iron oxide nanoparticles for biomedical applications, *Nanoscale*, 2016, **8**(47), 19421–19474, DOI: 10.1039/c6nr07542h.
136 W. Wu, Z. Wu, T. Yu, C. Jiang and W.-S. Kim, Recent progress on magnetic iron oxide nanoparticles: synthesis, surface functional strategies and biomedical applications, *Sci. Technol. Adv. Mater.*, 2015, **16**(2), DOI: 10.1088/1468-6996/16/2/023501.
137 D. Kim, N. Lee, M. Park, B. H. Kim, K. An and T. Hyeon, Synthesis of uniform ferrimagnetic magnetite nanocubes, *J. Am. Chem. Soc.*, 2009, **131**(2), 454–455.
138 B. H. Kim, *et al.*, Sizing by weighing: characterizing sizes of ultrasmall-sized iron oxide nanocrystals using MALDI-TOF mass spectrometry, *J. Am. Chem. Soc.*, 2013, **135**(7), 2407–2410.
139 N. A. Frey, S. Peng, K. Cheng and S. Sun, Magnetic nanoparticles: synthesis, functionalization, and applications in bioimaging and magnetic energy storage, *Chem. Soc. Rev.*, 2009, **38**(9), 2532–2542.
140 J. Park, *et al.*, One-nanometer-scale size-controlled synthesis of monodisperse magnetic Iron oxide nanoparticles, *Angew. Chem.*, 2005, **117**(19), 2932–2937.
141 D. Shi, M. E. Sadat, A. W. Dunn and D. B. Mast, Photo-fluorescent and magnetic properties of iron oxide nanoparticles for biomedical applications, *Nanoscale*, 2015, **7**(18), 8209–8232.
142 A. Loudet and K. Burgess, BODIPY dyes and their derivatives: syntheses and spectroscopic properties, *Chem. Rev.*, 2007, **107**(11), 4891–4932.
143 C.-J. Yu, S.-M. Wu and W.-L. Tseng, Magnetite nanoparticle-induced fluorescence quenching of adenosine triphosphate-BODIPY conjugates: application to adenosine triphosphate and pyrophosphate sensing, *Anal. Chem.*, 2013, **85**(18), 8559–8565.
144 S. Fu, *et al.*, Multifunctional NaYF 4: Yb, Er@ PE 3@ Fe 3 O 4 nanocomposites for magnetic-field-assisted upconversion imaging guided photothermal therapy of cancer cells, *Dalton Trans.*, 2019, **48**(34), 12850–12857.
145 M. Aghazadeh, I. Karimzadeh, M. G. Maragheh and M. R. Ganjali, Enhancing the Supercapacitive and Superparamagnetic Performances of Iron Oxide Nanoparticles through Yttrium Cations Electro-chemical Doping, *Mater. Res.*, 2018, **21**(5), DOI: 10.1590/1980-5373-mr-2018-0094.
146 F. J. Douglas, *et al.*, Gadolinium-doped magnetite nanoparticles from a single-source precursor, *RSC Adv.*, 2016, **6**(78), 74500–74505, DOI: 10.1039/C6RA18095G.
147 C. S. Levin, *et al.*, Magnetic- plasmonic core- shell nanoparticles, *ACS Nano*, 2009, **3**(6), 1379–1388.
148 L. Tong, J. Shi, D. Liu, Q. Li, X. Ren and H. Yang, Luminescent and magnetic properties of Fe3O4@ SiO2@ Y2O3: Eu3+ composites with core–shell structure, *J. Phys. Chem. C*, 2012, **116**(12), 7153–7157.
149 S. Gai, *et al.*, Synthesis of magnetic, up-conversion luminescent, and mesoporous core–shell-structured nanocomposites as drug carriers, *Adv. Funct. Mater.*, 2010, **20**(7), 1166–1172.
150 Z. Y. Ma, D. Dosev, M. Nichkova, S. J. Gee, B. D. Hammock and I. M. Kennedy, Synthesis and bio-functionalization of multifunctional magnetic Fe3O4@Y2O3: Eu nanocomposites, *J. Mater. Chem.*, 2009, **19**(27), 4695–4700.
151 W. Wang, M. Zou and K. Chen, Novel Fe3O4@YPO4: Re (Re= Tb, Eu) multifunctional magnetic–fluorescent hybrid spheres for biomedical applications, *Chem. Commun.*, 2010, **46**(28), 5100–5102.

152 S. K. Swain, A. Sahoo, S. K. Swain, S. K. Tripathy and G. Phaomei, Synthesis of a novel $β$-cyclodextrin-functionalized Fe3O4/BaMoO4: Dy 3+ magnetic luminescent hybrid nanomaterial and its application as a drug carrier, *Dalton Trans.*, 2020, **49**(41), 14605–14612.

153 S. Sahu and S. Mohapatra, Multifunctional magnetic fluorescent hybrid nanoparticles as carriers for the hydrophobic anticancer drug 5-fluorouracil, *Dalton Trans.*, 2013, **42**(6), 2224–2231.

154 L. U. Khan, *et al.*, Fe3O4@ SiO2 nanoparticles concurrently coated with chitosan and GdOF: Ce3+, Tb3+ luminophore for bioimaging: toxicity evaluation in the zebrafish model, *ACS Appl. Nano Mater.*, 2019, **2**(6), 3414–3425.

155 L. Zhang, *et al.*, Magnetic/upconversion luminescent mesoparticles of Fe 3 O 4@ LaF 3: Yb 3+, Er 3+ for dual-modal bioimaging, *Chem. Commun.*, 2012, **48**(91), 11238–11240.

156 M. N. Luwang, S. Chandra, D. Bahadur and S. K. Srivastava, Dendrimer facilitated synthesis of multifunctional lanthanide based hybrid nanomaterials for biological applications, *J. Mater. Chem.*, 2012, **22**(8), 3395–3403.

157 M. Longmire, P. L. Choyke and H. Kobayashi, *"Clearance Properties of Nano-Sized Particles and Molecules as Imaging Agents: Considerations and Caveats"*, 2008.

158 G. Chen, T. Y. Ohulchanskyy, R. Kumar, H. Ågren and P. N. Prasad, Ultrasmall monodisperse NaYF4: Yb3+/Tm3+ nanocrystals with enhanced near-infrared to near-infrared upconversion photoluminescence, *ACS Nano*, 2010, **4**(6), 3163–3168.

159 F. J. Douglas, *et al.*, Gadolinium-doped magnetite nanoparticles from a single-source precursor, *RSC Adv.*, 2016, **6**(78), 74500–74505.

160 L. Yang, *et al.*, Europium-engineered iron oxide nanocubes with high T 1 and T 2 contrast abilities for MRI in living subjects, *Nanoscale*, 2015, **7**(15), 6843–6850.

161 J. Shen, L.-D. Sun, Y.-W. Zhang and C.-H. Yan, Superparamagnetic and upconversion emitting Fe 3 O 4/NaYF 4: Yb, Er hetero-nanoparticles via a crosslinker anchoring strategy, *Chem. Commun.*, 2010, **46**(31), 5731–5733.

162 A. Xia, *et al.*, Core-shell NaYF4:Yb3+,Tm3+@FexOy nanocrystals for dual-modality T2-enhanced magnetic resonance and NIR-to-NIR upconversion luminescent imaging of small-animal lymphatic node, *Biomaterials*, 2011, **32**(29), 7200–7208, DOI: 10.1016/j.biomaterials.2011.05.094.

163 D. Liu, D. Zhao, F. Shi, K. Zheng and W. Qin, Superparamagnetic and upconversion luminescent properties of Fe3O4/NaYF4: Yb, Er hetero-submicro-rods, *Mater. Lett.*, 2012, **85**, 1–3.

164 C. O. Kappe, Controlled microwave heating in modern organic synthesis, *Angew. Chem., Int. Ed.*, 2004, **43**(46), 6250–6284.

165 D. Adam, Microwave chemistry: Out of the kitchen, *Nature*, 2003, **421**(6923), 571–573.

166 R. Saillard, M. Poux, J. Berlan and M. Audhuy-Peaudecerf, Microwave heating of organic solvents: thermal effects and field modelling, *Tetrahedron*, 1995, **51**(14), 4033–4042.

167 E. Grant, B. J. Halstead, *et al.*, Dielectric parameters relevant to microwave dielectric heating, *Chem. Soc. Rev.*, 1998, **27**(3), 213–224.

168 X. Hu and J. C. Yu, Continuous aspect-ratio tuning and fine shape control of monodisperse $α$-Fe2O3 nanocrystals by a programmed microwave-hydrothermal method, *Adv. Funct. Mater.*, 2008, **18**(6), 880–887.

169 N. Shrivastava, *et al.*, Binary activated iron oxide/SiO 2/NaGdF 4: RE (RE= Ce, and Eu; Yb, and Er) nanoparticles: synthesis, characterization and their potential for dual T 1–T 2 weighted imaging, *New J. Chem.*, 2020, **44**(3), 832–844.

170 S. Shen, *et al.*, Dual-core@shell-structured Fe3O4-NaYF 4@TiO2 nanocomposites as a magnetic targeting drug carrier for bioimaging and combined chemo-sonodynamic therapy, *J. Mater. Chem. B*, 2014, **2**(35), 5775–5784, DOI: 10.1039/c4tb00841c.

171 S. E. Shirsath, M. L. Mane, Y. Yasukawa, X. Liu and A. Morisako, Self-ignited high temperature synthesis and enhanced super-exchange interactions of Ho3+-Mn2+-Fe3+-O2- ferromagnetic nanoparticles, *Phys. Chem. Chem. Phys.*, 2014, **16**(6), 2347–2357, DOI: 10.1039/c3cp54257b.

172 F. Zhang, *et al.*, Mesoporous multifunctional upconversion luminescent and magnetic 'nanorattle' materials for targeted chemotherapy, *Nano Lett.*, 2012, **12**(1), 61–67.

173 D. Dosev, *et al.*, Magnetic/luminescent core/shell particles synthesized by spray pyrolysis and their application in immunoassays with internal standard, *Nanotechnology*, 2007, **18**(5), 055102, DOI: 10.1088/0957-4484/18/5/055102.

174 M. Runowski and S. Lis, Synthesis, surface modification/decoration of luminescent-magnetic core/shell nanomaterials, based on the lanthanide doped fluorides (Fe3O4/SiO2/NH2/PAA/LnF3), *J. Lumin.*, 2016, **170**, 484–490, DOI: 10.1016/j.jlumin.2015.05.037.

175 H. Zhu, *et al.*, Magnetic, fluorescent, and thermo-responsive Fe3O4/rare earth incorporated poly(St-NIPAM) core-shell colloidal nanoparticles in multimodal optical/magnetic resonance imaging probes, *Biomaterials*, 2013, **34**(9), 2296–2306, DOI: 10.1016/j.biomaterials.2012.11.056.

176 H. Zhu, *et al.*, Fluorescent magnetic Fe3O4/rare earth colloidal nanoparticles for dual-modality imaging, *Small*, 2013, **9**(17), 2991–3000, DOI: 10.1002/smll.201300126.

177 J. Wang, S. Chen, H. Liu and W. Li, Magnetic and thermosensitive luminescent nanocomposites based on Fe3O4/SiO2/poly (N-isopropylacrylamide)/lanthanide-polyoxometalates and their controllable luminescence properties, *J. Rare Earths*, 2018, **36**(7), 733–738, DOI: 10.1016/j.jre.2018.01.006.

178 R. Piñol, *et al.*, Joining time-resolved thermometry and magnetic-induced heating in a single nanoparticle unveils intriguing thermal properties, *ACS Nano*, 2015, **9**(3), 3134–3142, DOI: 10.1021/acsnano.5b00059.

179 Y. Liu, Q. Ma, X. Dong, W. Yu, J. Wang and G. Liu, A novel strategy to directly fabricate flexible hollow nanofibers with tunable luminescence-electricity-magnetism trifunctionality using one-pot electrospinning, *Phys. Chem. Chem. Phys.*, 2015, **17**(35), 22977–22984, DOI: 10.1039/c5cp03522h.

180 X. Liang, X. Wang, J. Zhuang, Y. Chen, D. Wang and Y. Li, Synthesis of nearly monodisperse iron oxide and oxyhydroxide nanocrystals, *Adv. Funct. Mater.*, 2006, **16**(14), 1805–1813, DOI: 10.1002/adfm.200500884.

181 J. Yin, *et al.*, Dysprosium-doped iron oxide nanoparticles boosting spin–spin relaxation: A computational and experimental study, *Phys. Chem. Chem. Phys.*, 2019, **21**(22), 11883–11891.

182 L. Cheng, *et al.*, Multifunctional nanoparticles for upconversion luminescence/MR multimodal imaging and magnetically targeted photothermal therapy, *Biomaterials*, 2012, **33**(7), 2215–2222.

183 M. Zeng, *et al.*, Study on the mechanism of tunable ferromagnetic composites with different rare earth ions, *RSC Adv.*, 2021, **11**(59), 37246–37253, DOI: 10.1039/D1RA07249H.

184 S. Sutariya, *et al.*, Magnetic Control of the Manganese Photoluminescence in Fe_3 O_4/l -Cys ZnS:Mn Nanocomposites, *ACS Omega*, 2021, **6**(11), 7598–7604, DOI: 10.1021/acsomega.0c06164.

185 I. Apostolova, A. Apostolov and J. Wesselinowa, Magnetic Properties of Gd-Doped Fe3O4 Nanoparticles, *Appl. Sci.*, 2023, **13**(11), 6411, DOI: 10.3390/app13116411.

186 D. Liu, L. Tong, J. Shi and H. Yang, Luminescent and magnetic properties of YVO4:Ln3+@Fe3O4 (Ln3+=Eu3+ or Dy3+) nanocomposites, *J. Alloys Compd.*, 2012, **512**(1), 361–365, DOI: 10.1016/j.jallcom.2011.09.100.

187 M. Runowski, T. Grzyb and S. Lis, Magnetic and luminescent hybrid nanomaterial based on Fe3O4 nanocrystals and GdPO4:Eu3+ nanoneedles, *J. Nanopart. Res.*, 2012, **14**(10), 1188, DOI: 10.1007/s11051-012-1188-7.

188 M. Skwierczyńska, *et al.*, Luminescent–Magnetic Cellulose Fibers, Modified with Lanthanide-Doped Core/Shell Nanostructures, *ACS Omega*, 2018, **3**(8), 10383–10390, DOI: 10.1021/acsomega.8b00965.

189 L. Wang and Y. Li, Green upconversion nanocrystals for DNA detection, *Chem. Commun.*, 2006, **24**, 2557–2559, DOI: 10.1039/b604871d.

190 L. Cheng, *et al.*, Multifunctional upconversion nanoparticles for dual-modal imaging-guided stem cell therapy under remote magnetic control, *Adv. Funct. Mater.*, 2013, **23**(3), 272–280, DOI: 10.1002/adfm.201201733.

191 X. Zhu, J. Zhou, M. Chen, M. Shi, W. Feng and F. Li, Core–shell Fe3O4@NaLuF4:Yb,Er/Tm nanostructure for MRI, CT and upconversion luminescence tri-modality imaging, *Biomaterials*, 2012, **33**(18), 4618–4627, DOI: 10.1016/j.biomaterials.2012.03.007.

192 X. Zhu, J. Zhou, M. Chen, M. Shi, W. Feng and F. Li, Core–shell Fe3O4@ NaLuF4: Yb, Er/Tm nanostructure for MRI, CT and upconversion luminescence tri-modality imaging, *Biomaterials*, 2012, **33**(18), 4618–4627.

193 A. Xia, *et al.*, Core–shell NaYF4: Yb3+, Tm3+@ FexOy nanocrystals for dual-modality T2-enhanced magnetic resonance and NIR-to-NIR upconversion luminescent imaging of small-animal lymphatic node, *Biomaterials*, 2011, **32**(29), 7200–7208.

194 H. Xu, L. Cheng, C. Wang, X. Ma, Y. Li and Z. Liu, Polymer encapsulated upconversion nanoparticle/iron oxide nanocomposites for multimodal imaging and magnetic targeted drug delivery, *Biomaterials*, 2011, **32**(35), 9364–9373.

195 Y. Zhou, *et al.*, Investigation on the uptake and release ability of $β$-cyclodextrin functionalized Fe3O4 magnetic nanoparticles by methylene blue, *Mater. Chem. Phys.*, 2016, **170**, 83–89.

196 L. Cheng, *et al.*, Facile preparation of multifunctional upconversion nanoprobes for multimodal imaging and dual-targeted photothermal therapy, *Angew. Chem.*, 2011, **123**(32), 7523–7528.

197 P. Drake, *et al.*, Gd-doped iron-oxide nanoparticles for tumour therapy via magnetic field hyperthermia, *J. Mater. Chem.*, 2007, **17**(46), 4914, DOI: 10.1039/b711962c.

198 P. Kowalik, *et al.*, Yttrium-Doped Iron Oxide Nanoparticles for Magnetic Hyperthermia Applications, *J. Phys. Chem. C*, 2020, **124**(12), 6871–6883, DOI: 10.1021/acs.jpcc.9b11043.

199 H. T. Khuyen, *et al.*, Synthesis of Multifunctional Eu(III) Complex Doped Fe3O4/Au Nanocomposite for Dual Photo-Magnetic Hyperthermia and Fluorescence Bioimaging, *Molecules*, 2023, **28**(2), 749, DOI: 10.3390/molecules28020749.

200 D. D. Yengkhom, G. S. Ningombam, R. Heisnam, N. Sharma, R. S. Nongmaithem and F. A. S. Chipem, Carboxymethylcellulose modified Fe_3 O_4 @SiO_2 @$GdPO_4$:Tb^{3+} ,Ce^{3+} nanocomposites for combined optical and magnetic fluid hyperthermia in cancer therapy, *RSC Appl. Interfaces*, 2024, **1**(2), 313–322, DOI: 10.1039/D3LF00217A.

201 M. Pooresmaeil, H. Namazi and R. Salehi, Synthesis of photoluminescent glycodendrimer with terminal $β$-cyclodextrin molecules as a biocompatible pH-sensitive carrier for doxorubicin delivery, *Carbohydr. Polym.*, 2020, **246**, 116658.

202 D. Ahmadi, *et al.*, Preparation and in-vitro evaluation of pH-responsive cationic cyclodextrin coated magnetic nanoparticles for delivery of methotrexate to the Saos-2 bone cancer cells, *J. Drug Delivery Sci. Technol.*, 2020, **57**, 101584.

203 Y. Zhou, C. Wang, F. Wang, C. Li, C. Dong and S. Shuang, $β$-Cyclodextrin and Its Derivatives Functionalized Magnetic Nanoparticles for Targeting Delivery of Curcumin and Cell Imaging, *Chin. J. Chem.*, 2016, **34**(6), 599–608.

204 Y. Guo, S. Guo, J. Ren, Y. Zhai, S. Dong and E. Wang, Cyclodextrin functionalized graphene nanosheets with high supramolecular recognition capability: synthesis and host- guest inclusion for enhanced electrochemical performance, *ACS Nano*, 2010, **4**(7), 4001–4010.

205 D. Dosev, *et al.*, Magnetic/luminescent core/shell particles synthesized by spray pyrolysis and their application in immunoassays with internal standard, *Nanotechnology*, 2007, **18**(5), 55102.

206 Y. Zhang, G. K. Das, R. Xu and T. T. Y. Tan, Tb-doped iron oxide: bifunctional fluorescent and magnetic nanocrystals, *J. Mater. Chem.*, 2009, **19**(22), 3696–3703.

207 A. J. Siddon and C. A. Tormey, *The Chemical and Laboratory Investigation of Hemolysis*, Elsevier Inc., 1st edn, 2019, vol. 89, DOI: 10.1016/bs.acc.2018.12.006.

208 K. Saha, D. F. Moyano and V. M. Rotello, Protein coronas suppress the hemolytic activity of hydrophilic and hydrophobic nanoparticles, *Mater. Horiz.*, 2014, **1**(1), 102–105, DOI: 10.1039/c3mh00075c.

209 L. S. da Costa, *et al.*, Hybrid magneto-luminescent iron oxide nanocubes functionalized with europium complexes: synthesis, hemolytic properties and protein corona formation, *J. Mater. Chem. B*, 2021, **9**(2), 428–439.

210 L. Qian, F. Cui, Y. Yang, Y. Liu, S. Qi and C. Wang, Mechanisms of developmental toxicity in zebrafish embryos (Danio rerio) induced by boscalid, *Sci. Total Environ.*, 2018, **634**, 478–487.

211 S. Sieber, *et al.*, Zebrafish as a preclinical in vivo screening model for nanomedicines, *Adv. Drug Deliv. Rev.*, 2019, **151**, 152–168.

212 S. Lin, Y. Zhao, A. E. Nel and S. Lin, Zebrafish: an in vivo model for nano EHS studies, *Small*, 2013, **9**(9–10), 1608–1618.

213 G. H. Da Silva, *et al.*, Toxicity assessment of TiO2-MWCNT nanohybrid material with enhanced photocatalytic activity on Danio rerio (Zebrafish) embryos, *Ecotoxicol. Environ. Saf.*, 2018, **165**, 136–143.